ASSESSING THE BIOLOGICAL ACTIVITIES OF DNA-TEMPLATED SILVER NANOCLUSTERS AND FURTHERING THE CHARACTERIZATION OF NUCLEIC ACID NANOPARTICLES

by

Lewis Alexander Rolband

A dissertation submitted to the faculty of
The University of North Carolina at Charlotte
in partial fulfillment of the requirements
for the degree of Doctor of Philosophy in
Nanoscale Science

Charlotte

2023

Approved by:

_____
Dr. Kirill Afonin

_____
Dr. Jerry Troutman

_____
Dr. Jordan Poler

_____
Dr. Irina Nesmelova

ABSTRACT

LEWIS ALEXANDER ROLBAND. Assessing the Biological activities of DNA-templated silver nanoclusters and furthering the characterization of nucleic acid nanoparticles. (Under the direction of KIRILL AFONIN)

DNA and RNA are structurally and functionally diverse biopolymers that have shown promise in recent years as a powerful biomedical tool, in the form of nucleic acid nanotechnologies. The applications of these technologies include biosensing, diagnostics, cancer therapeutics, vaccines, and many more. A relatively unexplored area to which nucleic acid nanotechnology is being applied is the field of antibacterial research. By combining short DNA oligos with silver cations, folding the DNA into its proper secondary and tertiary structures, then reducing the silver, DNA may template the formation of few-atom silver nanoclusters (AgNCs). Silver has been well understood for centuries to be an effective antibacterial agent. Many silver nanostructures have been investigated for their potential efficacy as antibiotics. DNA-AgNCs have been shown to be effective at preventing bacterial growth in a variety of conditions. A unique advantage of DNA-AgNCs is that, unlike many larger silver nanostructures which typically absorb light through surface plasmon resonance, AgNCs fluoresce in a manner dependent on the sequence and structure of the templating oligonucleotide(s). Due to the unique structure-function relationship of AgNCs, further investigation of their structure is warranted. Presented herein is a thorough review of silver nanomaterials, along with work demonstrating the effectiveness of a DNA-AgNC hairpin system against a model E. coli system, and the characterization of an RNA ring which may serve as the scaffold for a multitude of functionalities, including DNA-AgNCs, in preparation for future work.

ACKNOWLEDGEMENTS

It is my greatest pleasure to give thanks to the countless people who have had a hand in shaping who I am today. In my 11 total years at the University of North Carolina at Charlotte, I have had the opportunity to learn from and have been inspired by so many outstanding faculty, staff, and peers that it would be impossible to name them all. To the entire University community, I am forever grateful.

Firstly, I would like to express my deepest thanks to my advisor, Dr. Kirill Afonin, for his constant support throughout my doctoral studies. His mentorship and guidance pushed me to always strive for excellence in my work and in myself. He never stopped encouraging me to push boundaries in my work and chase after any interesting research questions that we happened across. The freedom he granted me to pursue my research goals made my work all the more fulfilling. Through everything, Dr. Afonin's support has been a constant source of inspiration.

I am also exceptionally grateful for the mentorship of Dr. Joanna Krueger. Dr. Krueger has supported me since I took General Chemistry II with her all the way back in 2016. Her unwavering support allowed me the opportunity to grow significantly as a biochemist and as a person. Without Dr. Krueger's encouragement, I may not have considered pursuing a career in science in the first place.

To my committee members, Dr. Jerry Troutman, Dr. Jordan Poler, and Dr. Irina Nesmelova, I am endlessly thankful for the guidance offered to me over the years that helped shape my career. I am also grateful to Dr. Martin Panigaj for all of his training and wisdom, Dr. Caryn Striplin for being a constant source of motivation while also helping to keep me grounded, Dr. Brittany Johnson for always being willing to help and to teach me, Dr. Angelica Martins for allowing me the opportunity to work with her team and serving as an outstanding example of

what leadership should be, Dr. Juan Vivero-Escoto for always encouraging me to find ways to improve, Dr. Markus Etzkorn for giving me my first opportunity in scientific research and encouraging me at every stage of my career, Dr. Bernadette Donovan-Merkert for always ensuring my needs were met as a student, and to every other member of the Chemistry Department as a whole. Every member of this department has, at some point or another, been there to support me in my work and in my life.

My sincerest gratitude also must be given to my family. My parents, Gary and Debbie Rolband, have done nothing but offer unconditional love and support from my earliest days. All of my accomplishments ultimately rely on their never-ending encouragement. I am especially grateful to my brother, Jason, sister-in-law, Erin, and my sister, Rachel. They consistently reminded me what I was working so hard for and were always there for me to lean on in times of need.

To my many colleagues and labmates, Damian, Elizabeth, Yelixza, Leyla, Yasmine, Laura, Sabina, and all of the undergraduates I have had the pleasure of working with over the years, I am so thankful for the day-to-day motivation and guidance you have provided. To Dr. Justin Halman and Dr. Morgan Chandler, your help in the early days of my doctoral studies accelerated the beginning of my lab work while your unwavering friendship has served to help keep me motivated at every point in my career. I am also thankful for all of the help I received from Rebecca Hawes, Lisa Carlin, Brenda Fandrey, Cindy Honegger, Dr. Adam Fessler, and Dr. Jon Merkert. I would also like to thank James Byrnes, Kriti Chropra, Lin Yang, Shirish Chondankar, and entire team of the Life Sciences X-ray Scattering Beamline at the National Synchrotron Light Source-II and the Center for Biomolecular Structure at Brookhaven National Lab.

Finally, I would also like to thank the Graduate School Summer Fellowship and the Mining for Gold program for supporting my work.

DEDICATION

I would like to dedicate this work to my beautiful daughter, Lorelai Elizabeth Rolband, who's smile lights up my life and who's laughter brings endless warmth to my days.

TABLE OF CONTENTS

LIST OF FIGURES

LIST OF TABLES

LIST OF ABBREVIATIONS

TNA	Therapeutic nucleic acid
°C	Degrees Celsius
µg	Microgram
µL	Microliter
µM	Micromolar
µM	Micromolar
1D	One-dimensional
2D	Two-dimensional
3D	Three-dimensional
A	Adenine
Å	Angstrom
AFM	Atomic force microscopy
AgNC	Silver nanocluster
AgNP	Silver nanoparticle
AuNP	Gold nanoparticle
bp	Base pairs
C	Cytosine
CD	Circular dichroism
cryo-EM	Cryogenic electron microscopy
DLS	Dynamic Light Scattering
DMEM	Dulbecco's Modified Eagle's Medium
DNA	Deoxyribonucleic acid
DS	Dicer-substrate
E. coli	*Escherichia coli*
EDS	Energy-dispersive x-ray spectroscopy
EEM	Excitation-emission matrix
G	Guanine
HEPES	N-2-hydroxyethylpiperazine-N'-2-ethanesulfonic acid
KOH	Potassium hydroxide
LB	Luria broth
LNP	Lipid nanoparticle
mg	Milligram
mL	Milliliter
mM	Millimolar
mRNA	Messenger ribonucleic acid
MTS	3-(4,5-dimethylthiazol-2-yl)-5-(3-carboxymethoxyphenyl) -2-(4-sulfophenyl)-2H-tetrazolium
Mw	Molecular weight
N	Avogadro's number
NANPs	Nucleic acid nanoparticles
nm	Nanometer
nt	Nucleotides

OD	Optical density
PAGE	Polyacrylamide gel electrophoresis
pmol	Picomoles
pro-uPA	Pro-urokinase-type plasminogen activator
Rg	Radius of gyration
Rh	Hydrodynamic radius
RNA	Ribonucleic acid
ROS	Reactive oxygen species
rpm	Revolutions per minute
RPMI	Roswell Park Memorial Institute
SARS-CoV-2	Severe acute respiratory syndrome coronavirus 2
SAXS	Small-angle x-ray scattering
SD	Standard deviation
SEM	Standard error of the mean
ss	Single-stranded
T	Thymine
t1/2	Time to half maximum growth
U	Uracil
uPA	Urokinase-type plasminogen activator
v	Partial specific volume
VLP	Virus-like particle
ρ	Electron density

CHAPTER 1: INTRODUCTION: SMALL-ANGLE X-RAY SCATTERING'S ROLE IN THE DEVELOPMENT OF THERAPEUTIC NUCLEIC ACID FORMULATIONS

1. Introduction:

The use of RNA and DNA as biomedical tools is continuing to expand as many formulations have been introduced into the clinical space in the last 2 decades. As of 2021, at least 15 therapeutic nucleic acids, TNAs, have been approved by the Food and Drug Administration in the United States[1, 2]. Given the exceptional success of the two mRNA-based vaccines which led the fight against SARS-CoV-2, it is unlikely that the use of TNAs will be slowing soon[1, 2]. Furthermore, it is becoming clear that TNAs are able to address a number of diseases for which there are currently no or minimally effective treatments, such as novel viruses, many cancers, bacterial infections, and so forth[3]. All TNAs are subject to several challenges which must be overcome for them to become clinically useful. Primarily, these are the issues of effective delivery to the target tissues, blood stability, and off-target stimulation of the immune system[1-4]. The two main strategies which are conventionally applied to address these issues are the introduction of chemical modifications on the individual nucleotides and the use of non-nucleic acid materials as delivery agents[1-5]. To ensure the safety of these novel drugs, they must have high batch-to-batch consistency in the structure of both the oligonucleotide cargo and the delivery agent, as both will impact the biological activities of these novel formulations[6, 7]. Current characterization methods do not capture the structure of the active biologic compound while also measuring the entire population of nanoparticles within the formulation, necessitating the adaptation of new techniques to characterize them[8].

Small-angle x-ray scattering (SAXS) is a powerful technique for the characterization of a variety of nanomaterials. SAXS is particularly well suited to investigate the structure of biological macromolecules and their complexes in solution[9]. While much of the history of SAXS is concerned with the elucidation of protein structures, DNA, RNA ,and lipid vesicle structures can be probed

using the same methodologies, as the principals remain the same[7, 10-14]. While modeling the 3D structure of a biomolecule may not always be possible, as this requires a highly monodisperse and non-interacting sample population, the results of a SAXS experiment may still provide significant insight helping to reveal important details of the structure-function relationship in novel formulations[6, 7, 9]. Given the ability to assess the structural parameters of an entire sample in one measurement, rather than a discreet number of particles as is the case in microscopy based experiments, SAXS is also poised to serve as a means of screening drug batches to ensure production consistency at a level of detail which is not resolvable by conventional laser-light scattering based methods[7, 14, 15].

2. SAXS Background

SAXS is similar in practice to other diffraction based techniques, however, rather than having crystals which consist of multiple layers of ordered molecules capable of diffracting x-ray photons, the observed intensity is a result photons being scattered by pairs of atoms within a single particle.[10, 11, 16-19] As such, the intensity is purely the result of first-order Bragg diffraction. In practice, x-rays are scattered off the particles elastically, with the intensity of scattered photons being recorded as a function of the scattering vector, q, defined as follows:

Eq. 1 $$q = \frac{4\pi \sin(\theta)}{\lambda}$$

The wavelength of the x-rays is represented as λ, while θ represents half of the angle from the scattered light to the incident beam. Due to the experimental conditions of assessing macromolecular scattering in solution, wherein they are free to move and rotate as they randomly diffuse, the recorded signal represents the spherically averaged single particle scattering[9, 10]. These scattering intensities for a given particle in a single conformation is given by equation 2[8, 11, 20, 21].

Eq. 2 $$I(q) = I(0)e^{\frac{-q^2R_g^2}{3}}$$

With equation 2, two important structural parameters are able to be estimated from the SAXS data by way of a linear fit as determined by André Guinier[8, 9, 22]. The first of these is the radius of gyration, R_g, which represents the root-mean-square distance from the center of mass of the particle to each scattering element of the particle. The second is the forward scattering at zero angle, given as I(0), which is not directly measurable and must instead be inferred from the linear fit. This quantity is particularly important, however, as it allows for the molecular weight, M_w, to be estimated from the scattering profile, provided the particles are at a known concentration, C, as given by equation 3.

Eq. 3 $$I(0) = \frac{C\,\Delta\rho^2 v^2 M_w}{N}$$

In equation 3, the partial specific volume is denoted as v, Avogadro's number as N, and the contrast between the electron density of the bulk solvent and the particle is given by Δρ. The contrast term is a critical component of any SAXS experiments. In practice, the scattering of the particle is isolated from the scattering of the sample cell, bulk solvent/buffer, and atmosphere if the space between the sample and the detector is not isolated in a vacuum, by measuring the scattering of a 'buffer-only' sample which is matched to the buffer the analyte is in via dialysis or any number of similar processes. The scattering profile of the matched buffer is then subtracted from the scattering profile of the solution containing the analyte of interest so that, ideally, only the scattering of the particle under investigation remains. As such, any mismatches between the buffer the particle resides in and the buffer-only sample result in significant reductions in data quality[8, 16, 17, 19].

3. Previous Studies

3.1 Nucleic acid structures. Much of the earliest work using SAXS to characterize oligonucleotides was focused on naturally occurring oligos with known functions or on nucleic acid binding proteins[23]. These included examinations of several ribozymes, such as the *Tetrahymena* ribozyme, which is one of the first examples of a low-resolution dummy-atom model being built of a functional RNA structure from its SAXS profile[24]. Once it was made clear that the structure determination algorithms which had initially been made with proteins in mind were able to be applied to nucleic acid structures as well, other increasingly complicated structures could begin to be investigated[23-28]. Additionally, many new tools began development to provide modeling software specifically designed to model DNA and RNA based structures[16, 19, 27, 29]. The two main classes of ordered TNAs with specific structures that have directly benefited from SAXS studies directly on the employed oligos themselves are aptamers and nucleic acid nanoparticles, NANPs[3, 6, 30-35].

Aptamers represent a unique class of TNA which are functionally similar to antibodies, in that they bind target molecules with specificity and high affinity[1, 2, 36-38]. SAXS has been critical in determining the functional structures of several therapeutic aptamers, such as the LC-18 aptamer which targets lung adenocarcinoma[39] and multiple aptamers against pro-urokinase-type plasminogen activator, pro-uPA, an important drug target for owing to its many roles in tissue remodeling and blood clot clearance among others[38, 40]. Preventing the activation of uPA in cancer patients is particularly important as a means of preventing metastasis[40]. Beyond the structural characterization, SAXS was also key in uncovering the mechanism by which upanap-12.49 most likely inhibits the activation of pro-uPA[38]. Through a series of mutagenesis studies, it was found that upanap-12.49 binds to a separate domain than the one where the plasmin cleavage site, which converts the enzyme from its zymogen form to the active form, is located. Following SAXS studies of the aptamer, it was determined that it has an elongated, rod-like, shape. When rigid body modeling was employed to fit the pro-uPA–upanap12.49 complex against the SAXS profiles

of the same, all solutions found the elongated aptamer in close proximity to the activation bond at K158-I159. The implication of these results was that, despite the binding site being some distance away, the size of the aptamer allows it to sterically hinder access to this bond, preventing its cleavage.

NANPs are very functionally diverse owing to their ability to self-assemble into specific geometries while being able to be adapted with any number of different moieties such as aptamers, gene therapies, fluorophores, and silver nanoclusters to name a few[33, 34, 41-45]. Two of the main parameters which dictate the interaction of NANPs with the innate immune system lies in their dimensionality (globular vs planar vs fibrous), and in the arrangement of TNAs around the NANPs which serves as a scaffold to specifically place these moieties in 3D space[6, 46]. To date, only one NANP platform carrying TNAs has been characterized via SAXS, a hexameric RNA ring capable of carrying up to six separate functionalities. Using SAXS, it was confirmed that the dicer-substrate RNAs, DS RNAs, carried by the ring tended to fold into a more compact structure than was initially suggested by atomic force microscopy through the pair-wise distance distribution functions and the estimated maximum linear dimensions. Furthermore, the three-dimensional structure was determined through a dummy-atom modeling approach for the ring without added functionalization and with six DS RNAs. From this modeling, the positioning of the DS RNAs out of the plane of the ring was observed, similarly to what had been previously reported from cryogenic electron microscopy, cryo-EM, though some models showed the arms positioned planarly. This ambiguity in the modeling was anticipated, however, as the SAXS profiles are the result of the population-weighted conformational average across all the particles and the DS RNAs are attached with a highly flexible linker formed by two unpaired uracil residues. Given the potential utility of SAXS as a characterization tool for NANPs, and as more NANPs are developed with significant therapeutic potential, it is anticipated that the use of SAXS for this purpose will expand with time[8].

3.2 Nucleic acids in complex with delivery agents. In the case of antisense oligos, mRNAs, and siRNAs, the structure of the nucleic acid component is not generally considered to be of as significant importance as the structure of the complex it forms with a variety of carrier molecules[1, 2]. Two key technologies for the packaging of TNAs for clinical use which can greatly benefit from SAXS characterization include virus-like particles, VLPs, and lipid nanoparticles, LNPs[18, 34, 47]. It should be noted that many other potential carrier molecules exist for the delivery TNAs to target tissues; however, these are the two most clinically relevant and are both made from biomolecules. Other potential carriers include mesoporous silica nanoparticles, exosomes, dendrimers, and bolaamphiphiles to name a few[1, 2, 47-53].

Recombinantly formed VLPs are generally made from non-encapsulated viruses, such as adeno-associated viruses[1, 47, 54]. The non-encapsulation refers to the lack of lipid components around the protein capsid which houses the TNA cargo[54, 55]. A common model organism for the SAXS based assessment of VLPs is the MS2 bacteriophage which is known to infect *E. coli*[55]. Recently, the ability to assess the structure of RNA packaged within VLP protein capsids has been expanded through the use of contrast variation SAXS, in which SAXS measurements are taken on a sucrose gradient[56]. The sucrose is used to gradually increase the electron density of the bulk solvent until it matches that of the protein capsid surrounding the single-stranded RNA cargo. As a result, the scattering profile of the packaged RNA can be separated from the scattering of the capsid, and they can be modeled independently of one another. Through this method, it was found that the viral capsid is permeable by the solvent, allowing sucrose to diffuse into the capsid. It was confirmed through these experiments that the packaged RNA is significantly compacted and less flexible in comparison to the un-encapsidated RNA. Upon comparison with previous cryo-EM results, it was found that the two techniques were able to capture similar levels of structural detail. One key finding was that the SAXS-based dummy-atom modeling was able to resolve a small piece of RNA which protrudes out from the capsid. The use of contrast variation

SAXS was also found to be significantly easier than the asymmetric cryo-EM experiments required to resolve the two components, protein and RNA, of the MS2 bacteriophage. Moving forward, this methodology will likely prove to be a key step in the process of confirming the proper packaging of TNAs within VLPs.

The recent success of two mRNA based vaccines against the COVID19 virus have highlighted the usefulness of LNPs as delivery agents for TNAs. SAXS has been previously used to extensively characterize a variety of LNPs intended for biomedical applications and allows for the observation of lipid lamellae formation among several other key features of LNPs[14]. A hybrid lipid-protamine nanoparticle, referred to here as the LNP for brevity, for the delivery of mRNA was recently characterized via SAXS, in conjunction with small-angle neutron scattering, SANS, and cryo-EM, to clarify the structure–function relationship of the LNP while also observing how different protocols for mixing the three components of the formulation impacted the structure and, in turn, the efficacy. In total, nine protocols for producing the final drug product were tested. It was found that the protocols which were determined to have more lamellar structures and were less compact overall tended to have significantly increased transfection efficiency as indicated by the increased production of the protein coded for by the mRNA cargo. While cryo-EM was able to provide images that displayed these lamellae, the SAXS and SANS measurements were able to quantitatively describe the thickness of these lamellae across the entire sample population. These results were consistent with other examples of RNA or DNA intercalated within the hydrophilic regions between lipid bilayers[57-60].

4. Future Directions and Theme

The role of TNAs is rapidly expanding and as such, our understanding of their unique structure–function relationship must continue to expand. As NANPs continue to show increased potential due to their modular and multivalent nature, their utilization is likely to continue to expand. SAXS's role in the future development of TNAs and of NANPs in particular is two-fold.

Firstly, the use of SAXS in the research and development space will be critical to assess and optimize the structure of both the TNAs and their formulations. A second, and often less discussed role, is in the confirmation batch-to-batch consistency of these formulations, as SAXS probes the entire sample population at once and data collection is rapid, on the order of a few seconds with as little as 60 µL of samples in many cases[61, 62]. This structural consistency is particularly important for biologic drugs, as they are typically administered at much higher concentrations than is typically encountered in a laboratory setting, where interparticle interactions can be significant[63].

A relatively unexplored field of TNA research is in the realm of antibacterial therapies. As such, the work presented herein focuses on the investigation of the antibacterial potential DNA-templated silver nanoclusters (DNA-AgNCs). This technology has great potential due to its unique fluorescent properties, making it easy to visualize, while also being nontoxic to mammalian cells at concentrations double what has been found to effectively reduce the growth of bacteria[64]. Furthermore, owing to its DNA template, DNA-AgNCs can be readily incorporated onto existing NANP scaffolds[45]. Through this multivalency effect, it is possible that the efficacy of the DNA-AgNCs can be greatly increased by increasing the local concentration of DNA-AgNCs[65]. Additionally, work towards improving the ability of NANPs to be modeled from SAXS data is presented using a hexameric RNA ring carrying six DS RNAs. We have used this NANP scaffold previously to tune the properties of DNA-AgNCs[45]. Moving forward, the combination of an antibacterial DNA-AgNC on this NANP scaffold may lead to a powerful new means of fighting bacterial infections; however, it must be confirmed that the proper structures are being formed to ensure that any observed effects are the results of the inclusion of multiple DNA-AgNCs on a single, discreet, nanoparticle platform rather than from an agglomeration of silver. As such, the presented work serves as a jumping off point for the further development of this potential TNA formulation.

References

1. Kulkarni, J. A.; Witzigmann, D.; Thomson, S. B.; Chen, S.; Leavitt, B. R.; Cullis, P. R.; Van Der Meel, R., The current landscape of nucleic acid therapeutics. *Nature Nanotechnology* **2021,** *16* (6), 630-643.
2. Yamada, Y., Nucleic Acid Drugs—Current Status, Issues, and Expectations for Exosomes. *Cancers* **2021,** *13* (19), 5002.
3. Afonin, K. A.; Dobrovolskaia, M. A.; Ke, W.; Grodzinski, P.; Bathe, M., Critical review of nucleic acid nanotechnology to identify gaps and inform a strategy for accelerated clinical translation. *Advanced Drug Delivery Reviews* **2022,** *181*, 114081.
4. Panigaj, M.; Dobrovolskaia, M. A.; Afonin, K. A., 2021: an immunotherapy odyssey and the rise of nucleic acid nanotechnology. *Nanomedicine* **2021,** *16* (19), 1635-1640.
5. Saito, R. F.; Rangel, M. C.; Halman, J. R.; Chandler, M.; de Sousa Andrade, L. N.; Odete-Bustos, S.; Furuya, T. K.; Carrasco, A. G. M.; Chaves-Filho, A. B.; Yoshinaga, M. Y.; Miyamoto, S.; Afonin, K. A.; Chammas, R., Simultaneous silencing of lysophosphatidylcholine acyltransferases 1-4 by nucleic acid nanoparticles (NANPs) improves radiation response of melanoma cells. *Nanomedicine: Nanotechnology, Biology and Medicine* **2021,** *36*, 102418.
6. Chandler, M.; Rolband, L.; Johnson, M. B.; Shi, D.; Avila, Y. I.; Cedrone, E.; Beasock, D.; Danai, L.; Stassenko, E.; Krueger, J. K.; Jiang, J.; Lee, J. S.; Dobrovolskaia, M. A.; Afonin, K. A., Expanding Structural Space for Immunomodulatory Nucleic Acid Nanoparticles (Nanps) via Spatial Arrangement of Their Therapeutic Moieties. *Advanced Functional Materials* **2022**, 2205581.
7. Siewert, C. D.; Haas, H.; Cornet, V.; Nogueira, S. S.; Nawroth, T.; Uebbing, L.; Ziller, A.; Al-Gousous, J.; Radulescu, A.; Schroer, M. A.; Blanchet, C. E.; Svergun, D. I.; Radsak, M. P.; Sahin, U.; Langguth, P., Hybrid Biopolymer and Lipid Nanoparticles with Improved Transfection Efficacy for mRNA. *Cells* **2020,** *9* (9), 2034.
8. Oliver, R. C.; Rolband, L. A.; Hutchinson-Lundy, A. M.; Afonin, K. A.; Krueger, J. K., Small-Angle Scattering as a Structural Probe for Nucleic Acid Nanoparticles (NANPs) in a Dynamic Solution Environment. *Nanomaterials* **2019,** *9* (5), 681.
9. Jacques, D. A.; Trewhella, J., Small-angle scattering for structural biology—Expanding the frontier while avoiding the pitfalls. *Protein science* **2010,** *19* (4), 642-657.
10. Trewhella, J.; Duff, A. P.; Durand, D.; Gabel, F.; Guss, J. M.; Hendrickson, W. A.; Hura, G. L.; Jacques, D. A.; Kirby, N. M.; Kwan, A. H.; Pérez, J.; Pollack, L.; Ryan, T. M.; Sali, A.; Schneidman-Duhovny, D.; Schwede, T.; Svergun, D. I.; Sugiyama, M.; Tainer, J. A.; Vachette, P.; Westbrook, J.; Whitten, A. E., 2017 publication guidelines for structural modelling of small-angle scattering data from biomolecules in solution: an update. *Acta Crystallographica Section D Structural Biology* **2017,** *73* (9), 710-728.
11. Grant, T. D.; Luft, J. R.; Carter, L. G.; Matsui, T.; Weiss, T. M.; Martel, A.; Snell, E. H., The accurate assessment of small-angle X-ray scattering data. *Acta Crystallogr. Sect. D-Biol. Crystallogr.* **2015,** *71*, 45-56.
12. Mahieu, E.; Gabel, F., Biological small-angle neutron scattering: recent results and development. *Acta Crystallographica Section D* **2018,** *74* (8), 715-726.
13. Rambo, R. P.; Tainer, J. A., Bridging the solution divide: comprehensive structural analyses of dynamic RNA, DNA, and protein assemblies by small-angle X-ray scattering. *Curr. Opin. Struct. Biol.* **2010,** *20* (1), 128-137.
14. Sartori, B.; Marmiroli, B., Tailoring Lipid-Based Drug Delivery Nanosystems by Synchrotron Small Angle X-ray Scattering. *Pharmaceutics* **2022,** *14* (12), 2704.
15. Minton, A. P., Recent applications of light scattering measurement in the biological and biopharmaceutical sciences. *Anal. Biochem.* **2016,** *501*, 4-22.

16. Rambo, R. P.; Tainer, J. A., Improving small-angle X-ray scattering data for structural analyses of the RNA world. *Rna* **2010,** *16* (3), 638-646.
17. Yang, S. C., Methods for SAXS-Based Structure Determination of Biomolecular Complexes. *Adv. Mater.* **2014,** *26* (46), 7902-7910.
18. Svergun, D. I., Restoring Low Resolution Structure of Biological Macromolecules from Solution Scattering Using Simulated Annealing. *Biophys. J.* **1999,** *76* (6), 2879-2886.
19. Yang, S.; Parisien, M.; Major, F.; Roux, B., RNA Structure Determination Using SAXS Data. *The Journal of Physical Chemistry B* **2010,** *114* (31), 10039-10048.
20. Svergun, D. I.; Petoukhov, M. V.; Koch, M. H. J., Determination of Domain Structure of Proteins from X-Ray Solution Scattering. *Biophys. J.* **2001,** *80* (6), 2946-2953.
21. Svergun, D. I.; Koch, M. H. J., Small-angle scattering studies of biological macromolecules in solution. *Rep. Prog. Phys.* **2003,** *66* (10), 1735-1782.
22. Guinier, A., La diffraction des rayons X aux très petits angles: application à l'étude de phénomènes ultramicroscopiques. *Ann. Phys. Onzieme Serie* **1939,** *12*, 161-237.
23. Lipfert, J.; Doniach, S., Small-Angle X-Ray Scattering from RNA, Proteins, and Protein Complexes. *Annu. Rev. Biophys. Biomolec. Struct.* **2007,** *36* (1), 307-327.
24. Lipfert, J.; Chu, V. B.; Bai, Y.; Herschlag, D.; Doniach, S., Low-resolution models for nucleic acids from small-angle X-ray scattering with applications to electrostatic modeling. *J. Appl. Crystallogr.* **2007,** *40* (s1), s229-s234.
25. Bruetzel, L. K.; Gerling, T.; Sedlak, S. M.; Walker, P. U.; Zheng, W.; Dietz, H.; Lipfert, J., Conformational Changes and Flexibility of DNA Devices Observed by Small-Angle X-ray Scattering. *Nano Lett.* **2016,** *16* (8), 4871-4879.
26. Bruetzel, L. K.; Walker, P. U.; Gerling, T.; Dietz, H.; Lipfert, J., Time-Resolved Small-Angle X-ray Scattering Reveals Millisecond Transitions of a DNA Origami Switch. *Nano Lett.* **2018,** *18* (4), 2672-2676.
27. Gajda, M. J.; Martinez Zapien, D.; Uchikawa, E.; Dock-Bregeon, A.-C., Modeling the Structure of RNA Molecules with Small-Angle X-Ray Scattering Data. *PLoS One* **2013,** *8* (11), e78007.
28. Chen, Y.; Pollack, L., SAXS studies of RNA : structures, dynamics, and interactions with partners. *WIREs RNA* **2016,** *7* (4), 512-526.
29. Reyes, F. E.; Schwartz, C. R.; Tainer, J. A.; Rambo, R. P., Methods for Using New Conceptual Tools and Parameters to Assess RNA Structure by Small-Angle X-Ray Scattering. In *Riboswitch Discovery, Structure and Function*, BurkeAguero, D. H., Ed. Elsevier Academic Press Inc: San Diego, 2014; Vol. 549, pp 235-263.
30. Afonin, K. A.; Bindewald, E.; Yaghoubian, A. J.; Voss, N.; Jacovetty, E.; Shapiro, B. A.; Jaeger, L., In vitro assembly of cubic RNA-based scaffolds designed in silico. *Nature Nanotechnology* **2010,** *5* (9), 676-682.
31. Afonin, K. A.; Dobrovolskaia, M. A.; Church, G.; Bathe, M., Opportunities, Barriers, and a Strategy for Overcoming Translational Challenges to Therapeutic Nucleic Acid Nanotechnology. *ACS Nano* **2020,** *14* (8), 9221-9227.
32. Afonin, K. A.; Grabow, W. W.; Walker, F. M.; Bindewald, E.; Dobrovolskaia, M. A.; Shapiro, B. A.; Jaeger, L., Design and self-assembly of siRNA-functionalized RNA nanoparticles for use in automated nanomedicine. *Nature Protocols* **2011,** *6* (12), 2022-2034.
33. Afonin, K. A.; Kasprzak, W. K.; Bindewald, E.; Kireeva, M.; Viard, M.; Kashlev, M.; Shapiro, B. A., In silico design and enzymatic synthesis of functional RNA nanoparticles. *Accounts Chem. Res.* **2014,** *47* (6), 1731-1741.
34. Afonin, K. A.; Viard, M.; Koyfman, A. Y.; Martins, A. N.; Kasprzak, W. K.; Panigaj, M.; Desai, R.; Santhanam, A.; Grabow, W. W.; Jaeger, L.; Heldman, E.; Reiser, J.; Chiu, W.; Freed, E. O.; Shapiro, B. A., Multifunctional RNA Nanoparticles. *Nano Lett.* **2014,** *14* (10), 5662-5671.

35. Chandler, M.; Panigaj, M.; Rolband, L. A.; Afonin, K. A., Challenges in optimizing RNA nanostructures for large-scale production and controlled therapeutic properties. *Nanomedicine* **2020,** *15* (13), 1331-1340.
36. Baird, N. J.; Ferré-D'Amaré, A. R., Idiosyncratically tuned switching behavior of riboswitch aptamer domains revealed by comparative small-angle X-ray scattering analysis. *Rna* **2010,** *16* (3), 598-609.
37. Reinstein, O.; Neves, M. A.; Saad, M.; Boodram, S. N.; Lombardo, S.; Beckham, S. A.; Brouwer, J.; Audette, G. F.; Groves, P.; Wilce, M. C., Engineering a structure switching mechanism into a steroid-binding aptamer and hydrodynamic analysis of the ligand binding mechanism. *Biochemistry* **2011,** *50* (43), 9368-9376.
38. Dupont, D. M.; Thuesen, C. K.; Bøtkjær, K. A.; Behrens, M. A.; Dam, K.; Sørensen, H. P.; Pedersen, J. S.; Ploug, M.; Jensen, J. K.; Andreasen, P. A., Protein-Binding RNA Aptamers Affect Molecular Interactions Distantly from Their Binding Sites. *PLoS One* **2015,** *10* (3), e0119207.
39. Morozov, D.; Mironov, V.; Moryachkov, R. V.; Shchugoreva, I. A.; Artyushenko, P. V.; Zamay, G. S.; Kolovskaya, O. S.; Zamay, T. N.; Krat, A. V.; Molodenskiy, D. S.; Zabluda, V. N.; Veprintsev, D. V.; Sokolov, A. E.; Zukov, R. A.; Berezovski, M. V.; Tomilin, F. N.; Fedorov, D. G.; Alexeev, Y.; Kichkailo, A. S., The role of SAXS and molecular simulations in 3D structure elucidation of a DNA aptamer against lung cancer. *Molecular Therapy - Nucleic Acids* **2021,** *25*, 316-327.
40. Mahmood, N.; Mihalcioiu, C.; Rabbani, S. A., Multifaceted Role of the Urokinase-Type Plasminogen Activator (uPA) and Its Receptor (uPAR): Diagnostic, Prognostic, and Therapeutic Applications. *Frontiers in Oncology* **2018,** *8*.
41. Panigaj, M.; Johnson, M. B.; Ke, W.; McMillan, J.; Goncharova, E. A.; Chandler, M.; Afonin, K. A., Aptamers as Modular Components of Therapeutic Nucleic Acid Nanotechnology. *ACS Nano* **2019,** *13* (11), 12301-12321.
42. Afonin, K. A.; Kireeva, M.; Grabow, W. W.; Kashlev, M.; Jaeger, L.; Shapiro, B. A., Co-transcriptional Assembly of Chemically Modified RNA Nanoparticles Functionalized with siRNAs. *Nano Lett.* **2012,** *12* (10), 5192-5195.
43. Chandler, M.; Minevich, B.; Roark, B.; Viard, M.; Johnson, M. B.; Rizvi, M. H.; Deaton, T. A.; Kozlov, S.; Panigaj, M.; Tracy, J. B.; Yingling, Y. G.; Gang, O.; Afonin, K. A., Controlled Organization of Inorganic Materials Using Biological Molecules for Activating Therapeutic Functionalities. *ACS Applied Materials & Interfaces* **2021,** *13* (33), 39030-39041.
44. Tannir, Z. E.; Afonin, K. A.; Shapiro, B., RNA and DNA nanoparticles for triggering RNA interference. *RNA & DISEASE* **2015,** *2*.
45. Yourston, L.; Rolband, L.; West, C.; Lushnikov, A.; Afonin, K. A.; Krasnoslobodtsev, A. V., Tuning properties of silver nanoclusters with RNA nanoring assemblies. *Nanoscale* **2020,** *12* (30), 16189-16200.
46. Hong, E.; Halman, J. R.; Shah, A. B.; Khisamutdinov, E. F.; Dobrovolskaia, M. A.; Afonin, K. A., Structure and Composition Define Immunorecognition of Nucleic Acid Nanoparticles. *Nano Lett.* **2018,** *18* (7), 4309-4321.
47. Markova, N.; Cairns, S.; Jankevics-Jones, H.; Kaszuba, M.; Caputo, F.; Parot, J., Biophysical Characterization of Viral and Lipid-Based Vectors for Vaccines and Therapeutics with Light Scattering and Calorimetric Techniques. *Vaccines* **2021,** *10* (1), 49.
48. Dobrovolskaia, M. A.; McNeil, S. E., Strategy for selecting nanotechnology carriers to overcome immunological and hematological toxicities challenging clinical translation of nucleic acid-based therapeutics. *Expert Opin Drug Deliv* **2015,** *12* (7), 1163-75.
49. Mollé, L. M.; Smyth, C. H.; Yuen, D.; Johnston, A. P. R., Nanoparticles for vaccine and gene therapy: Overcoming the barriers to nucleic acid delivery. *WIREs Nanomedicine and Nanobiotechnology* **2022,** *14* (6).

50. Juneja, R.; Vadarevu, H.; Halman, J.; Tarannum, M.; Rackley, L.; Dobbs, J.; Marquez, J.; Chandler, M.; Afonin, K.; Vivero-Escoto, J. L., Combination of Nucleic Acid and Mesoporous Silica Nanoparticles: Optimization and Therapeutic Performance In Vitro. *ACS Applied Materials & Interfaces* **2020,** *12* (35), 38873-38886.
51. Kim, T.; Viard, M.; Afonin, K. A.; Gupta, K.; Popov, M.; Salotti, J.; Johnson, P. F.; Linder, C.; Heldman, E.; Shapiro, B. A., Characterization of Cationic Bolaamphiphile Vesicles for siRNA Delivery into Tumors and Brain. *Molecular Therapy - Nucleic Acids* **2020,** *20*, 359-372.
52. Halman, J. R.; Kim, K.-T.; Gwak, S.-J.; Pace, R.; Johnson, M. B.; Chandler, M. R.; Rackley, L.; Viard, M.; Marriott, I.; Lee, J. S.; Afonin, K. A., A cationic amphiphilic co-polymer as a carrier of nucleic acid nanoparticles (Nanps) for controlled gene silencing, immunostimulation, and biodistribution. *Nanomedicine: Nanotechnology, Biology and Medicine* **2020,** *23*, 102094.
53. Avila, Y. I.; Chandler, M.; Cedrone, E.; Newton, H. S.; Richardson, M.; Xu, J.; Clogston, J. D.; Liptrott, N. J.; Afonin, K. A.; Dobrovolskaia, M. A. Induction of Cytokines by Nucleic Acid Nanoparticles (NANPs) Depends on the Type of Delivery Carrier *Molecules* [Online], 2021.
54. Naso, M. F.; Tomkowicz, B.; Perry, W. L.; Strohl, W. R., Adeno-Associated Virus (AAV) as a Vector for Gene Therapy. *BioDrugs* **2017,** *31* (4), 317-334.
55. Krueger, S.; Huie, J. L.; Kuzmanovic, D., Small angle scattering analysis of virus-like particles for biomedical diagnostic assays. *Neutron Scattering Methods and Studies* **2013**, 35-58.
56. San Emeterio, J.; Pollack, L., Visualizing a viral genome with contrast variation small angle X-ray scattering. *J. Biol. Chem.* **2020,** *295* (47), 15923-15932.
57. Badwaik, V. D.; Aicart, E.; Mondjinou, Y. A.; Johnson, M. A.; Bowman, V. D.; Thompson, D. H., Structure-property relationship for in vitro siRNA delivery performance of cationic 2-hydroxypropyl-β-cyclodextrin: PEG-PPG-PEG polyrotaxane vectors. *Biomaterials* **2016,** *84*, 86-98.
58. Ziller, A.; Nogueira, S. S.; Hühn, E.; Funari, S. S.; Brezesinski, G.; Hartmann, H.; Sahin, U.; Haas, H.; Langguth, P., Incorporation of mRNA in Lamellar Lipid Matrices for Parenteral Administration. *Molecular Pharmaceutics* **2018,** *15* (2), 642-651.
59. Weisman, S.; Hirsch-Lerner, D.; Barenholz, Y.; Talmon, Y., Nanostructure of Cationic Lipid-Oligonucleotide Complexes. *Biophys. J.* **2004,** *87* (1), 609-614.
60. Rädler, J. O.; Koltover, I.; Salditt, T.; Safinya, C. R., Structure of DNA-Cationic Liposome Complexes: DNA Intercalation in Multilamellar Membranes in Distinct Interhelical Packing Regimes. *Science* **1997,** *275* (5301), 810-814.
61. Yang, L.; Antonelli, S.; Chodankar, S.; Byrnes, J.; Lazo, E.; Qian, K., Solution scattering at the Life Science X-ray Scattering (LiX) beamline. *Journal of Synchrotron Radiation* **2020,** *27* (3), 804-812.
62. Yang, L.; Lazo, E.; Byrnes, J.; Chodankar, S.; Antonelli, S.; Rakitin, M., Tools for supporting solution scattering during the COVID-19 pandemic. *Journal of synchrotron radiation* **2021,** *28* (4).
63. Mosbæk, C. R.; Konarev, P. V.; Svergun, D. I.; Rischel, C.; Vestergaard, B., High Concentration Formulation Studies of an IgG2 Antibody Using Small Angle X-ray Scattering. *Pharmaceutical Research* **2012,** *29* (8), 2225-2235.
64. Rolband, L.; Yourston, L.; Chandler, M.; Beasock, D.; Danai, L.; Kozlov, S.; Marshall, N.; Shevchenko, O.; Krasnoslobodtsev, A. V.; Afonin, K. A., DNA-Templated Fluorescent Silver Nanoclusters Inhibit Bacterial Growth While Being Non-Toxic to Mammalian Cells. *Molecules* **2021,** *26* (13), 4045.

65. Javani, S.; Lorca, R.; Latorre, A.; Flors, C.; Cortajarena, A. L.; Somoza, Á., Antibacterial Activity of DNA-Stabilized Silver Nanoclusters Tuned by Oligonucleotide Sequence. *ACS Applied Materials & Interfaces* **2016,** *8* (16), 10147-10154.

CHAPTER 2: OPTICAL PROPERTIES AND ANTIBACTERIAL ACTIVITIES OF SILVER NANOPARTICLES AND DNA-TEMPLATED SILVER NANOCLUSTERS

Introduction

Nanoscale silver structures are investigated for their distinct physiochemical and biological characteristics, as compared to larger-scale bulk silver. Atomic silver structures, only several nanometers in size, have a mixture of unique fluorescent, catalytic, and antibacterial properties [1-14]. Applying nanotechnology to silver allows for the precise assembly of silver nanostructures in a predictable and controllable fashion. The properties of nanoparticles depend heavily on size and shape, which can be designed to achieve specific and unique functions and qualities. Depending on the intended function of the nanostructure, certain physical properties of the atomic silver structures can be fine-tuned during synthesis to produce desirable characteristics. Furthermore, chemical properties of silver nanostructures, e.g., composition, coating, and in-solution reactivity, can be readily functionalized to avoid toxicity or agglomeration while maximizing these system's effectiveness as biosensors antibacterial agents [6, 10, 11, 13-23].

The worldwide concern of bacterial drug resistance, accelerated by misuse and over-prescription of antibiotics [24], has become one of the main challenges facing our society. This issue is exacerbated by the declining interest of big pharmaceutical companies in developing new antibacterial treatments [25]. As antibiotics used in the clinic combat bacteria by affecting a specific mechanism or location of the cell, bacterial strains adapt and eventually become resistant to these (**Figure 1**). A solution would be the development of bacteria specific therapies that employ a single active compound yet can efficiently target multiple essential biochemical pathways, thus delaying the bacterial evolution for drug resistance. Silver is well poised to fill this unique biomedical niche [26].

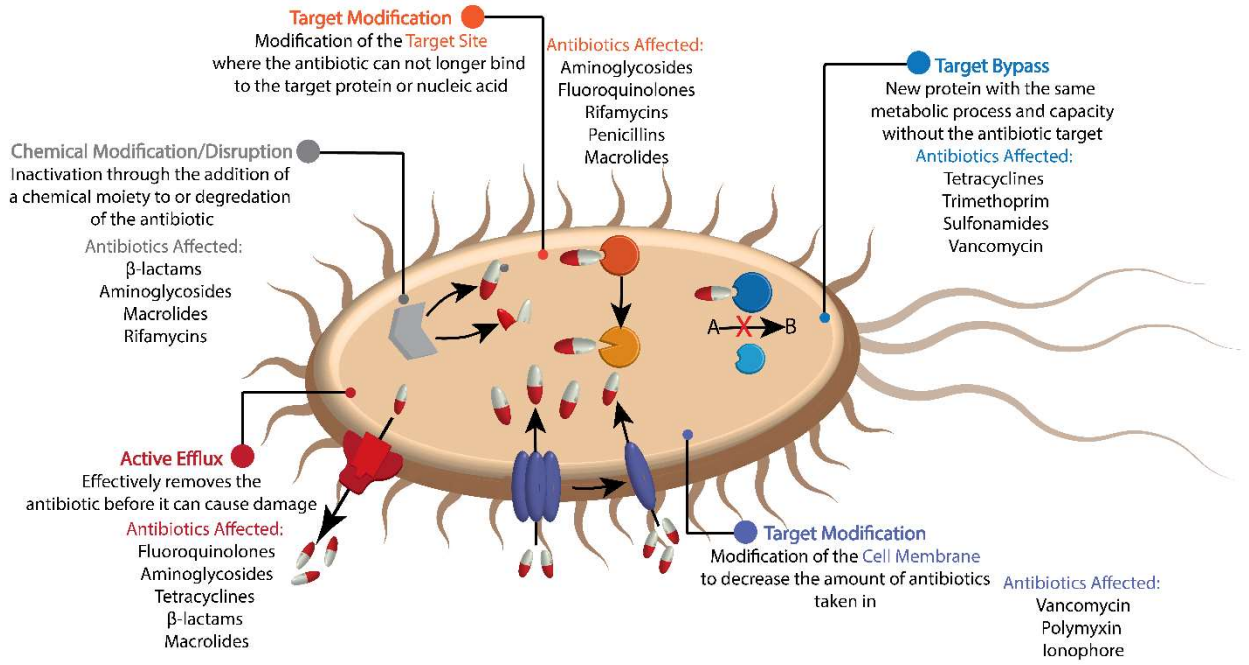

Figure 1: Schematic mechanisms of bacterial antibiotic resistance and list of some antibiotics affected.

Silver nanoparticles (AgNPs), averaging in size around 10 nm – 80 nm, while well-affiliated with bactericidal activity, are still increasingly investigated for unique physiochemical and biological characteristics which are distinct from the bulk analogs [27]. Silver's efficacy as an antibacterial material, particularly when solubilized in its monovalent cation state, has been known since ancient times and under investigation since[16, 28, 29]. Recently, AgNPs, consisting of a combination of cationic (Ag^{+}) and elemental silver (Ag^{0}), have been actively researched for ability to serve as antibacterial agents in a variety of biomedical applications, such as burn/wound dressings or topical creams [26, 29]. The antibacterial mechanism of AgNPs was poorly understood until 2004, despite having been investigated as early as 1953 [3, 28, 30]. Recent studies have shown that AgNPs are capable of inhibiting bacterial growth through a multitude of mechanisms. Due to the bacteriostatic and bactericidal properties of AgNPs that impact structural and biochemical

features of pathogens, it becomes difficult for bacteria to evolve defense mechanisms against them [31-33].

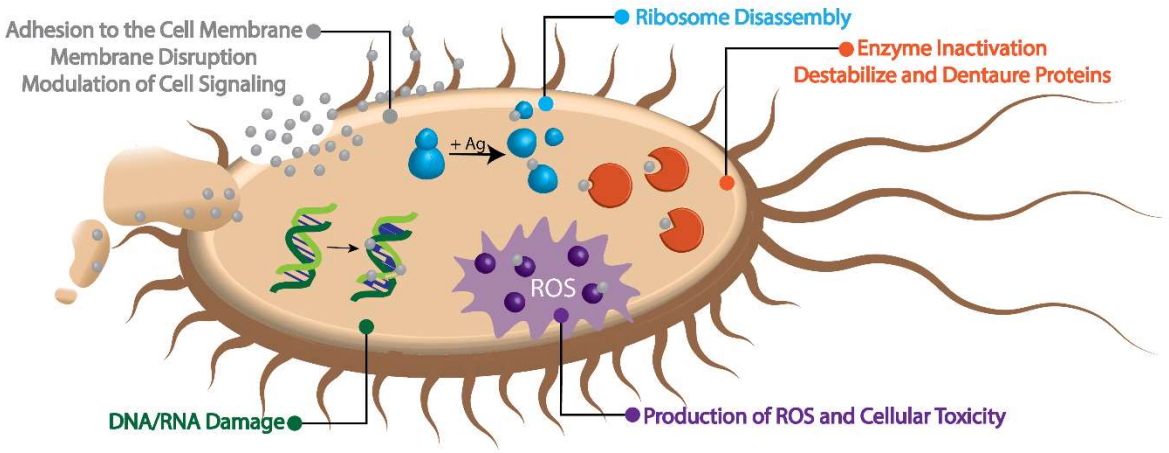

Figure 2: Schematic effect of AgNPs on bacterial cell.

Antibacterial properties of AgNPs

At very low concentrations, AgNPs inhibit bacterial growth, while remaining nontoxic to mammalian cells [20]. The anti-bacterial and anti-viral potential of AgNPs has sparked studies that elucidated the mechanisms of AgNPs' antimicrobial activity [34]. Antibacterial AgNPs are particularly appealing to combat multi-drug resistant bacteria, primarily due to the numerous mechanisms displayed when exposed to microbes. Colloidal silver and Ag^+ interact with bacterial cell walls in a way that disrupts the membrane and increases its permeability [3, 35, 36]. Increased permeability of the cell membrane allows AgNPs to penetrate through the cell. AgNPs tend to cluster together on the surface of the bacterial cell, creating holes or pits in the cell wall, ultimately causing bacterial cell death [7]. Additionally, AgNPs lead to the production of reactive oxygen species (ROS), which cause oxidative stress that reduces bacterial viability by damaging DNA, proteins, and other intracellular biomolecules (**Figure 2**) [4, 8, 14]. It is commonly understood that the biological properties of nanoscale materials greatly vary depending on the size, shape, and

structure of the particle [37]. These factors should therefore be considered during AgNP synthesis when they can be modulated. The size of AgNPs has a significant effect on ROS production with smaller nanoparticles leading to higher ROS levels [14]. The size and shape of AgNPs also determine the way in which they interact with light. Generally, these interactions are dominated by surface plasmon resonance by AgNPs as small as 2 nm in diameter [11, 38-40]. High proportions of surface area compared to particle volume likely contribute to the potent antibacterial properties of AgNPs assemblies. This is supported by the increased antibacterial efficacy of AgNPs as their size decreases [41, 42]. The shape of AgNPs also have a significant effect on their potency as antibacterial agents, with thinner plate-like structures typically performing the best (examples of different shapes are shown in **Figure 3**) [41, 43, 44]. The intended in-solution reactivity of AgNPs are additionally enhanced *via* surface chemistry and functionalization, helping to avoid toxicity or aggregation [45, 46]. Across similar bacterial strains, smaller AgNPs demonstrate a stronger antibacterial efficacy as compared to larger AgNPs [47].

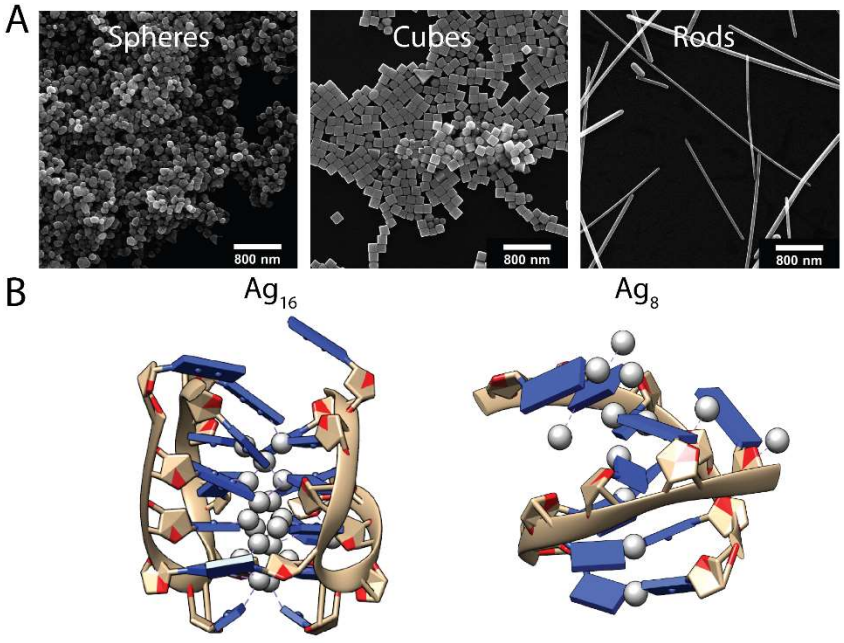

Figure 3: (A) Example silver nanoparticles are shown in a variety of shapes including spheres, cubes, and rods.[44] Copyright 2016, The Royal Society of Chemistry. (B) Crystal structures of two DNA-AgNCs with 16 or 8 Ag atoms in the cluster structures [48, 49].

Regardless of the multimodal antibacterial properties, which harbor advantages in comparison to traditional antibiotics, AgNPs are not without limitations, most notably heterogeneity and possible *in vivo* and *in vitro* cell toxicity [50, 51]. There are several reports describing a wide range of different AgNPs which vary greatly in synthesis methods, and importantly, in the methods of antibacterial studies. It remains very challenging to compare reported efficacies using different methodologies and materials [50]. AgNPs' toxicity towards human cells is highly dose-, size-, and time-dependent; additionally, long-term exposure is recognized to lead to chronic disorders of the skin and eyes [52, 53]. Furthermore, the synthesis of highly monodisperse AgNPs remains a challenge due to aggregation, which may significantly impact the biological activities and toxicity of AgNPs [54].

As with AgNPs, gold nanoparticles (AuNPs) are examined for their antibacterial efficacies [55, 56]. The size and dimensionality of AuNPs, which are varied by selected synthesis method, are strong contributing factors to their antimicrobial mechanisms. Most reports of significant bacterial inhibition induced by AuNPs include surface functionalization with antibiotics; these combinatorial treatments are effective at preventing bacteria from developing drug resistance [57]. Unlike AgNPs, AuNPs have photothermal properties due to their localized plasmon surface resonance. When a specific wavelength of light is absorbed by AuNPs, the energy is transformed to heat; this phenomenon is applied in cancer therapy to facilitate localized tumor cell death [58, 59]. Similarly, the plasmonic photothermal effect of AuNPs can be used to promote bacterial cell death. This has been successfully demonstrated using *Pseudomonas aeruginosa* in a suspension of AuNPs [60]. Following continuous exposure to a laser beam, bacterial viability is reduced. AgNPs are a convenient option as they do not require photon energy to destroy bacteria [61].

Physicochemical and antibacterial properties of DNA-AgNCs

In contrast to AgNPs, DNA-templated silver nanoclusters (DNA-AgNCs) are discreetly structured collections of only 5 – 30 silver atoms, and 2 nm in size. Although previous work has demonstrated the efficacy of DNA-AgNCs as antibiotics, further research is needed to elucidate the mechanism of antibacterial activity or correlate the inherent fluorescence properties of AgNCs to their biological activity. While it is commonly accepted that a significant contributor to the antibacterial efficacy of AgNPs is the production of ROS and the slow release of Ag^+ ions into solution, only ROS production has been implicated in DNA-AgNCs activity [3, 15, 17, 35]. This initial correlation indicates the need for further detailed studies of antibacterial mechanisms and identifying factors that can effectively modulate antibacterial activity, e.g., the relative age of the DNA-AgNCs, the arrangement of DNA-AgNCs in 3D space, and the changes in the local concentration of DNA-AgNCs. It is important to note that Ag^+ ions might be released from the DNA-AgNCs, but it is unlikely that the release of ions from the DNA-stabilized cluster is pH dependent within a physiologically relevant range, as DNA-AgNCs retain their fluorescence over a wide range of pH conditions [62]. In addition, DNA-AgNCs, which undergo significant changes to their fluorescence after aging for several weeks, can fully restore their fluorescence upon re-reduction with $NaBH_4$ [13]. Both of these observations imply a stable AgNC core which, while it may undergo changes in the oxidation state, likely does not change in cluster size or number of silver atoms [20]. The optical properties of AgNCs are generally dominated by fluorescence, which arises due to the molecule-like electronic structure of AgNCs [63].

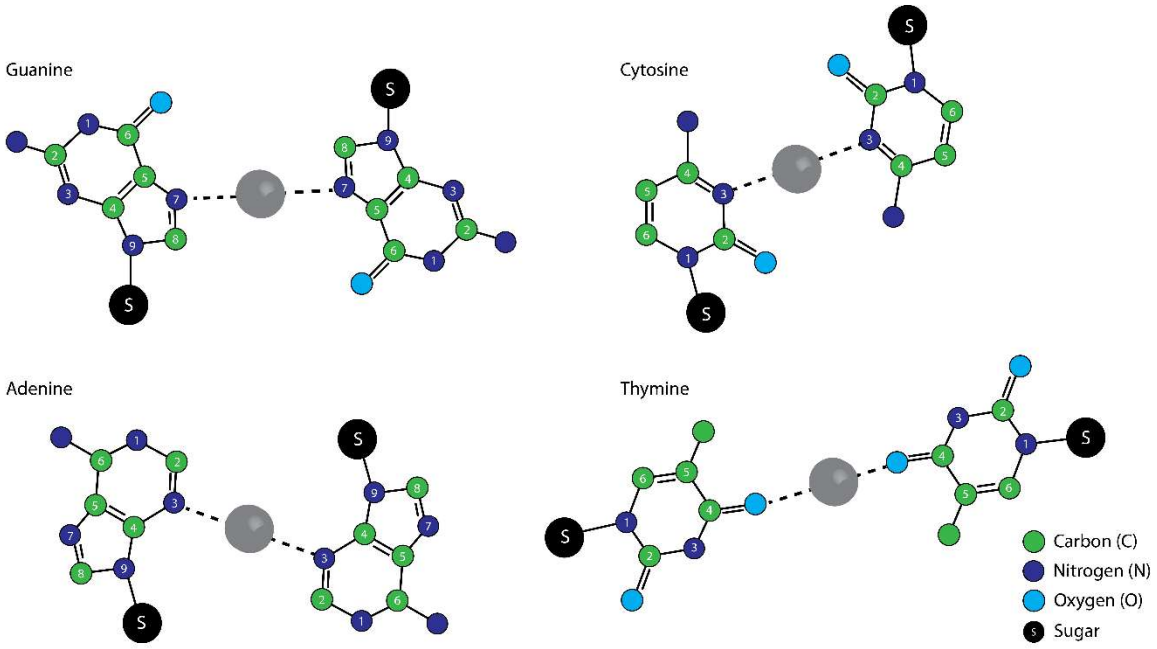

Figure 4: Schematic representation of silver binding to nucleic acid bases.

AgNCs formation can be templated by a variety of ligands, such as small molecules, polymers, and biomolecules [6, 63, 64]. If single-stranded (ss) nucleic acids, ssDNA or ssRNA, are used as templates, the size and fluorescence of resulting DNA-AgNCs can be regulated by the sequence of the templating oligonucleotide [2, 6, 20, 62-68]. Generally, DNA-AgNCs include cytosine-rich sections, as cytosine has the highest affinity for Ag^+ of the four DNA nucleobases (**Figure 4**) [64]. While ssDNA templates the formation of DNA-AgNCs, silver can also stabilize nucleic acid secondary structures, such as i-motifs and G-quadruplexes [64, 69-71].

Recently obtained crystal structures seem to support this by demonstrating the multidentate chelation of AgNCs by ssDNA in a manner that is consistent with the formation of dative bonds between endocyclic nitrogens or exocyclic oxygens of the nucleobases and silver atoms, as well as the formation of Ag–Ag bonds within the cluster [71, 72]. Two recent crystal structures shed light on the chemistry involved in the formation of DNA-AgNCs, revealing the formation of dative bonds between endocyclic nitrogen atoms which have accessible lone-pairs of electrons in the plane of

the nucleobase [71, 72]. On cytosine bases, this bond is formed with the N3 nitrogen. Other interactions, also likely to be dative bonds, are formed between the exocyclic O2 and N4 atoms, allowing the nucleobases and the entire oligonucleotide to act as a polydentate ligand in the chelation of silver atoms. In the case of the N4 atoms, it is possible that this involves the deprotonation of the N4 amine, as it is expected for the pK_a to be reduced in the presence of metal ions [71-73]. Similar interactions occur with the endocyclic N1 and exocyclic N6 nitrogen atoms of adenine [71, 72].

The antibacterial properties of DNA-AgNCs can be compared to those of AgNPs; however, DNA-AgNCs may harbor enhanced antibacterial characteristics as compared to their larger AgNP counterparts, due to increased stability and tunability of the DNA template [15]. Just as with AgNPs, the production of ROS is primarily associated with the antibacterial mechanisms of DNA-AgNCs [74]. The overproduced ROS damage bacterial DNA, and inhibits mitochondrial membrane potential, leading to apoptosis [75]. It is likely that there are other mechanisms at play, yet inclusive mechanistic studies of DNA-AgNC to bacterial cell interactions are still lacking. These DNA-AgNC bactericidal mechanisms include interference and damage of bacterial DNA, preventing replication [76]. Of particular interest is the positive correlation in the optical properties and antibacterial efficacies of DNA-AgNCs, both of which highly modifiable by tuning the oligonucleotide template sequence and length [20]. By taking advantage of this relationship, new approaches are taken for designing nanostructures capable of bacterial sensing and visualization as well as growth inhibition [77]. Although the inefficiency of DNA-AgNC fluorescence and limited shelf-life have presented as a challenge, precise modification of the templating oligonucleotide structure can result in increased stability and enhanced fluorescence [22]. DNA-AgNCs can be applied to demonstrate detection, reduction, and prevention of *P. Aeruginosa* biofilm growth, a finding that shows promise for the use of DNA-AgNCs in combating harmful bacterial biofilms without the risk of encouraging development of antibiotic resistance [78]. *P. Aeruginosa* are also used as a model for aptamer-functionalized DNA-AgNCs which displayed increased antibacterial

efficacies as compared to DNA-AgNCs not containing the *P. Aeruginosa*-specific aptamer [19]. DNA-AgNCs may be used in conjunction with the few antibiotics which remain effective against multi-drug resistant bacteria, in order to slow down or potentially prevent the bacterial species to develop resistance. This is demonstrated with daptomycin in combination with DNA-AgNCs to include multiple bactericidal mechanisms upon already multidrug-resistant *Staphylococcus aureus* [79]. Importantly, DNA-AgNCs are known to display significant antibacterial efficacy in low concentrations, and therefore are able to combat bacterial infection *in vivo* and *in vitro* without harming or displaying toxicity towards mammalian cells [20, 80]. Therefore, DNA-AgNCs for applications combating multi-drug resistance are not only comparable, but potentially preferable to AgNPs.

Table1: A comparison of AgNP and DNA-AgNC physicochemical properties

	AgNPs	DNA-AgNCs
Size	Up to 100 nm in size	Only about 2 nm in size
Synthesis requirements	Silver precursor, reducing agent, and a capping agent	Templating oligonucleotide, silver precursor, and reducing agent
Colloidal stability	Changes with various capping agents	Generally stable in solution due to templating DNA structures
Chemical stability	Addition of surfactants can modulate Ag^+ release from the surface	Ag^0 oxidizes to Ag^+ over time

Interaction with light	Efficient surface plasmon resonance photoeffect	Strong and adjustable fluorescence determined by DNA sequence and size
Particle uniformity	High polydispersity due to nonuniform particle synthesis	High batch-to-batch consistency

Computational studies of DNA-AgNCs

Various computational approaches can be applied to investigate stability of AgNCs, absorption and emission spectra, geometry of AgNCs, binding strength, and electrons transfer between DNA and AgNCs. The type of AgNCs for these studies vary by size, net charges, nanocluster geometry, and binding sites. Most theoretical research agrees with several discoveries, such that the shape of AgNCs bound to DNA is rod-like or thread-like and that electron population transfers between AgNCs and DNA. However, there are some discrepancies among research groups in binding strength, binding sites, and stability of complex between parallel and antiparallel strands DNAs.

Karimova, et al., investigate the absorption and circular dichroism (CD) spectra of neutral naked silver nanochains without any DNA components [81]. The size of the naked silver nanochains vary from 4 to 12 atoms. Although the optical absorption spectra of both planar and helical structures are similar, the planar structures show no CD signals while the helical structures produce strong CD spectra. In addition, the intensity and shape of the CD spectra are strongly influenced by helical geometry. The authors, agreeing with a report from Reveguk, et al., show that the spectrum redshifts and the peak intensity is enhanced as the number of silver atoms increases [82].

The interactions between a small size of AgNCs and bare DNA bases are studied by several research groups. Lee, et al., investigate the binding strength between a pair of silver atoms (Ag_2) and bare DNA bases [83]. The authors show that the binding strength of cytosine is highest, those

of both adenine and guanine are next, and that thymine is the weakest binder. Swasey, et al., studied the geometries and stabilities of Ag^+ mediated base pairing in homo-base deoxyoligonucleotides [84]. The authors report that the G-Ag^+-G ground state has highest binding energy with coplanar conformation, while that of C-Ag^+-C shows next highest binding energy with slightly bent coplanar geometry. Additionally, Ag^+ bridges to the N7 atom of guanine and the N3 atom in cytosine. In contrast, both A-Ag^+-A and T-Ag^+-T show twisted non-coplanar geometry with small binding energy which explains why Ag^+ mediated adenine and thymine homo-base pairs are not observed experimentally. Srivastava, et al., investigate the binding of the neutral Ag_nNCs (n = 8, 10, 12) to adenine, guanine, and Watson-Crick (WC) A:T and G:C base pairs [85]. The authors show that the binding strength of AgNCs in the WC base pair is stronger than those of isolated DNA complexes. In addition, the electron charge is transferred from the DNA/WC bases to the AgNCs. The specific interactions between AgNCs and guanine are studied by two research groups. Dale, et al., found that the neutral AgNCs prefer to bind to the π system or N3 atom while all cationic and dicationic AgNCs are favored to bind N7, oxygen, and carbonyl groups [86]. Interestingly, the Ag_5^+−guanine complex forms a trapezoid-like AgNC which was also captured by crystal structure [71]. Chen, et al., research Ag^+ mediated cytosine and guanine homo-bases and they found that both cytosine and guanine form stable parallel Ag^+ mediated double helix due to interplanar hydrogen bond interactions [87-89].

The AgNCs bound to DNA strands and their emissions are analyzed by several research groups. Ramazanov, et al. study the geometry and excitation spectra of neutral and charged silver atoms bound to single DNA bases and dC3 oligomers [90]. The authors show that the absorption spectra of planar AgNCs bound to N atoms of DNA bases are weak and do not match the excitation spectra of the emitting AgNCs. However, excitation spectra of the threadlike AgNCs are similar to those of observed fluorescent polymer-stabilized AgNCs. Furthermore, the authors show that the excitation spectrum of threadlike analogs in the minor groove in the dC3 oligomer is well matched to the fluorescence excitation spectrum of green emitting clusters. However, the

computational studies show that the Ag_3^{+1} cluster binds to oxygen atoms on phosphates while most other computational studies propose that AgNCs bind nitrogen atoms in cytosine or guanine [83-86, 89]. Ramazamov, et al. also report the fluorescence excitation spectra of a planar (Ag_3^+) and a zigzag (Ag_4^+) clusters bound to a 12-mer DNA [91]. Their QM/MM-MD simulations show that the planar Ag_3^+ emits violet and green lights when it is bound to the DNA hairpin loop and cytosine rich site, respectively. The zigzag Ag_4^+ bound to DNA T-T mismatch site emits red spectra. As the source of the excited state of the complex, they show that charges transfer from AgNCs to DNA. Lisinetskaya, et al. also assess the emission spectrum of planar Ag_3^+ clusters bound to CT_2 and C_4 units as well as a DNA hairpin in which CT_2 and C_4 form a dimer [92]. The authors report that two peaks at 3.47 eV and 3.69 eV in the emission spectrum of the dimer at the excitation energy of 3.69 eV are from $Ag_3^+C_4$ and $Ag_3^+CT_2$, respectively. They show that the 3.69 eV laser pulse induces the electron population transfer to the S_1 state of $Ag_3^+CT_2$ and the S_2 state of $Ag_3^+C_4$. However, when the 3.47 eV laser pulse is tested, no coupled excited state, as well as no energy transfer, between the AgNCs is observed.

Chen, et al., report three DNA-AgNCs with six to eight silver atoms bound to C_6-C_6 duplex [93]. All central silver cores bind to N3 atoms in cytosine whereas no oxygen binds to silver. In addition, the conformations of all core silver atoms show two-row planar shape which bridges DNA strands. Interestingly, their computational work shows a trapezoidal conformation of the Ag_5 core which was also found in the X-ray structure [71]. In the crystal structure, the Ag_8 cluster is bound to a cytosine rich (A_2C_4) oligonucleotide where the Ag_5 core forms a trapezoidal structure. In addition, the authors identify the source of first peaks in the optical absorption spectra and CD are due to the transitions between HOMO state in silver atoms and the unoccupied states in the DNA moiety. Therefore, their computational studies support the results that the low-energy peaks in the optical spectra and CD are due to the electronic transitions from Ag atoms to the DNA.

As described above, most theoretical research groups agree that the AgNCs bound to DNA form a rod-like or thread-like shape [81, 82, 86, 90, 91, 93-98]. In addition, most theoretical research groups

agree on the charge transition between AgNCs and DNA. The charges transfer from DNA to neutral AgNCs [85, 90, 98] while charge transitions occur from charged AgNCs to DNA [90-93]. In contrast, the major discrepancy among the theoretical research groups is the stability of DNA-AgNCs clusters complex in parallel and antiparallel DNA duplex. Chen, et al. show that the parallel duplex is more stable than the antiparallel duplex in terms of helical geometry and hydrogen bond interactions [88]. The stability of DNA-AgNCs complexes by parallel strands is also found by other research groups [99-102]. However, the antiparallel silver-mediated double-helix structure, in the study of Kondo, et al., matches well with the crystal structure [103]. In addition, Reveguk, et al., show the fluorescence activation due to the neutral AgNC (Ag_4) mediated two short antiparallel cytosine rich DNA duplexes formation [82]. They also show the optical spectrum shift to red due to an increase of energy of the S1 as the size of the AgNC increases, which is also apparent in isolated silver nanochains [81]. Xu, et al. and Toomey, et al. also report experimental evidence of AgNC mediated antiparallel strands [104, 105]. The question of how parallel and antiparallel strands affect the stability of DNA-AgNC complexes remains to be answered.

Optical properties

The major light interaction that takes place between light in the UV-Vis range and AgNPs is absorption *via* surface plasmon resonance [11, 39, 40, 106]. The most efficiently absorbed wavelength is dependent on size and shape of the AgNP. Rod-like AgNPs with high aspect ratios can have multiple absorption peaks corresponding to the longitudinal and transverse modes along the nanorod. Spherical AgNPs tend to only show a single absorbance peak [11]. It is also key to note that the ligand used to stabilize the surface of the AgNPs can significantly impact the strength of the absorbance peaks [11, 106]. AgNPs also have a significantly higher absorptivity than gold or platinum nanoparticles, which make AgNPs particularly easy to track spectroscopically [107].

The major peak in the UV-Vis absorbance spectra of DNA-AgNCs occurs at 260 nm [20]. Absorbance of 260 nm light is anticipated with nucleic acids, and is largely dominated by π–π*

transitions [108, 109]. DNA-AgNCs are excited with both UV light, generally near 260 nm, and visible light, generally with a wavelength 50 nm – 150 nm less than the peak emission wavelength [110]. The absorbance of 260 nm light by DNA-AgNCs is likely to be slightly enhanced by the presence of the AgNCs [110, 111]. The excitation of DNA-AgNCs with either of these wavelengths can lead to nearly identical emission spectra. The implication of these results is that both excited states relax to the same lowest energy excited state prior to emission. Computational results simulating AgNCs with 13 silver atoms ligated by 12 cytosines predict that the complex has a semiconductor-like band gap, close to 2 eV, with charges of +5 or greater, corresponding to one of the experimentally observed 'magic color' emission near 630 nm (2 eV converts to 620 nm) [112, 113]. Interestingly, this DNA-AgNC with a +5 charge on the AgNC moiety does correspond to one of the magic numbers predicted for metal superatoms with a closed shell of 8 electrons. It is important to note in this determination that cytosines (and presumably other nucleobases) are not considered electron withdrawing ligands [112].

Metal clusters in general have a "magic number" of neutral atoms which are stable due to the formation of closed electron shells following the cluster shell model [23, 113-115]. This is not always the case with small AgNCs, however. Recent reports demonstrate stable AgNCs formed with open shell electronic structures [71, 116]. From an analysis of DNA-AgNCs with well characterized clusters, the 'magic numbers' of Ag^0 are often found to be 4 and 6. Ag^0=4 typically corresponds to 'green' fluorescent clusters, and Ag^0=6 corresponds to 'red' fluorescent clusters, and while the total cluster size, Ag^0 and Ag^+, varies [113]. These magic numbers correspond to what the Gwinn group dub 'magic colors' of 'red' ~ 630 nm and 'green' ~ 540 nm [113]. These clusters may not be subject to the same constraints as spherical metal clusters (stable valence electron magic numbers of 2, 8, 18, 20, etc.), as expected, and recently confirmed via two crystal structures, that DNA-AgNCs generally assume rod-like cluster shapes which are better described by an ellipsoidal shell model [71, 72, 113, 117, 118].

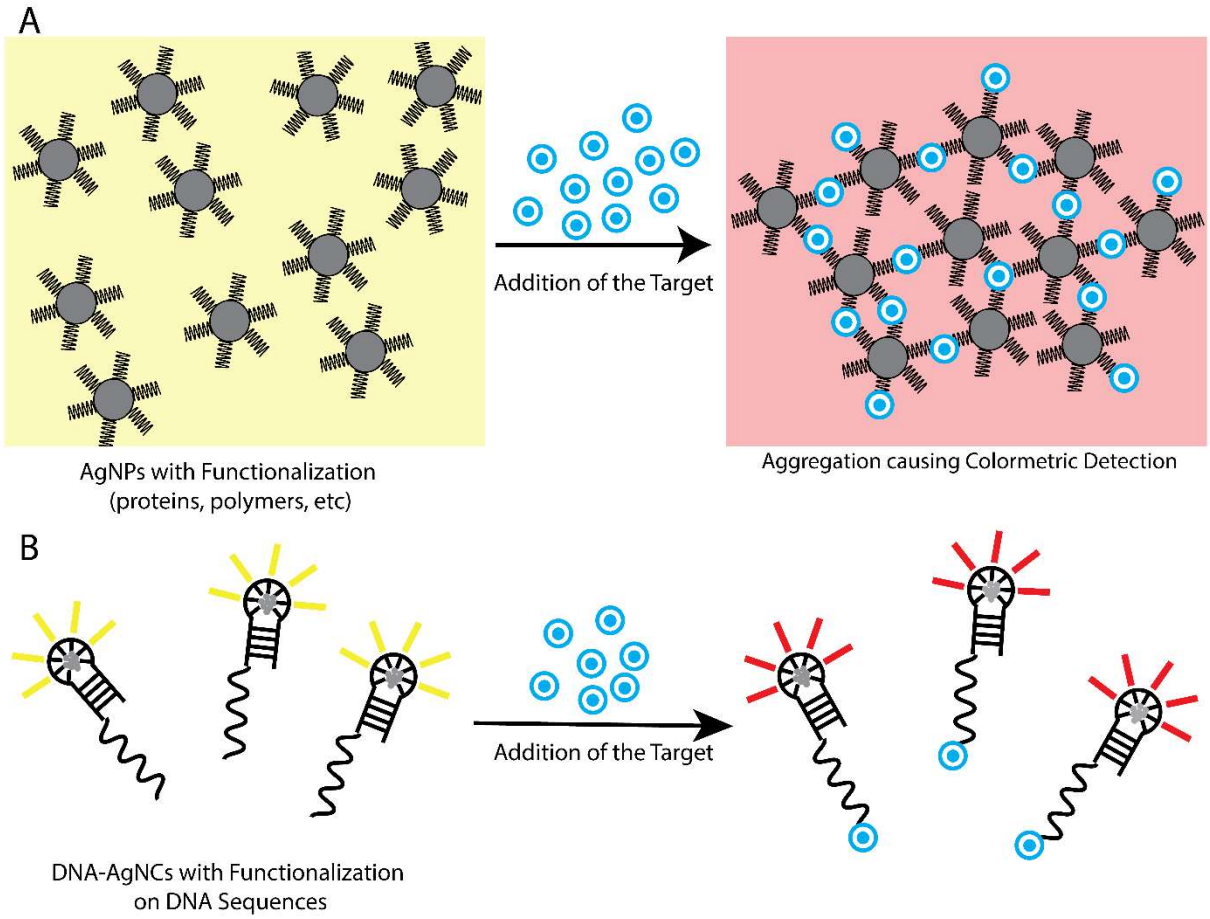

Figure 5: Schematic representation of biosensing techniques by AgNPs (**A**) and DNA-AgNCs (**B**). (**Ai**) Interaction between the functionalization and the target causes a change in fluorescence. (**Aii**) The target links multiple AgNPs together to increase the fluorescence signal. (**B**) DNA is functionalized at the 3' or 5' end to interact with specific targets to cause a change in fluorescence.

Applications as Biosensors

The use of AgNPs as biosensors for diagnostic testing and biomolecular detection has slowly begun to expand, with AgNPs in the center of the development to sense the presence of a variety of biomolecules. For example, AgNPs are utilized for detecting small molecules, such as dipicolinate, a sign of the presence of *Bacillus anthracis*, in a platform presented by Chrimes, et al. This system employs the AgNPs as a surface-enhanced Raman scattering substrate and

intensifies the Raman scattering signal of the passively-adsorbed dipicolinate [119]. Other groups take advantage of the peroxidase-like catalysis that AgNP nanozymes offer to develop colorimetric assays, as demonstrated by Jiang, et al., who uses their platform to detect glucose [120]. Moreover, the high available surface area on smaller AgNPs allows for attachment of surface functional groups (**Figure 5A**), which can be incorporated to achieve binding and biosensing dependent on the presence of a certain target. Other examples include the use of plasmonic AgNPs to sense melamine [121, 122], tryptophan [123], and many other targets [124-130].

A significant advantage of using DNA-AgNCs is the ability to modify the nucleic acid template to detect endogenous nucleic acids in a sequence specific manner. This approach has yielded powerful probes for detecting disease-associated oligonucleotides. Fredrick, et al. demonstrate a system in which the association of two strands with miR-371, a biomarker which tends to be overabundant in prostate cancers, leads to a shift in the fluorescence pattern of AgNCs templated on a substrate oligo. The system was able to reliably detect as little as 22 pmol of miR-371 [131]. Other DNA-AgNC-based biosensors are designed to detect a wide array of substrates such as virus-associated nucleic acids and microRNAs [132-134]. DNA-AgNCs are not limited to detecting oligonucleotides; they can detect pathogenic bacteria, disease antigens, and many other substrates [135-138]. As depicted in **Figure 5B**, DNA-AgNCs may be decorated with specific sequences to allow for target-dependent fluorescence.

Future Perspective

The incorporation of silver in nanomedicine has thus far been primarily focused in the direction of sterilization of tools and preventing infection of open wounds. Frequent use of antibiotic drugs comes with the risk of encouraging development of antibiotic resistance in harmful bacterial species. The multivalent antibacterial activities of AgNPs and DNA-AgNCs are advantageous for use in sterile settings as bacteria are more likely to effectively evolve against mechanisms which inhibit bacterial viability *via* a certain and specific method. As of recently, wound dressings which

incorporate AgNPs are increasingly developed so that reliance on antibiotics may be avoided [139]. However, the unique composition of biocompatible DNA-AgNCs and programmability of DNA can allow for AgNCs to become readily incorporated in larger, multifunctional nucleic acid nanoparticles (NANPs) [13] that can be further programmed to specifically target certain bacteria strains *in vivo*. This combinatorial technology can open unforeseen possibilities for silver nanomaterials and significantly accelerate their translation into the clinical settings.

Executive Summary

Antibacterial properties of AgNPs

- The antibacterial mechanisms of AgNPs are well characterized.
- Despite their limitations, AgNPs may be advantageous over other nanomaterials, such as gold nanoparticles (AuNPs).

Physicochemical and antibacterial properties of DNA-AgNCs

- The size and resulting fluorescence of AgNCs are determined by the templating DNA sequence.
- Crystal structures of DNA-AgNCs indicate that silver atoms contribute to a more stable DNA secondary structure.
- By repeating reduction of DNA-AgNCs, fluorescence that has changed due to oxidation can be restored.
- DNA-AgNCs harbor antibacterial mechanisms that are yet to be comprehensively investigated.
- DNA-AgNCs display enhanced antibacterial efficacies as compared to AgNPs.

Computational studies of DNA-AgNCs

- Silver atoms have the highest binding affinity for cytosine, show the lowest binding strength for thymine

- Absorption and circular dichroism spectra demonstrate that peak intensities of AgNCs increase with the number of silver atoms.
- Most DNA-AgNCs are of a rodlike or threadlike structure.
- The stability of DNA-AgNCs may be impacted by the incorporation of parallel or antiparallel DNA duplexes.

Optical properties

- AgNPs absorb light efficiently at varying wavelengths contingent on size and shape of the AgNPs.
- The emission wavelength of AgNCs is dependent on the number of silver atoms on the DNA template.

Applications as Biosensors

- AgNPs are applied as detection systems for targeted biomolecules.
- The tunable fluorescence of DNA-AgNCs is useful for the detecting of pathogenic or damaged oligonucleotide sequences.

Future Perspective

- Due to their multimodal antibacterial activities, AgNPs and DNA-AgNCs are strong assets to face the challenge of drug-resistant bacteria.

Acknowledgements:

Research reported in this publication was supported by the National Institute of General Medical Sciences of the National Institutes of Health under award number R35GM139587 (to K.A.A.). The content is solely the responsibility of the authors and does not necessarily represent the official views of the National Institutes of Health.

References

1. Ranoszek-Soliwoda, K.; Tomaszewska, E.; Socha, E.; Krzyczmonik, P.; Ignaczak, A.; Orlowski, P.; Krzyzowska, M.; Celichowski, G.; Grobelny, J., The role of tannic acid and

sodium citrate in the synthesis of silver nanoparticles. *Journal of Nanoparticle Research* **2017,** *19* (8).
2. Gwinn, E. G.; O'Neill, P.; Guerrero, A. J.; Bouwmeester, D.; Fygenson, D. K., Sequence-Dependent Fluorescence of DNA-Hosted Silver Nanoclusters. *Advanced Materials* **2008,** *20* (2), 279-283.
3. Möhler, J. S.; Sim, W.; Blaskovich, M. A. T.; Cooper, M. A.; Ziora, Z. M., Silver bullets: A new lustre on an old antimicrobial agent. *Biotechnology Advances* **2018,** *36* (5), 1391-1411.
4. Morones-Ramirez, J. R.; Winkler, J. A.; Spina, C. S.; Collins, J. J., Silver Enhances Antibiotic Activity Against Gram-Negative Bacteria. *Science Translational Medicine* **2013,** *5* (190), 190ra81-190ra81.
5. Afonin, K. A.; Schultz, D.; Jaeger, L.; Gwinn, E.; Shapiro, B. A., Silver Nanoclusters for RNA Nanotechnology: Steps Towards Visualization and Tracking of RNA Nanoparticle Assemblies. Springer New York: 2015; pp 59-66.
6. Xie, Y.-P.; Shen, Y.-L.; Duan, G.-X.; Han, J.; Zhang, L.-P.; Lu, X., Silver nanoclusters: synthesis, structures and photoluminescence. *Materials Chemistry Frontiers* **2020,** *4* (8), 2205-2222.
7. Sondi, I.; Salopek-Sondi, B., Silver nanoparticles as antimicrobial agent: a case study on E-coli as a model for Gram-negative bacteria. *JOURNAL OF COLLOID AND INTERFACE SCIENCE* **2004,** *275* (1), 177-182.
8. Flores-López, L. Z.; Espinoza-Gómez, H.; Somanathan, R., Silver nanoparticles: Electron transfer, reactive oxygen species, oxidative stress, beneficial and toxicological effects. Mini review. *Journal of Applied Toxicology* **2019,** *39* (1), 16-26.
9. Chen, J.; Chen, Q.; Gao, C.; Zhang, M.; Qin, B.; Qiu, H., A SiO2 NP–DNA/silver nanocluster sandwich structure-enhanced fluorescence polarization biosensor for amplified detection of hepatitis B virus DNA. *Journal of Materials Chemistry B* **2015,** *3* (6), 964-967.
10. Desai, R.; Mankad, V.; Gupta, S. K.; Jha, P. K., Size Distribution of Silver Nanoparticles: UV-Visible Spectroscopic Assessment. *Nanoscience and Nanotechnology Letters* **2012,** *4* (1), 30-34.
11. Liu, F.-K.; Ko, F.-H.; Huang, P.-W.; Wu, C.-H.; Chu, T.-C., Studying the size/shape separation and optical properties of silver nanoparticles by capillary electrophoresis. *Journal of Chromatography A* **2005,** *1062* (1), 139-145.
12. Yang, L.; Yao, C.; Li, F.; Dong, Y.; Zhang, Z.; Yang, D., Synthesis of Branched DNA Scaffolded Super-Nanoclusters with Enhanced Antibacterial Performance. *Small* **2018,** *14* (16), 1800185.
13. Yourston, L.; Rolband, L.; West, C.; Lushnikov, A.; Afonin, K. A.; Krasnoslobodtsev, A. V., Tuning properties of silver nanoclusters with RNA nanoring assemblies. *Nanoscale* **2020,** *12* (30), 16189-16200.
14. Carlson, C.; Hussain, S. M.; Schrand, A. M.; K. Braydich-Stolle, L.; Hess, K. L.; Jones, R. L.; Schlager, J. J., Unique Cellular Interaction of Silver Nanoparticles: Size-Dependent Generation of Reactive Oxygen Species. *The Journal of Physical Chemistry B* **2008,** *112* (43), 13608-13619.
15. Javani, S.; Lorca, R.; Latorre, A.; Flors, C.; Cortajarena, A. L.; Somoza, Á., Antibacterial Activity of DNA-Stabilized Silver Nanoclusters Tuned by Oligonucleotide Sequence. *ACS Applied Materials & Interfaces* **2016,** *8* (16), 10147-10154.
16. Sim, W.; Barnard, R.; Blaskovich, M. A. T.; Ziora, Z., Antimicrobial Silver in Medicinal and Consumer Applications: A Patent Review of the Past Decade (2007–2017). *Antibiotics* **2018,** *7* (4), 93.
17. Tian, X.; Jiang, X.; Welch, C.; Croley, T. R.; Wong, T.-Y.; Chen, C.; Fan, S.; Chong, Y.; Li, R.; Ge, C.; Chen, C.; Yin, J.-J., Bactericidal Effects of Silver Nanoparticles on Lactobacilli and the Underlying Mechanism. *ACS Applied Materials & Interfaces* **2018,** *10* (10), 8443-8450.

18. Lyu, D.; Li, J.; Wang, X.; Guo, W.; Wang, E., Cationic-Polyelectrolyte-Modified Fluorescent DNA–Silver Nanoclusters with Enhanced Emission and Higher Stability for Rapid Bioimaging. *Analytical Chemistry* **2019,** *91* (3), 2050-2057.
19. Soundy, J.; Day, D., Delivery of antibacterial silver nanoclusters to Pseudomonas aeruginosa using species-specific DNA aptamers. *Journal of Medical Microbiology* **2020,** *69* (4), 640-652.
20. Rolband, L.; Yourston, L.; Chandler, M.; Beasock, D.; Danai, L.; Kozlov, S.; Marshall, N.; Shevchenko, O.; Krasnoslobodtsev, A. V.; Afonin, K. A., DNA-Templated Fluorescent Silver Nanoclusters Inhibit Bacterial Growth While Being Non-Toxic to Mammalian Cells. *Molecules* **2021,** *26* (13), 4045.
21. Li, J.; Liu, W.; Wu, X.; Gao, X., Mechanism of pH-switchable peroxidase and catalase-like activities of gold, silver, platinum and palladium. *Biomaterials* **2015,** *48*, 37-44.
22. Eun, H.; Kwon, W. Y.; Kalimuthu, K.; Kim, Y.; Lee, M.; Ahn, J.-O.; Lee, H.; Lee, S. H.; Kim, H. J.; Park, H. G.; Park, K. S., Melamine-promoted formation of bright and stable DNA–silver nanoclusters and their antimicrobial properties. *Journal of Materials Chemistry B* **2019,** *7* (15), 2512-2517.
23. Desireddy, A.; Conn, B. E.; Guo, J.; Yoon, B.; Barnett, R. N.; Monahan, B. M.; Kirschbaum, K.; Griffith, W. P.; Whetten, R. L.; Landman, U.; Bigioni, T. P., Ultrastable silver nanoparticles. *Nature* **2013,** *501* (7467), 399-402.
24. Ventola, C. L., The antibiotic resistance crisis: part 1: causes and threats. *P T* **2015,** *40* (4), 277-83.
25. Jackson, N.; Czaplewski, L.; Piddock, L. J. V., Discovery and development of new antibacterial drugs: learning from experience? *J Antimicrob Chemother* **2018,** *73* (6), 1452-1459.
26. Silver, S.; Phung, L. T.; Silver, G., Silver as biocides in burn and wound dressings and bacterial resistance to silver compounds. *Journal of Industrial Microbiology & Biotechnology* **2006,** *33* (7), 627-634.
27. Chernousova, S.; Epple, M., Silver as Antibacterial Agent: Ion, Nanoparticle, and Metal. *Angewandte Chemie International Edition* **2013,** *52* (6), 1636-1653.
28. Hoffman, R. K.; Surkiewicz, B. F.; Chambers, L. A.; Phillips, C. R., Bactericidal Action of Movidyn. *Industrial & Engineering Chemistry* **1953,** *45* (11), 2571-2573.
29. Fong, J.; Wood, F., Nanocrystalline silver dressings in wound management: a review. *Int J Nanomedicine* **2006,** *1* (4), 441-9.
30. Sondi, I.; Salopek-Sondi, B., Silver nanoparticles as antimicrobial agent: a case study on E. coli as a model for Gram-negative bacteria. *J Colloid Interface Sci* **2004,** *275* (1), 177-82.
31. Gupta, A.; Mumtaz, S.; Li, C.-H.; Hussain, I.; Rotello, V. M., Combatting antibiotic-resistant bacteria using nanomaterials. *Chemical Society Reviews* **2019,** *48* (2), 415-427.
32. Hajipour, M. J.; Fromm, K. M.; Ashkarran, A. A.; Jimenez de Aberasturi, D.; de Larramendi, I. R.; Rojo, T.; Serpooshan, V.; Parak, W. J.; Mahmoudi, M., Antibacterial properties of nanoparticles. *Trends Biotechnol* **2012,** *30* (10), 499-511.
33. Zhang, X.-F.; Liu, Z.-G.; Shen, W.; Gurunathan, S., Silver Nanoparticles: Synthesis, Characterization, Properties, Applications, and Therapeutic Approaches. *Int J Mol Sci* **2016,** *17* (9), 1534.
34. Bruna, T.; Maldonado-Bravo, F.; Jara, P.; Caro, N., Silver Nanoparticles and Their Antibacterial Applications. *Int J Mol Sci* **2021,** *22* (13).
35. Mathur, P.; Jha, S.; Ramteke, S.; Jain, N., Pharmaceutical aspects of silver nanoparticles. *Artificial cells, nanomedicine, and biotechnology* **2018,** *46* (sup1), 115-126.
36. Sorinolu, A. J.; Godakhindi, V.; Siano, P.; Vivero-Escoto, J. L.; Munir, M., Influence of silver ion release on the inactivation of antibiotic resistant bacteria using light-activated silver nanoparticles. *Materials Advances* **2022,** *3* (24), 9090-9102.

37. Morones, J. R.; Elechiguerra, J. L.; Camacho, A.; Holt, K.; Kouri, J. B.; Ramírez, J. T.; Yacaman, M. J., The bactericidal effect of silver nanoparticles. *Nanotechnology* **2005,** *16* (10), 2346.
38. Alfagih, I. M.; Aldosari, B.; Alquadeib, B.; Almurshedi, A.; Alfagih, M. M., Nanoparticles as adjuvants and nanodelivery systems for mRNA-based vaccines. *Pharmaceutics* **2021,** *13* (1), 1-27.
39. Vodnik, V. V.; Božanić, D. K.; Bibić, N.; Šaponjić, Z. V.; Nedeljković, J. M., Optical Properties of Shaped Silver Nanoparticles. *Journal of Nanoscience and Nanotechnology* **2008,** *8* (7), 3511-3515.
40. González, A. L.; Noguez, C., Optical properties of silver nanoparticles. *physica status solidi (c)* **2007,** *4* (11), 4118-4126.
41. Tang, S.; Zheng, J., Antibacterial Activity of Silver Nanoparticles: Structural Effects. *Advanced Healthcare Materials* **2018,** *7* (13), 1701503.
42. Agnihotri, S.; Mukherji, S.; Mukherji, S., Size-controlled silver nanoparticles synthesized over the range 5–100 nm using the same protocol and their antibacterial efficacy. *RSC Adv.* **2014,** *4* (8), 3974-3983.
43. Pal, S.; Tak Yu, K.; Song Joon, M., Does the Antibacterial Activity of Silver Nanoparticles Depend on the Shape of the Nanoparticle? A Study of the Gram-Negative Bacterium Escherichia coli. *Applied and Environmental Microbiology* **2007,** *73* (6), 1712-1720.
44. Helmlinger, J.; Sengstock, C.; Groß-Heitfeld, C.; Mayer, C.; Schildhauer, T. A.; Köller, M.; Epple, M., Silver nanoparticles with different size and shape: equal cytotoxicity, but different antibacterial effects. *RSC Advances* **2016,** *6* (22), 18490-18501.
45. Samberg, M. E.; Oldenburg, S. J.; Monteiro-Riviere, N. A., Evaluation of silver nanoparticle toxicity in skin in vivo and keratinocytes in vitro. *Environ Health Perspect* **2010,** *118* (3), 407-13.
46. El Badawy, A. M.; Silva, R. G.; Morris, B.; Scheckel, K. G.; Suidan, M. T.; Tolaymat, T. M., Surface Charge-Dependent Toxicity of Silver Nanoparticles. *Environmental Science & Technology* **2011,** *45* (1), 283-287.
47. Baker, C.; Pradhan, A.; Pakstis, L.; Pochan, D. J.; Shah, S. I., Synthesis and antibacterial properties of silver nanoparticles. *Journal of nanoscience and nanotechnology* **2005,** *5* (2), 244-249.
48. Huard, D. J. E.; Demissie, A.; Kim, D.; Lewis, D.; Dickson, R. M.; Petty, J. T.; Lieberman, R. L., Atomic Structure of a Fluorescent Ag₈ Cluster Templated by a Multistranded DNA Scaffold. *Journal of the American Chemical Society* **2019,** *141* (29), 11465-11470.
49. Cerretani, C.; Kanazawa, H.; Vosch, T.; Kondo, J., Crystal structure of a NIR-Emitting DNA-Stabilized Ag ₁₆ Nanocluster. *Angewandte Chemie International Edition* **2019,** *58* (48), 17153-17157.
50. Duval, R. E.; Gouyau, J.; Lamouroux, E., Limitations of Recent Studies Dealing with the Antibacterial Properties of Silver Nanoparticles: Fact and Opinion. *Nanomaterials* **2019,** *9* (12), 1775.
51. Liao, C.; Li, Y.; Tjong, S. C., Bactericidal and Cytotoxic Properties of Silver Nanoparticles. *Int J Mol Sci* **2019,** *20* (2), 449.
52. Jiang, X.; Lu, C.; Tang, M.; Yang, Z.; Jia, W.; Ma, Y.; Jia, P.; Pei, D.; Wang, H., Nanotoxicity of Silver Nanoparticles on HEK293T Cells: A Combined Study Using Biomechanical and Biological Techniques. *ACS Omega* **2018,** *3* (6), 6770-6778.
53. Carrola, J.; Bastos, V.; Jarak, I.; Oliveira-Silva, R.; Malheiro, E.; Daniel-da-Silva, A. L.; Oliveira, H.; Santos, C.; Gil, A. M.; Duarte, I. F., Metabolomics of silver nanoparticles toxicity in HaCaT cells: structure–activity relationships and role of ionic silver and oxidative stress. *Nanotoxicology* **2016,** *10* (8), 1105-1117.

54. Bélteky, P.; Rónavári, A.; Igaz, N.; Szerencsés, B.; Tóth, I. Y.; Pfeiffer, I.; Kiricsi, M.; Kónya, Z., Silver nanoparticles: aggregation behavior in biorelevant conditions and its impact on biological activity. *Int J Nanomedicine* **2019,** *14*, 667-687.
55. Shamaila, S.; Zafar, N.; Riaz, S.; Sharif, R.; Nazir, J.; Naseem, S., Gold Nanoparticles: An Efficient Antimicrobial Agent against Enteric Bacterial Human Pathogen. *Nanomaterials (Basel)* **2016,** *6* (4).
56. Okkeh, M.; Bloise, N.; Restivo, E.; De Vita, L.; Pallavicini, P.; Visai, L., Gold Nanoparticles: Can They Be the Next Magic Bullet for Multidrug-Resistant Bacteria? *Nanomaterials (Basel)* **2021,** *11* (2).
57. Su, C.; Huang, K.; Li, H.-H.; Lu, Y.-G.; Zheng, D.-L., Antibacterial Properties of Functionalized Gold Nanoparticles and Their Application in Oral Biology. *Journal of Nanomaterials* **2020,** *2020*, 5616379.
58. Ali, M. R. K.; Wu, Y.; El-Sayed, M. A., Gold-Nanoparticle-Assisted Plasmonic Photothermal Therapy Advances Toward Clinical Application. *The Journal of Physical Chemistry C* **2019,** *123* (25), 15375-15393.
59. Gharatape, A.; Davaran, S.; Salehi, R.; Hamishehkar, H., Engineered gold nanoparticles for photothermal cancer therapy and bacteria killing. *RSC Advances* **2016,** *6* (112), 111482-111516.
60. Al-Bakri, A. G.; Mahmoud, N. N., Photothermal-Induced Antibacterial Activity of Gold Nanorods Loaded into Polymeric Hydrogel against Pseudomonas aeruginosa Biofilm. *Molecules* **2019,** *24* (14).
61. Zhou, Y.; Kong, Y.; Kundu, S.; Cirillo, J. D.; Liang, H., Antibacterial activities of gold and silver nanoparticles against Escherichia coli and bacillus Calmette-Guérin. *J Nanobiotechnology* **2012,** *10*, 19.
62. Gambucci, M.; Cerretani, C.; Latterini, L.; Vosch, T., The effect of pH and ionic strength on the fluorescence properties of a red emissive DNA-stabilized silver nanocluster. *Methods and Applications in Fluorescence* **2019,** *8* (1), 014005.
63. Díez, I.; Ras, R. H. A., Fluorescent silver nanoclusters. *Nanoscale* **2011,** *3* (5), 1963.
64. New, S. Y.; Lee, S. T.; Su, X. D., DNA-templated silver nanoclusters: structural correlation and fluorescence modulation. *Nanoscale* **2016,** *8* (41), 17729-17746.
65. Yin, N.; Yuan, S.; Zhang, M.; Wang, J.; Li, Y.; Peng, Y.; Bai, J.; Ning, B.; Liang, J.; Gao, Z., An aptamer-based fluorometric zearalenone assay using a lighting-up silver nanocluster probe and catalyzed by a hairpin assembly. *Microchimica Acta* **2019,** *186* (12).
66. Chandler, M.; Shevchenko, O.; Vivero-Escoto, J. L.; Striplin, C. D.; Afonin, K. A., DNA-Templated Synthesis of Fluorescent Silver Nanoclusters. *Journal of Chemical Education* **2020,** *97* (7), 1992-1996.
67. Guo, W.; Yuan, J.; Dong, Q.; Wang, E., Highly Sequence-Dependent Formation of Fluorescent Silver Nanoclusters in Hybridized DNA Duplexes for Single Nucleotide Mutation Identification. *Journal of the American Chemical Society* **2010,** *132* (3), 932-934.
68. O'Neill, P. R.; Velazquez, L. R.; Dunn, D. G.; Gwinn, E. G.; Fygenson, D. K., Hairpins with Poly-C Loops Stabilize Four Types of Fluorescent Agn:DNA. *The Journal of Physical Chemistry C* **2009,** *113* (11), 4229-4233.
69. Ai, J.; Guo, W.; Li, B.; Li, T.; Li, D.; Wang, E., DNA G-quadruplex-templated formation of the fluorescent silver nanocluster and its application to bioimaging. *Talanta* **2012,** *88*, 450-455.
70. Sengupta, B.; Springer, K.; Buckman, J. G.; Story, S. P.; Abe, O. H.; Hasan, Z. W.; Prudowsky, Z. D.; Rudisill, S. E.; Degtyareva, N. N.; Petty, J. T., DNA Templates for Fluorescent Silver Clusters and I-Motif Folding. *The Journal of Physical Chemistry C* **2009,** *113* (45), 19518-19524.

71. Huard, D. J. E.; Demissie, A.; Kim, D.; Lewis, D.; Dickson, R. M.; Petty, J. T.; Lieberman, R. L., Atomic Structure of a Fluorescent Ag8 Cluster Templated by a Multistranded DNA Scaffold. *Journal of the American Chemical Society* **2019,** *141* (29), 11465-11470.
72. Cerretani, C.; Kanazawa, H.; Vosch, T.; Kondo, J., Crystal structure of a NIR-Emitting DNA-Stabilized Ag 16 Nanocluster. *Angewandte Chemie* **2019,** *131* (48), 17313-17317.
73. Lippert, B., Alterations of nucleobase pK (a) values upon metal coordination: origins and consequences. *Prog. Inorg. Chem* **2005,** *54*, 385-447.
74. Joshi, N.; Ngwenya, B. T.; Butler, I. B.; French, C. E., Use of bioreporters and deletion mutants reveals ionic silver and ROS to be equally important in silver nanotoxicity. *Journal of Hazardous Materials* **2015,** *287*, 51-58.
75. Prateeksha; Singh, B. R.; Gupta, V. K.; Deeba, F.; Bajpai, R.; Pandey, V.; Naqvi, A. H.; Upreti, D. K.; Gathergood, N.; Jiang, Y.; El Enshasy, H. A.; Sholkamy, E. N.; Mostafa, A. A.; Hesham, A. E.-L.; Singh, B. N., Non-Toxic and Ultra-Small Biosilver Nanoclusters Trigger Apoptotic Cell Death in Fluconazole-Resistant Candida albicans via Ras Signaling. *Biomolecules* **2019,** *9* (2), 47.
76. Tao, Y.; Aparicio, T.; Li, M.; Leong, K. W.; Zha, S.; Gautier, J., Inhibition of DNA replication initiation by silver nanoclusters. *Nucleic Acids Research* **2021,** *49* (9), 5074-5083.
77. Yang, M.; Chen, X.; Zhu, L.; Lin, S.; Li, C.; Li, X.; Huang, K.; Xu, W., Aptamer-Functionalized DNA–Silver Nanocluster Nanofilm for Visual Detection and Elimination of Bacteria. *ACS Applied Materials & Interfaces* **2021,** *13* (32), 38647-38655.
78. Sengupta, B.; Adhikari, P.; Mallet, E.; Havner, R.; Pradhan, P., Spectroscopic Study on Pseudomonas Aeruginosa Biofilm in the Presence of the Aptamer-DNA Scaffolded Silver Nanoclusters. *Molecules* **2020,** *25* (16), 3631.
79. Zheng, K.; Setyawati, M. I.; Lim, T.-P.; Leong, D. T.; Xie, J., Antimicrobial Cluster Bombs: Silver Nanoclusters Packed with Daptomycin. *ACS Nano* **2016,** *10* (8), 7934-7942.
80. Liu, S.; Yan, Q.; Cao, S.; Wang, L.; Luo, S.-H.; Lv, M., Inhibition of Bacteria In Vitro and In Vivo by Self-Assembled DNA-Silver Nanocluster Structures. *ACS Applied Materials & Interfaces* **2022,** *14* (37), 41809-41818.
81. Karimova, N. V.; Aikens, C. M., Time-Dependent Density Functional Theory Investigation of the Electronic Structure and Chiroptical Properties of Curved and Helical Silver Nanowires. *J Phys Chem A* **2015,** *119* (29), 8163-73.
82. Reveguk, Z. V.; Pomogaev, V. A.; Kapitonova, M. A.; Buglak, A. A.; Kononov, A. I., Structure and Formation of Luminescent Centers in Light-Up Ag Cluster-Based DNA Probes. *The Journal of Physical Chemistry C* **2021,** *125* (6), 3542-3552.
83. Lee, S. P.; Johnson, S. N.; Ellington, T. L.; Mirsaleh-Kohan, N.; Tschumper, G. S., Energetics and Vibrational Signatures of Nucleobase Argyrophilic Interactions. *ACS Omega* **2018,** *3* (10), 12936-12943.
84. Swasey, S. M.; Leal, L. E.; Lopez-Acevedo, O.; Pavlovich, J.; Gwinn, E. G., Silver (I) as DNA glue: Ag+-mediated guanine pairing revealed by removing Watson-Crick constraints. *Scientific Reports* **2015,** *5* (1), 10163.
85. Srivastava, R., Complexes of DNA bases and Watson-Crick base pairs interaction with neutral silver Ag(n) (n = 8, 10, 12) clusters: a DFT and TDDFT study. *J Biomol Struct Dyn* **2018,** *36* (4), 1050-1062.
86. Dale, B. B.; Senanayake, R. D.; Aikens, C. M., Research Update: Density functional theory investigation of the interactions of silver nanoclusters with guanine. *APL Materials* **2017,** *5*, 053102.
87. Espinosa Leal, L. A.; Karpenko, A.; Swasey, S.; Gwinn, E. G.; Rojas-Cervellera, V.; Rovira, C.; Lopez-Acevedo, O., The Role of Hydrogen Bonds in the Stabilization of Silver-Mediated Cytosine Tetramers. *The Journal of Physical Chemistry Letters* **2015,** *6* (20), 4061-4066.

88. Chen, X.; Karpenko, A.; Lopez-Acevedo, O., Silver-Mediated Double Helix: Structural Parameters for a Robust DNA Building Block. *ACS Omega* **2017,** *2* (10), 7343-7348.
89. Chen, X.; Makkonen, E.; Golze, D.; Lopez-Acevedo, O., Silver-Stabilized Guanine Duplex: Structural and Optical Properties. *The Journal of Physical Chemistry Letters* **2018,** *9* (16), 4789-4794.
90. Ramazanov, R. R.; Kononov, A. I., Excitation Spectra Argue for Threadlike Shape of DNA-Stabilized Silver Fluorescent Clusters. *The Journal of Physical Chemistry C* **2013,** *117* (36), 18681-18687.
91. Ramazanov, R. R.; Sych, T. S.; Reveguk, Z. V.; Maksimov, D. A.; Vdovichev, A. A.; Kononov, A. I., Ag–DNA Emitter: Metal Nanorod or Supramolecular Complex? *The Journal of Physical Chemistry Letters* **2016,** *7* (18), 3560-3566.
92. Lisinetskaya, P. G.; Mitric, R., Collective Response in DNA-Stabilized Silver Cluster Assemblies from First-Principles Simulations. *J Phys Chem Lett* **2019,** *10* (24), 7884-7889.
93. Chen, X.; Boero, M.; Lopez-Acevedo, O., Atomic structure and origin of chirality of DNA-stabilized silver clusters. *Physical Review Materials* **2020,** *4* (6), 065601.
94. Yourston, L. E.; Krasnoslobodtsev, A. V., Micro RNA Sensing with Green Emitting Silver Nanoclusters. *Molecules* **2020,** *25* (13).
95. Tao, G.; Chen, Y.; Lin, R.; Zhou, J.; Pei, X.; Liu, F.; Li, N., How G-quadruplex topology and loop sequences affect optical properties of DNA-templated silver nanoclusters. *Nano Research* **2018,** *11* (4), 2237-2247.
96. Hsu, H.-C.; Lin, Y.-X.; Chang, C.-W., The optical properties of the silver clusters and their applications in the conformational studies of human telomeric DNA. *Dyes and Pigments* **2017,** *146*, 420-424.
97. Schultz, D.; Gardner, K.; Oemrawsingh, S. S.; Markesevic, N.; Olsson, K.; Debord, M.; Bouwmeester, D.; Gwinn, E., Evidence for rod-shaped DNA-stabilized silver nanocluster emitters. *Adv Mater* **2013,** *25* (20), 2797-803.
98. Berdakin, M.; Taccone, M.; Julian, K. J.; Pino, G.; Sánchez, C. G., Disentangling the Photophysics of DNA-Stabilized Silver Nanocluster Emitters. *The Journal of Physical Chemistry C* **2016,** *120* (42), 24409-24416.
99. Guo, W.; Yuan, J.; Wang, E., Oligonucleotide-stabilized Ag nanoclusters as novel fluorescence probes for the highly selective and sensitive detection of the Hg2+ ion. *Chem Commun (Camb)* **2009,** (23), 3395-7.
100. Yeh, H. C.; Sharma, J.; Han, J. J.; Martinez, J. S.; Werner, J. H., A DNA--silver nanocluster probe that fluoresces upon hybridization. *Nano Lett* **2010,** *10* (8), 3106-10.
101. Petty, J. T.; Sengupta, B.; Story, S. P.; Degtyareva, N. N., DNA sensing by amplifying the number of near-infrared emitting, oligonucleotide-encapsulated silver clusters. *Anal Chem* **2011,** *83* (15), 5957-64.
102. Liu, H.; Shen, F.; Haruehanroengra, P.; Yao, Q.; Cheng, Y.; Chen, Y.; Yang, C.; Zhang, J.; Wu, B.; Luo, Q.; Cui, R.; Li, J.; Ma, J.; Sheng, J.; Gan, J., A DNA Structure Containing Ag(I) -Mediated G:G and C:C Base Pairs. *Angew Chem Int Ed Engl* **2017,** *56* (32), 9430-9434.
103. Kondo, J.; Tada, Y.; Dairaku, T.; Hattori, Y.; Saneyoshi, H.; Ono, A.; Tanaka, Y., A metallo-DNA nanowire with uninterrupted one-dimensional silver array. *Nat Chem* **2017,** *9* (10), 956-960.
104. Xu, Z.; Xu, L.; Liz-Marzán, L. M.; Ma, W.; Kotov, N. A.; Wang, L.; Kuang, H.; Xu, C., Sensitive Detection of Silver Ions Based on Chiroplasmonic Assemblies of Nanoparticles. *Advanced Optical Materials* **2013,** *1* (9), 626-630.
105. Toomey, E.; Xu, J.; Vecchioni, S.; Rothschild, L.; Wind, S.; Fernandes, G. E., Comparison of Canonical versus Silver(I)-Mediated Base-Pairing on Single Molecule Conductance in Polycytosine dsDNA. *The Journal of Physical Chemistry C* **2016,** *120* (14), 7804-7809.

106. Peng, S.; McMahon, J. M.; Schatz, G. C.; Gray, S. K.; Sun, Y., Reversing the size-dependence of surface plasmon resonances. *Proceedings of the National Academy of Sciences* **2010,** *107* (33), 14530-14534.
107. Thompson, D. G.; Stokes, R. J.; Martin, R. W.; Lundahl, P. J.; Faulds, K.; Graham, D., Synthesis of Unique Nanostructures with Novel Optical Properties Using Oligonucleotide Mixed-Metal Nanoparticle Conjugates. *Small* **2008,** *4* (8), 1054-1057.
108. Rodger, A., UV Absorbance Spectroscopy of Biological Macromolecules. In *Encyclopedia of Biophysics*, Roberts, G. C. K., Ed. Springer Berlin Heidelberg: Berlin, Heidelberg, 2013; pp 2714-2718.
109. Rich, A.; Kasha, M., THE n → π* TRANSITION IN NUCLEIC ACIDS AND POLYNUCLEOTIDES. *Journal of the American Chemical Society* **1960,** *82* (23), 6197-6199.
110. O'Neill, P. R.; Gwinn, E. G.; Fygenson, D. K., UV Excitation of DNA Stabilized Ag Cluster Fluorescence via the DNA Bases. *The Journal of Physical Chemistry C* **2011,** *115* (49), 24061-24066.
111. Soto-Verdugo, V.; Metiu, H.; Gwinn, E., The properties of small Ag clusters bound to DNA bases. *The Journal of Chemical Physics* **2010,** *132* (19), 195102.
112. Brown, S. L.; Hobbie, E. K.; Tretiak, S.; Kilin, D. S., First-Principles Study of Fluorescence in Silver Nanoclusters. *The Journal of Physical Chemistry C* **2017,** *121* (43), 23875-23885.
113. Copp, S. M.; Schultz, D.; Swasey, S.; Pavlovich, J.; Debord, M.; Chiu, A.; Olsson, K.; Gwinn, E., Magic Numbers in DNA-Stabilized Fluorescent Silver Clusters Lead to Magic Colors. *The Journal of Physical Chemistry Letters* **2014,** *5* (6), 959-963.
114. Teo, B. K.; Yang, S.-Y., Jelliumatic shell model. *Journal of Cluster Science* **2015,** *26* (6), 1923-1941.
115. Yoon, B.; Koskinen, P.; Huber, B.; Kostko, O.; Von Issendorff, B.; Häkkinen, H.; Moseler, M.; Landman, U., Size-Dependent Structural Evolution and Chemical Reactivity of Gold Clusters. *ChemPhysChem* **2007,** *8* (1), 157-161.
116. Liu, C.; Li, T.; Abroshan, H.; Li, Z.; Zhang, C.; Kim, H. J.; Li, G.; Jin, R., Chiral Ag23 nanocluster with open shell electronic structure and helical face-centered cubic framework. *Nature Communications* **2018,** *9* (1).
117. Schultz, D.; Gardner, K.; Oemrawsingh, S. S. R.; Markešević, N.; Olsson, K.; Debord, M.; Bouwmeester, D.; Gwinn, E., Evidence for Rod-Shaped DNA-Stabilized Silver Nanocluster Emitters. *Advanced Materials* **2013,** *25* (20), 2797-2803.
118. De Heer, W. A., The physics of simple metal clusters: experimental aspects and simple models. *Reviews of Modern Physics* **1993,** *65* (3), 611-676.
119. Chrimes, A. F.; Khoshmanesh, K.; Stoddart, P. R.; Kayani, A. A.; Mitchell, A.; Daima, H.; Bansal, V.; Kalantar-Zadeh, K., Active Control of Silver Nanoparticles Spacing Using Dielectrophoresis for Surface-Enhanced Raman Scattering. *Analytical Chemistry* **2012,** *84* (9), 4029-4035.
120. Jiang, H.; Chen, Z.; Cao, H.; Huang, Y., Peroxidase-like activity of chitosan stabilized silver nanoparticles for visual and colorimetric detection of glucose. *Analyst* **2012,** *137* (23), 5560-5564.
121. Han, C.; Li, H., Visual detection of melamine in infant formula at 0.1 ppm level based on silver nanoparticles. *Analyst* **2010,** *135* (3), 583-588.
122. Ma, Y.; Niu, H.; Zhang, X.; Cai, Y., One-step synthesis of silver/dopamine nanoparticles and visual detection of melamine in raw milk. *The Analyst* **2011,** *136* (20), 4192.
123. Li, H.; Li, F.; Han, C.; Cui, Z.; Xie, G.; Zhang, A., Highly sensitive and selective tryptophan colorimetric sensor based on 4,4-bipyridine-functionalized silver nanoparticles. *Sensors and Actuators B: Chemical* **2010,** *145* (1), 194-199.
124. Loiseau, A.; Asila, V.; Boitel-Aullen, G.; Lam, M.; Salmain, M.; Boujday, S., Silver-Based Plasmonic Nanoparticles for and Their Use in Biosensing. *Biosensors* **2019,** *9* (2), 78.

125. Xia, Y.; Ye, J.; Tan, K.; Wang, J.; Yang, G., Colorimetric Visualization of Glucose at the Submicromole Level in Serum by a Homogenous Silver Nanoprism–Glucose Oxidase System. *Analytical Chemistry* **2013,** *85* (13), 6241-6247.
126. Malicka, J.; Gryczynski, I.; Lakowicz, J. R., DNA hybridization assays using metal-enhanced fluorescence. *Biochemical and Biophysical Research Communications* **2003,** *306* (1), 213-218.
127. Zhang, J.; Malicka, J.; Gryczynski, I.; Lakowicz, J. R., Oligonucleotide-displaced organic monolayer-protected silver nanoparticles and enhanced luminescence of their salted aggregates. *Anal. Biochem.* **2004,** *330* (1), 81-86.
128. Endo, T.; Ikeda, R.; Yanagida, Y.; Hatsuzawa, T., Stimuli-responsive hydrogel–silver nanoparticles composite for development of localized surface plasmon resonance-based optical biosensor. *Anal. Chim. Acta* **2008,** *611* (2), 205-211.
129. Xiong, D.; Li, H., Colorimetric detection of pesticides based on calixarene modified silver nanoparticles in water. *Nanotechnology* **2008,** *19* (46), 465502.
130. Aslan, K.; Lakowicz, J. R.; Szmacinski, H.; Geddes, C. D., Metal-Enhanced Fluorescence Solution-Based Sensing Platform. *Journal of Fluorescence* **2004,** *14* (6), 677-679.
131. Fredrick, D.; Yourston, L.; Krasnoslobodtsev, A. V., Detection of cancer-associated miRNA using fluorescence switch of AgNC@NA and guanine-rich overhang sequences. *Luminescence* **2023**.
132. He, J.-Y.; Deng, H.-L.; Shang, X.; Yang, C.-L.; Zuo, S.-Y.; Yuan, R.; Liu, H.-Y.; Xu, W.-J., Modulating the Fluorescence of Silver Nanoclusters Wrapped in DNA Hairpin Loops via Confined Strand Displacement and Transient Concatenate Ligation for Amplifiable Biosensing. *Analytical Chemistry* **2022,** *94* (22), 8041-8049.
133. Chen, J.; Wang, M.; Zhou, C.; Zhang, J.; Su, X., Label-free and dual-mode biosensor for HPV DNA based on DNA/silver nanoclusters and G-quadruplex/hemin DNAzyme. *Talanta* **2022,** *247*, 123554.
134. Wong, Z. W.; Muthoosamy, K.; Mohamed, N. A. H.; New, S. Y., A ratiometric fluorescent biosensor based on magnetic-assisted hybridization chain reaction and DNA-templated silver nanoclusters for sensitive microRNA detection. *Biosensors and Bioelectronics: X* **2022,** *12*, 100244.
135. Ma, L.; Wang, J.; Li, Y.; Liao, D.; Zhang, W.; Han, X.; Man, S., A ratiometric fluorescent biosensing platform for ultrasensitive detection of Salmonella typhimurium via CRISPR/Cas12a and silver nanoclusters. *Journal of Hazardous Materials* **2023,** *443*, 130234.
136. Shamsipur, M.; Molaei, K.; Molaabasi, F.; Hosseinkhani, S.; Taherpour, A.; Sarparast, M.; Moosavifard, S. E.; Barati, A., Aptamer-based fluorescent biosensing of adenosine triphosphate and cytochrome c via aggregation-induced emission enhancement on novel label-free DNA-capped silver nanoclusters/graphene oxide nanohybrids. *ACS applied materials & interfaces* **2019,** *11* (49), 46077-46089.
137. Wang, J.; Guo, X.; Liu, R.; Guo, J.; Zhang, Y.; Zhang, W.; Sang, S., Detection of carcinoembryonic antigen using a magnetoelastic nano-biosensor amplified with DNA-templated silver nanoclusters. *Nanotechnology* **2019,** *31* (1), 015501.
138. Xu, J.; Zhu, X.; Zhou, X.; Khusbu, F. Y.; Ma, C., Recent advances in the bioanalytical and biomedical applications of DNA-templated silver nanoclusters. *TrAC Trends in Analytical Chemistry* **2020,** *124*, 115786.
139. Yuan, Y.; Ding, L.; Chen, Y.; Chen, G.; Zhao, T.; Yu, Y., Nano-silver functionalized polysaccharides as a platform for wound dressings: A review. *International Journal of Biological Macromolecules* **2022,** *194*, 644-653.

CHAPTER 3: DNA-TEMPLATED FLUORESCENT SILVER NANOCLUSTERS INHIBIT BACTERIAL GROWTH WHILE BEING NON-TOXIC TO MAMMALIAN CELLS

1. Introduction

The formation of silver nanoclusters (AgNCs) on single-stranded (ss) DNA templates has been shown to promote the unique optical properties defined by the sequences of the DNA strands.[1-3] Out of all available coordination sites on nucleobases, silver cations demonstrate the highest affinity for the N3 of cytosines, and therefore cytosine-rich ssDNAs become efficient capping-agents for AgNC formation.[4-6] The size and shape of AgNCs are regulated by rationally designed and chemically synthesized short DNA oligonucleotides with different numbers of single-stranded cytosines embedded in secondary and tertiary DNA structures such as hairpin loops, i-motifs, and G-quadruplexes, to name a few.[3-6] The optical properties of DNA-AgNCs are dictated by their size, as the appearance of the characteristic fluorescence is possible for nanoclusters comprised of only a few silver atoms. At this nanometer size, a continuous density of electronic energy states present in bulk silver breaks up and a band gap in the material becomes apparent.[1-8] This, in turn, causes a molecule-like behavior of AgNCs with discrete energy states allowing for size-dependent fluorescence to occur.[7-9] DNA-capped AgNCs are also generally more resistant to photobleaching when compared to traditional organic fluorophores or fluorescent proteins, and this property begets the application of DNA-AgNCs in a variety of nanophotonics and biosensing/biomedical applications.[10-13] While nanophotonics and biosensing with DNA-AgNCs' advantageous optical properties have been widely probed and studied, other practical uses of AgNCs remain unexplored. Since the main functional component of DNA-AgNCs is silver, applications based on effects known for this element may prove useful. Various forms of silver, including ions and silver nanoparticles, are well-documented to have antibacterial efficacy.[14-17] Several groups have shown DNA-AgNCs to be effective against both Gram-negative and Gram-positive bacteria in liquid cultures[18-20] and against the formation of

biofilms when aptamers for increased targeting and binding of the bacteria of interest were introduced.[21, 22] However, the underlying mechanisms and relationship between the fluorescent properties of DNA-AgNCs and their antibacterial actions are still understudied and poorly understood. AgNCs offer a large surface-to-volume ratio and are composed of both forms of silver: cationic (Ag^{+}) and neutral (Ag^{0}), thereby providing further advantages over solid silver, silver salts, or silver nanoparticles.

We reason that understanding and linking optical and antibacterial properties of DNA-AgNCs may pave the way to the development of next generation antibacterial agents with high potency and regulated activity. Our current work includes four representative DNA hairpins that template the formation of DNA-AgNCs with four distinct colors and investigates their optical properties in relation to antibacterial activity measured at different pH, as well as in relation to cytotoxicity assessed for several human cell lines. The use of antibacterial DNA-AgNCs formed on DNA hairpins becomes advantageous for various antibacterial formulations and opens broader possibilities for DNA nanotechnology due to the relative structural stability of the hairpins and their inability to participate in any undesirable base-pairings, thus not interfering with any other DNA nanodesigns. As proof-of-concept work, we explore the use of DNA-AgNC forming hairpins with odd numbers of consecutive cytosines (C7, C9, C11, or C13) in their loop compositions.

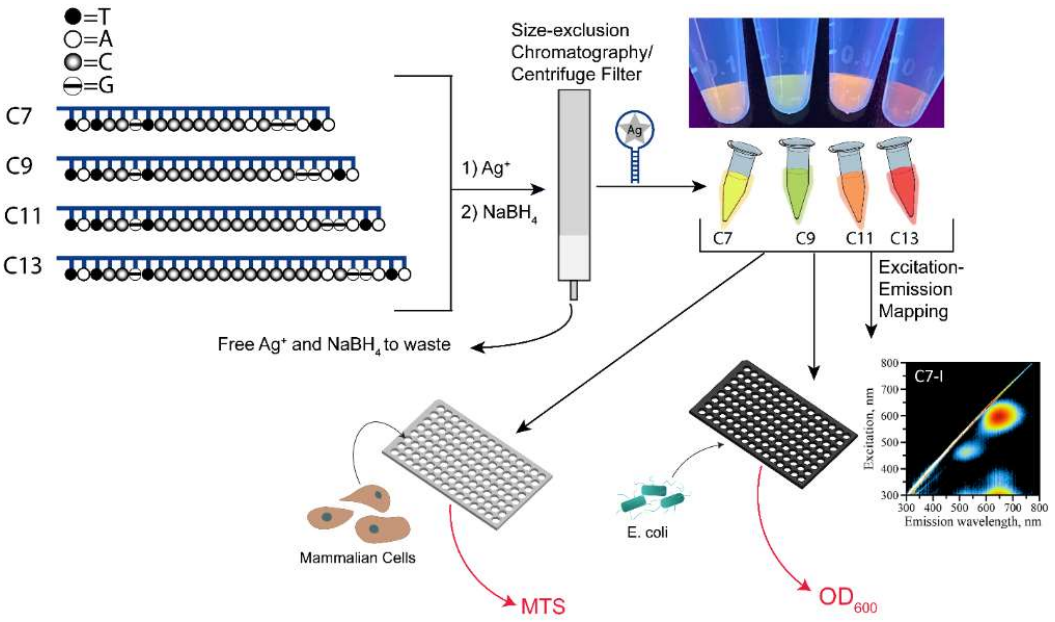

Figure 1. Experimental flow of DNA-AgNC synthesis, purification, and analysis. The embedded image shows DNA-AgNCs after their purification upon UV excitation on a transilluminator.

2. Results

2.1. Template Design

Cytosine-rich ssDNAs are suitable capping agents for templating stable DNA-AgNCs due to cytosine's high affinity for silver ions, Ag^+. Various sequences have been reported to stabilize clusters with unique optical properties, including bright emission bands in the visible part of the spectrum and excitation bands in the UV and visible regions. The emission wavelengths can be modulated by choosing a specific DNA sequence and various colors (e.g., yellow, green, orange, red as shown in **Figure 1**) of DNA-AgNCs have been reported based on prevalent emission wavelengths for a particular nanocluster. While the parameters that define emissive properties of DNA-AgNCs are still not well understood, it is generally accepted that shape, size, and overall charge state of the AgNC are among the main contributors. We hypothesize that the same factors are responsible for modulating the antibacterial activity of the DNA-AgNCs. While cytosine-rich ssDNAs have been widely used in synthesizing AgNCs, these sequences are prone to forming

alternative DNA structures.[23] Such alternative structures include i-motif and non-canonical C-Ag-C base paring facilitated by the presence of silver cations. We have compared properties of two C12-containing templates in which one is an opened ssDNA and another is a sequence embedded in a hairpin loop. The results (**Supporting Figure S1**) clearly show the differences observed for these two sequences after DNA-AgNC formation. As evident from AFM images (**Supporting Figure S1A-B**), the single-stranded template shows various degrees of polymerization, while the hairpin-loop template does not polymerize, forming individual DNA-AgNCs. These results agree well with our recent study demonstrating that the formation of alternative DNA structures in the presence of Ag^+ drives the polymerization of various sequences containing single-stranded (ss) C-rich stretches.[23] Additionally, such polymerization also alters fluorescence properties of AgNCs (**Supporting Figure S1C-D**). Hairpin-looped structures feature one single fluorescence peak for C_{12} sequence while single-stranded templates show multiple peaks, suggesting the formation of AgNCs with various sizes and shapes due to variety of the polymerized templates.[23] To avoid structural and functional uncertainties associated with ssC_N template sequences and to make the structures suitable for further implementation in nanodesign, we have chosen to work only with DNA hairpin templates wherein the C_N sequence forms the loop of the hairpin structure. Four representative templates were constructed with the same double-stranded stem and a loop with a variable number of ssCs (C7, C9, C11, and C13). This design gradually increases the number of binding sites for silver and makes the size of the loop larger (**Figure 1**).[3, 24] An odd number of cytosines in the loop with +2C steps was intended to noticeably alter properties of the DNA-AgNCs with fluorescent colors covering the entire visible spectral region (**Figure 1**). We reasoned that such substantial optical differences would provide an insight into which factors modulate the antibacterial activity of the DNA-AgNCs and how antibacterial activity correlates with the optical signatures of individual DNA-AgNCs. Incubation of the looped DNA templates with silver nitrate and subsequent reduction of silver using sodium borohydride results in the formation of optically active nanoclusters with bright emissions (**Figures**

1 and 2). Figure S8 shows UV-Vis spectra of all four purified AgNC samples immediately after their formation.

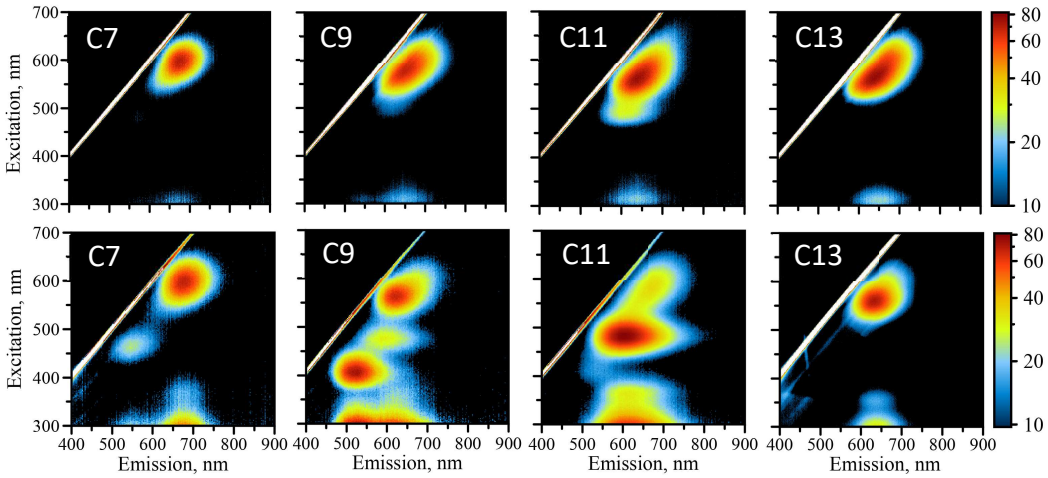

Figure 2. Fluorescence measurements of DNA-AgNCs. Excitation-emission matrix spectroscopy: top panel shows the initial readings of freshly made DNA-AgNCs, bottom panel corresponds to the analysis of samples aged over a period of two weeks (dual fluorescence pattern with both green and red peaks is typical for freshly prepared AgNCs producing distinct colors shown in Figure 1).

2.2. Fluorescence

The formation of DNA-AgNCs is tracked by the changes in solution that are observed after the addition of silver nitrate and sodium borohydride reducing agent and incubation in the dark for 24 hours. We have characterized the optical properties of these DNA-AgNCs using fluorescence excitation-emission matrix spectroscopy (EEM). EEM represents the excitation-emission relationships of the optical response of the DNA-AgNCs presented as 2D contour maps.[25] **Figure 2** shows EEM maps for all four DNA-AgNCs in the 300-800 nm range for the excitation while recording the emission spectrum spanning 300-800 nm wavelengths. Initial readings of the EEMs after purification (top panel of **Figure 2**) indicates that all four samples show a great degree

of similarity in the behavior of emission. All four samples are dominated by one peak in the red part of the spectrum. While similar in general, the peaks show detectable differences.

In **Table 1**, we summarize peak positions for the maximum excitation and maximum emission for all four DNA-AgNCs. It appears that smaller loop DNA-AgNCs have maxima for both excitation and emission shifted to longer wavelengths. It is very pronounced for C7 and C9 with $\lambda_{EXC}/\lambda_{EM}$=600/685 nm and $\lambda_{EXC}/\lambda_{EM}$=580/661 nm, respectively. Further shift to $\lambda_{EXC}/\lambda_{EM}$=562/647 nm and $\lambda_{EXC}/\lambda_{EM}$=562/645 nm is observed for C11 and C13, respectively. C11 DNA-AgNC also features an extra shoulder of emission at shorter excitation wavelengths. C9, C11, and C13 peaks appear to be elongated featuring red edge emission shift (REES) as reported previously and is common for AgNCs.[23, 26, 27] Interestingly, C7 DNA-AgNC does not have REES-based elongation of the emission peak which is well-pronounced for other samples. These observations emphasize the differences of DNA-AgNCs formed by the four looped templates despite all samples having “red” emission.

Table 1. Spectral position of excitation and emission for “red” emitting peak in initial EEMs.

Wavelength, nm.	**C7**	**C9**	**C11**	**C13**
EXC_{MAX}	600	580	562	562
FLU_{MAX}	685	661	647	645

The differences in observed optical properties intensify further as samples are allowed to age. Changes in emission pattern with time develop very quickly during “maturation” stage of the AgNCs typical for our preparation procedure. These changes represent the conversion of AgNCs’ from “red” to “green” emission upon interaction with ambient conditions as we have previously reported.[26] ”Red” to “green” conversion can be linked to the interactions of AgNCs with species

dissolved in the solution that are capable of oxidizing silver atoms ($Ag^0 \rightarrow Ag^+$), such as molecular oxygen.[26] Many reports documented the “blue” shift with aging and some protocols call for bubbling oxygen through to stimulate this transition.[28] All four of our samples also experience such “blue” shift and eventually develop a pattern of multi-peaked emission with some samples more noticeable than others (for example, C9 vs C13). **Figure 2** summarizes in detail all changes in emission patterns when C7-C13 DNA-AgNCs age over a period of two weeks. The appearance of additional emission peaks in the “green” region are obvious for C7, C9, and C11, while C13 remained primarily as a single peak. The changes in C13 DNA-AgNCs include the loss of elongated shape with the near-IR part of the peak disappearing over time. Shorter loops C7, C9, and C11 develop an obvious multipeak excitation-emission pattern over time. These new peaks appear in the “orange” and “green” spectral region. Also, these peaks differ significantly in their position and intensity. C7 DNA-AgNCs have only one new peak of $\lambda_{EXC}/\lambda_{EM}$=465/547 nm – “green.” The intensity of this new peak is 27% the intensity of the original “red” peak. Both C9 and C11 have multi-peak patterns of newly appeared “orange” and “green” emission labeled O (longer wavelengths) and G (shorter wavelengths). The positions of these two new peaks are very similar for both C9 and C11 DNA-AgNCs: $\lambda_{EXC}/\lambda_{EM}$=475/606 nm (O-C9), $\lambda_{EXC}/\lambda_{EM}$=480/606 nm (O-C11), $\lambda_{EXC}/\lambda_{EM}$=408/530 nm (G-C9), and $\lambda_{EXC}/\lambda_{EM}$=410/536 nm (G-C11). Similar spectral positions indicate the same nature of “green” states for both C9 and C11 DNA-AgNCs. The differences for these two samples, however, include the position of the “red” peak as listed in **Table 1**. Another major difference is the relative intensities of orange and green peaks, O and G. O peak dominates in the C11 sample, while G is more pronounced in the C9 sample. The following are the relative intensities as compared to the original “red” peak: 22% (O-C9), 360% (O-C11), 112% (G-C9), and 29% (G-C11). The observed intensities suggest that C9 DNA-AgNCs primarily stabilize G state while C11 DNA-AgNCs prefer O. The O peak is not observed in the fluorescence of the aged C7 sample, while C13 remains “red” during aging.

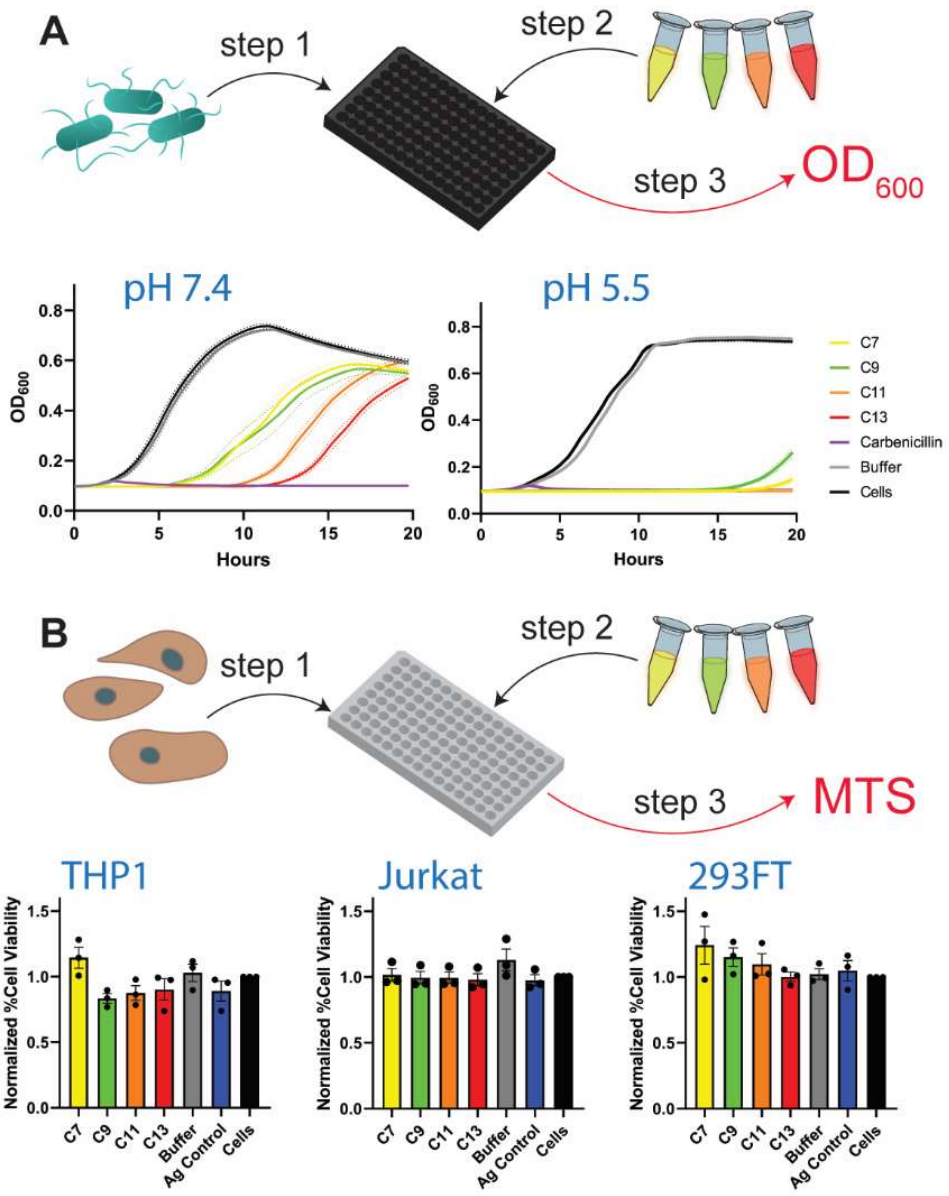

Figure 3. Biological activity of DNA-AgNCs. (**A**) The growth curves of *E. coli* when treated with 4 μM DNA-AgNC are shown at pH 7.4 (the pH of standard LB) and pH 5.5. The standard error of the mean of each measurement is shown as a dotted line on both sides of the solid line in the same color. The lines for C11, C13, and Carbenicillin overlap at pH 5.5. (**B**) The normalized cell viability of THP1-Dual™, Jurkat, and 293FT cells after incubation with 4 μM AgNC for 20 hours, as assessed by MTS assay.

To complete the description of the emissive properties of C7-C13 DNA-AgNCs, we also visualized the emission of nanoclusters under UV excitation on a trans-illuminator (at 254 nm). Such excitation is typically discussed as a means of excitation via DNA bases that contact silver atoms in the nanocluster. 254 nm excitation results in a color palette of the employed samples (colors under trans-illuminator excitation, **Figure 1** - top). This picture reflects the rich emission pattern observed for C7-C13 samples in the visible part of the spectrum.

2.3. Cell culture experiments

To assess the relative effects of representative DNA-AgNCs on bacterial cells, TOP10F' *E. coli* are grown in liquid cultures and treated with the panel of DNA-AgNCs at a final concentration of 4 μM DNA (**Figure 3A**). A decrease in the bacterial growth is observed over a 20-hour period for all *E. coli* cultures treated with DNA-AgNCs when compared to the non-treated control. There is a strong dose-dependence noted for all DNA-AgNCs (**Supporting Figure S2**) with 4 μM to be the lowest DNA concentration that shows reasonable antibacterial effectiveness for all constructs. As such, all experiments are carried out at 4 μM in order to best resolve differences between four tested DNA-AgNCs. To quantitatively examine the inhibition of *E. coli* growth, we compare the changes in the amount of time ($\Delta t_{1/2}$) required for bacteria cultured with each DNA-AgNC to grow to half of their maximum optical density when referenced to untreated cells from the same experimental group. C13 was the most effective DNA-AgNC at slowing bacterial growth as the calculated $\Delta t_{1/2}$ for C7, C9, C11, and C13, shown with their 95% confidence intervals, are 5.5 ± 0.2 hours, 5.8 ± 0.3 hours, 8.8 ± 0.2 hours, and 10.7 ± 0.2 hours respectively. The effect of free silver at the concentrations used to synthesize the DNA-AgNCs can be considered minimal since the control experiment with 650 μM of Ag^+, the highest of the concentrations used for C_N synthesis, has a minimal effect on the growth curve after being reduced with $NaBH_4$ (**Supporting Figure S3**). The antibacterial effect of the DNA-AgNCs greatly increases at lower pH. When *E. coli* grown in pH 5.5-buffered LB are treated with 4 μM of each DNA-AgNC, the growth is nearly fully inhibited

over the entire 20 hours (**Figure 3A**). From these experiments, the performance of C7 and C9 as antibacterial agents are similar, though it is clear that C13 outperforms C11 significantly. From these data, it appears that there may be a correlation between the number of cytosines and the antibacterial efficacy of the DNA-AgNC for larger hairpins.

To test the same conditions in mammalian cells, we use several human cell lines and all DNA-AgNCs are again introduced at a 4 μM final concentration. The cell viability is assessed after 20 hours of incubation using an MTS assay (**Figure 3B**). No statistically significant reduction in cell viability is observed after incubation with DNA-AgNCs for Jurkat, THP1, or 293FT cells. To ensure the safety of DNA-AgNCs for mammalian cells, the same experiments are repeated at a final concentration of 8 μM DNA-AgNC with all three cell lines and the results are similar (**Supporting Figure S4**). Therefore, AgNCs remain non-toxic to mammalian cells at concentrations two-fold higher than required to efficiently inhibit bacterial growth.

2.4. Stoichiometry Determination

In order to quantify the number of silver atoms bound to each ssDNA oligonucleotide, EDS is performed and micrographs of dried AgNC solutions are recorded using SEM. The ratio of the relative atomic percentages of the Ag and P in the EDS spectrum are used for evaluating the stoichiometric ratio of silver per hairpin-loop DNA template. From these experiments, we determine that each C7 DNA-AgNC binds an average of 9.9 ± 0.6 silver atoms (± SEM), C9 DNA-AgNC binds an average of 8.5 ± 0.5 silver atoms, C11 DNA-AgNC binds an average of 11.7 ± 0.5 silver atoms, and C13 DNA-AgNC binds an average of 10.2 ± 0.9 silver atoms. The differences in the number of silver atoms bound were not found to be statistically significant between each templating strand. A representative micrograph of a DNA-AgNC sample is shown in **Figure 4**, and the micrographs of all samples analyzed by EDS are shown in the supplementary information (**Supporting Figure S5**).

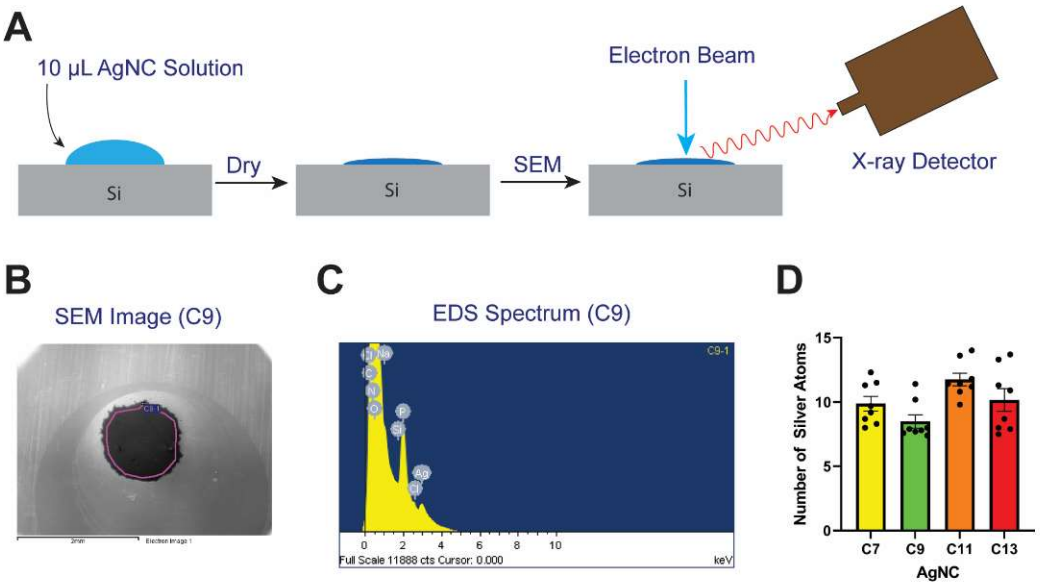

Figure 4. (**A**) The general workflow for the SEM and EDS experiments is shown. The drying is done at ambient conditions with the silicon wafer covered by a petri dish. (**B**) A representative SEM image is shown of a DNA-AgNC C9 sample and (**C**) the raw EDS spectrum of the same sample. The purple line in (**B**) defines the outer perimeter of the area that is scanned to obtain the EDS spectrum. (**D**) The number of bound silver atoms on each templating DNA hairpin is shown as determined by EDS. Error bars are the standard error of the mean for each measurement.

3. Discussion

Silver has long been used as a disinfectant. The most recent applications include the use of silver nanoparticles in many different areas including food packaging, water and air disinfection, the textile sector, and medical applications (Silver Soaker® Catheters, Acticoat™, SilvaSorb® Gel).[29, 30] The search for new therapeutic agents to combat multi-drug resistant (MDR) bacteria is ongoing. While silver nanoparticles have been recently extensively studied for their use as antibacterial agents,[31] novel silver nanoclusters have been largely overlooked[18] primarily because most studies have focused on biosensing applications due to the unique optical

properties of AgNCs.[27, 32, 33] DNA-AgNCs have several advantages which position them as excellent candidates for antibacterial applications. First, DNA-AgNCs are small in size – they are comprised of only a few atoms of silver capped with stabilizing cytosine-rich ssDNA oligonucleotides. Since DNA-AgNCs are bound to DNA, in addition to serving as a host for AgNCs, DNA can also be utilized for embedding AgNCs into a structured network of functional assemblies leading to novel properties and functions of hybrid nanomaterials.[23, 26] In this study, we show that AgNCs are capable of inhibiting bacterial growth at a much lower concentration (4 μM) than carbenicillin (132 μM), which is a bactericidal antibiotic from the penicillin group and was used as a positive control in this study. We confirm, herein, that DNA-AgNCs show very little toxicity against human cells. In addition to serving as a template for AgNC synthesis, DNA templates may further contribute to better solubility and biocompatibility of clusters. Thus, DNA-AgNCs could potentially be used against a broad range of various bacteria without harmful side effects. Furthermore, the robust fluorescence of AgNCs can be coupled with biocompatibility and antibacterial properties to produce label-free bioimaging agents with dual purpose.

Our additional experiments indicate that DNA-AgNCs exhibit antibacterial activity against *Lactobacilli* (**Supporting Figure S6**), suggesting that DNA-AgNCs might cause undesirable effects to the gut microbiota, and should be avoided in applications involving oral ingestion of these materials, *e.g.* in food packaging. This is especially concerning given the apparent increased antibacterial efficacy of AgNCs at a lower pH (**Figure 3A**). Previous work has shown that a lower pH will increase the antibacterial efficacy of silver nanoparticles, likely due to a resulting increased production of reactive oxygen species. DNA templated AgNCs are capable of catalyzing the production of reactive oxygen species.[18, 34] It is possible, though outside of the scope of the current work, that our DNA-AgNCs produce an increased amount of reactive oxygen species as pH decreases. It is unlikely that DNA-AgNCs are leaching silver into solution through protonation events at the lower pH used in this study, as the pK_a of cytosine is close to 4.4;

therefore, less than 10% of cytosines would be expected to protonate.[35] It is also considered improbable that the decreased pH would cause silver ions to further detach from the AgNC as DNA-AgNCs have previously been shown to retain their fluorescence over a wide pH range, down to a pH of 5, implying the stability of the AgNC over the same range.[36]

We show that C13 DNA-AgNC produces the highest antibacterial activity among the four studied sequences followed by C11, while C7 and C9 DNA-AgNCs show lower activity (**Figure 3A**). Several factors might contribute to antibacterial activity, however, the number of silver atoms comprising the AgNCs does not appear to be the decisive factor. Using EDS analysis we confirmed that there is no statistical significance in the number of Ag atoms bound by each DNA-AgNC (**Figure 4A**). It is unlikely that the amount of silver in the DNA-AgNCs determines their antibacterial properties as all templates stabilize clusters of nearly the same size with N≈10-11 bound in them. Our observation is supported by a previous report which also ruled out the amount of silver atoms per cluster.[18] Emission color has been proposed to correlate with DNA-AgNCs' antibacterial properties with "red" emissive clusters being the most active.[18] We also turned to fluorescence properties in search of a possible explanation for the antibacterial activity of DNA-AgNCs. It is unclear how exactly silver DNA-AgNCs act in terms of antibacterial properties and this uncertainty in their mechanism of antibacterial action has triggered the current study. There are clear changes in fluorescent properties of DNA-AgNCs which we can correlate with the increased antibacterial activity of AgNCs. It appears that a single-peak emission pattern might be the key. The mere presence of "red" fluorescence does not define antibacterial properties; all samples are "red" initially, but the abilities to inhibit bacterial growth differ among C13, C11 and C9, C7. C13 remains "red" during aging while C11 effectively converts to "orange." At the same time, C13 provides better antibacterial efficacy as compared to C11. Also, C7 remains primarily "red" while its activity is lower than C11 and C13. C9 is the only sample that develops a "green" peak with high intensity, but it is also less effective at inhibiting bacterial growth. As such, we

hypothesize that the stability of the “red” fluorescence upon aging may be one of the most decisive factors for the antibacterial efficacy of DNA-AgNCs.

It is commonly accepted that DNA-AgNCs include both Ag^0 and Ag^+ atoms in their composition. The ratio of Ag^0/Ag^+ defines the overall charge state and the color of the nanocluster’s emission.[37] It has been proposed that distinct “green” and “red” fluorescence occurs for a “magic number” of neutral silver atoms in the nanocluster.[37, 38] Four neutral atoms produce green fluorescence and six Ag^0 atoms produce red fluorescence regardless of the number of Ag^+.[37] Recent studies indicated that such conversion does not change the overall number of silver, *N*, in the cluster as this conversion is reversible.[26, 31] Given that the number of bound silver atoms remains constant, it is unlikely that it would be easy to separate DNA-AgNCs with different oxidation states from each other for characterization by chromatographic means and it is expected that the physicochemical properties of the DNA-AgNC as a whole will be largely unchanged by changes in the oxidation state of the AgNC itself. “Red,” “orange,” and “green” emissive states of AgNCs we observe may represent different ratios of Ag^+ to Ag^0. Aging of the samples can therefore be explained by the interaction of AgNCs with species dissolved in the solution that are capable of oxidizing silver atoms ($Ag^0 \rightarrow Ag^+$). For example, dissolved “molecular oxygen” might effectively convert “red” to “orange” and to “green” emitting species. Controlled oxidation with hydrogen peroxide confirms our conclusion (**Supporting Figure S8**). The addition of hydrogen peroxide gradually converts emissive patterns which resembles “aging” of all samples. Many studies relate the antibacterial activity of silver nanoparticles to the oxidative release of Ag^+.[39] In this regard, DNA-AgNCs already have silver ions in their composition and can therefore act as antibacterial agents. Furthermore, the ratio of Ag^+/Ag^0 can modulate the antibacterial activity of DNA-AgNCs. It is tempting to suggest that the increased number of silver ions in DNA-AgNCs may explain higher antibacterial activity. However, C9 is dominated by “green” emitting species which would supposedly have the highest number of cations in the DNA-AgNC

composition, while we observe that C9 has the second lowest antibacterial effect. It is possible that the looped hairpin templates used herein while varying in length may have different protective properties for DNA-AgNCs depending on the final conformation of the loop wrapping around silver nanoclusters. For example, faster conversion of C13 to a non-emitting species might indicate lesser protection of the clusters and thus correlate better with higher antibacterial activity of C13. Additional studies will be required to identify whether intact DNA-AgNCs act as the antibacterial agent or if their activity requires nanocluster dissolution with the release of silver ions into the solution.

Another possible explanation for different activities observed for the four analyzed samples is that the nature of emissive and non-emissive states may play a role. We observed that all four samples age and react with hydrogen peroxide very differently (**Supporting Figure S7**). It is also apparent that partial oxidation is involved in “red” to “orange” or “red” to “green” conversion of emissive DNA-AgNC states. We have evaluated the rate of “red” peak conversion as a function of hydrogen peroxide concentration (**Figure 5**) for all four DNA-AgNCs using a modified Stern-Volmer relationship.[40]

$$F_0/_F = (1 + K_D C_{H2O2})(1 + K_S C_{H2O2}) \quad (1)$$

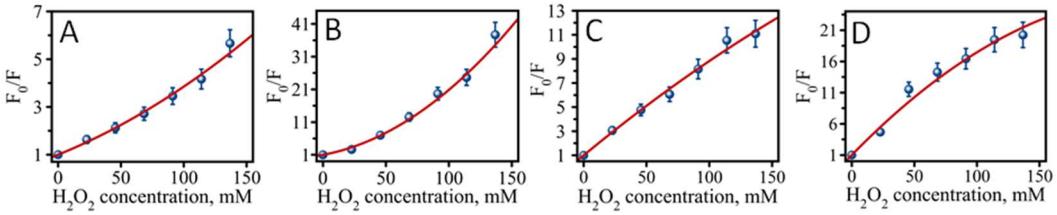

Figure 5. Stern-Volmer plots for (**A**) C7 DNA-AgNCs, (**B**) C9 DNA-AgNCs, (**C**) C11 DNA-AgNCs, (**D**) C13 DNA-AgNCs. Data points were fitted with equation 1 which considers two possible quenching mechanisms: static and dynamic.

Generally, a linear Stern-Volmer plot indicates a single class of fluorophores which are all equally vulnerable to quenching by hydrogen peroxide.[40] All four DNA-AgNC samples show non-linear F_0/F vs H_2O_2 concentration dependence (**Figure 5**). This suggests a complex nature of fluorescence quenching with at least two deactivation pathways: intermolecular quenching due to H_2O_2 (dynamic quenching, K_D, most likely due to intersystem crossing from singlet S* to triplet T*) and intramolecular conversion of “red” to “orange” or “green” (static quenching, K_S, due to change of the overall charge state of AgNC). While C7 and C9 DNA-AgNCs exhibit slightly upward curvature, C11 and C13 show clear downward curvature. This observation indicates that these two groups have different mechanisms of quenching while interacting with hydrogen peroxide. Typically, downward curvature is associated with fluorophores which are inaccessible to the quencher, suggesting a more protective nature of larger loops.[40] Interestingly, C13 also shows the highest antibacterial activity and the largest downward curvature among the studied C-loop templates. While it is difficult to specify exact details of interactions between the “quencher” and certain states of AgNCs without further studies, it is apparent that the charge state of the DNA-AgNC can play a critical role in defining the antibacterial activity of nanoclusters. Several reports have indicated that silver nanoclusters are capable of generating excessive amounts of intracellular reactive oxygen species which is proposed as the major contributing factor defining DNA-AgNCs’ antibacterial ability.[18, 41] It is also becoming increasingly apparent from recent studies both theoretical[42] and experimental[43] that certain shape, composition, and charge states of DNA-AgNCs can increase the chances of optically “dark” states to exist with highspin multiplicity (doublet and triplet). Therefore, it is not unreasonable to propose that highspin AgNC states may interact with highly abundant triplet oxygen removing the "spin-forbidden" condition and stimulating the transition of triplet to singlet oxygen: $^3O_2 \rightarrow {}^1O_2$. Since singlet oxygen is far more reactive compared to triplet oxygen, this can explain various antibacterial properties of different DNA-AgNCs and the generation of reactive oxygen species.

In conclusion, nucleic acid-based nanomaterials are often designed based on two rationales: the delivery of functional moieties which can be implemented into the nanoscaffolds and the patterns in recognition of nucleic acids which contribute to the cellular response. DNA-AgNCs offer an approach by which functional fluorescent moieties can contribute to selective growth inhibition of bacterial cultures. The results of this study suggest that the rich optical behavior of the DNA-AgNCs may be tightly linked to the antibacterial properties of this novel class of nanostructures. Excitation-emission pattern, interconversion of emissive states, and their connection with environmental changes are the keys to understanding the mechanism of DNA-AgNC inhibitive action. The results obtained herein warrant further exploration of the antibacterial effects of DNA-AgNCs on both pathogenic and non-pathogenic bacteria species.

4. Materials and Methods

Synthesis of DNA-AgNCs. All DNA oligonucleotides were purchased from Integrated DNA Technologies (IDT), Inc. (Coralville, IA, USA) as desalted products and used without further purification. All sequences are listed in the Supporting Information. Nuclease-free water was obtained from IDT. Sodium borohydride was purchased from TCI America, Inc. In a typical preparation, DNA template (C13, C11, C9, or C7) and $AgNO_3$ aqueous solutions were mixed and incubated for 25 min at room temperature in ammonium acetate buffer (100 mM NH_4OAc , pH 6.9). Next, $NaBH_4$ aqueous solution was added and samples were placed on ice and stirred vigorously. The final concentrations (C) of the components were as follows: $C_{DNA\text{-}template}$ = 50 μM; C_{AgNO3} was adjusted to match the number of cytosines in the loop according to n*$AgNO_3$:C_n;C_{NaBH4}:C_{AgNO3} was taken at 1:1 ratio and C_{NH4Ac} = 4 mM. The solution was then incubated in the dark for 24 h at 4°C. Synthesized DNA-AgNCs were then purified *via* a NAP-5 (Cytiva) filtration gel column purchased from Sigma-Aldrich, Inc. for fluorescence measurements. Purification was performed according to the protocol supplied by the manufacturer. Final concentrations of DNA-AgNC obtained after filtration varied between 8 – 15 μM and were

evaluated by taking DNA absorption at 265 nm wavelength. For antibacterial and mammalian cell viability experiments, DNA-AgNCs were purified using 3 kDa Amicon centrifugal filters by washing twice with buffer and diluting to 50 μM DNA-AgNC.

Fluorescence measurements. The excitation and emission spectra were acquired on a Duetta – Fluorescence and Absorbance Spectrometer (Horiba, Inc., Chicago, IL, USA). In all the measurements, the concentration of the templating sequence was kept the same at ~6 μM. Fluorescence measurements were carried out in a Sub-Micro Fluorometer Cell, model 16.40F-Q-10 (from StarnaCells, Inc., Atascadero, CA, USA) at room temperature of ~22 °C. The excitation–emission matrix spectra (EEMS) were recorded with 0.5 nm resolution. Fluorescence spectra were recorded with the emission wavelength range from 300 nm to 1000 nm, the initial excitation wavelength was set to 280 nm, and the final excitation wavelength was set to 800 nm with an increment of 0.5 nm. Matrix data were then used for 2D contour plot using MagicPlot Pro software.

Bacterial growth assays. TOP10F' *E. coli* were purchased from ThermoFisher Scientific and grown in Luria broth (LB) purchased from Sigma. Where shown, the pH of LB was adjusted to pH 5.5 with 100 mM 2-morpholin-4-ylethanesulfonic acid (MES). *E. coli* were grown in LB from single colonies while shaking at 200 rpm at 37 °C in a GeneMate Incubated Shaker. For treatment with AgNCs, bacteria were diluted in LB to an optical density at 600 nm (OD_{600}) of 0.018-0.020. Next, 50 μL of diluted bacteria were added to each well of a 96-well flat-bottom black-walled plate. Purified DNA-AgNCs were added with LB to reach a final volume of 100 μL in each well with 4 μM final concentration of DNA-AgNCs. Carbenicillin was used as a positive control at a final concentration of 50 μg/mL (132 μM). The lids of the plates were hydrophobically treated by filling them with 10 mL of 20% ethanol, 0.05% Triton X-100 for 30 seconds.[44] The excess liquid was drained, and the lid was leaned against the back of a fume hood to dry for 30 minutes.[44] The lids were parafilmed to the microwell plates to prevent excess evaporation. Microplate optical density measurements were recorded using a Tecan Spark microwell plate reader. The plates

were shaken for 30 seconds between each measurement and were incubated at 37 °C with OD_{600} measurements taken every 15 minutes over 20 hours. A minimum of six technical repeats and three biological repeats of each experiment were performed. The time required for each growth curve to reach half its maximum optical density, $t_{1/2}$, was calculated with GraphPad Prism 9 using a non-linear fit of the data. The difference between the untreated control $t_{1/2}$ and the treatment $t_{1/2}$ is reported as $\Delta t_{1/2}$. Additional experiments in *Lactobacillus* cultures were conducted to understand the effects of DNA-AgNCs on normal microflora (**Supporting Information**).

Mammalian cell viability assays. For all experiments, cells were maintained and cultured at 37 °C, 5% CO_2. THP1-Dual™ cells were purchased from InvivoGen and were maintained in RPMI 1640, 2 mM L-glutamine, 25 mM HEPES, 10% heat-inactivated fetal bovine serum (FBS), and PenStrep (100 U/mL,100 µg/mL). 293FT cells were cultured in DMEM, 2 mM L-glutamine, 10% FBS, and PenStrep (100 U/mL, 100 µg/mL). Jurkat cells were cultured in RPMI 1640, 2 mM L-glutamine, 25 mM HEPES, 10% FBS, and PenStrep (100 U/mL,100 µg/mL). For cell viability studies, cells were plated in a 96-well flat-bottom plate at a density of 40,000 cells per well along with DNA-AgNC solution at final concentrations of 4 or 8 µM and final well volumes of 100 µL. After incubation with AgNC treatments for 20 hours, 20 µL of CellTiter 96® AQueous One Solution Cell Proliferation Assay (MTS) were added to each well. Plates were incubated for an additional 75 minutes at 37 °C, 5% CO_2. The plates were then read on a Tecan Spark microplate reader for absorbance at 490 nm. Sixteen reads per well were averaged for each value.

Scanning electron microscopy (SEM) and energy-dispersive x-ray spectroscopy (EDS). Solutions of 50 µM C7, C9, C11, and C13 in buffer were pipetted onto a polished silicon wafer as 10 µL droplets. Droplets were allowed to dry in a covered petri dish overnight at room temperature. The solid residue was analyzed with SEM/EDS to determine the atomic ratio between P and Ag. Dried solutions on the Si substrate were analyzed with a JEOL JSM-6480 SEM. Micrographs were taken in secondary electron mode with an accelerating voltage of 5 kV. EDS spectra were

collected using an Oxford Instruments INCA EDS behind a beryllium window. Atomic percentages were calculated by the INCA instrument software from P Kα (2.013 keV) and Ag Lα (2.984 keV) characteristic x-rays.

Statistical analysis. All data is presented as the mean ± standard deviation or standard error of the mean (specified for each case) for a minimum of N=3 independent biological replicates. For statistical analysis, a one-way ANOVA was performed, followed by a t-test using GraphPad Prism 9.0.0 for Windows, GraphPad Software, San Diego, California USA, www.graphpad.com. P-values of $p<0.05$ were considered statistically significant.

Supplementary Materials: The following are available online at www.mdpi.com/xxx/s1, Figure S1-S7 and sequences used in this project.

Author Contributions: Conceptualization by K.A.A. and A.V.K.; methodology, validation, and formal analysis by L.R., L.Y., M.C., D.B., L.D., S.K., N.M., O.S. All authors have read and agreed to the published version of the manuscript.

Funding: Research reported in this publication was supported by the National Institute Of General Medical Sciences of the National Institutes of Health under Award Number R35GM139587 (to K.A.A.). The content is solely the responsibility of the authors and does not necessarily represent the official views of the National Institutes of Health.

Institutional Review Board Statement: Not applicable.

Informed Consent Statement: Not applicable.

Data Availability Statement: All data are available and can be shared upon request.

Acknowledgments: The authors would like to thank Dr. Brittany Johnson (UNCC) for advice with bacterial studies, the Troutman Lab (UNCC) for use of the Molecular Devices SpectraMax M5 microplate reader for initial data collection, and Dr. Ryan Riskowski (UNO) for use of the Duetta

Spectrometer. AFM scans were obtained with the use of MultiMode Nanoscope IV system at the Nanoimaging Core Facility, UNMC, and we also thank Dr. Alexander Lushnikov (NCF-UNMC) for his assistance in sample preparation for AFM imaging.

Conflicts of Interest: The authors declare no conflict of interest.

Sample Availability: Samples of the DNA-AgNCs are available from the authors.

References

1. Ritchie, C. M.; Johnsen, K. R.; Kiser, J. R.; Antoku, Y.; Dickson, R. M.; Petty, J. T., Ag Nanocluster Formation Using a Cytosine Oligonucleotide Template. *The Journal of Physical Chemistry C* **2007,** 111, (1), 175-181.

2. Petty, J. T.; Zheng, J.; Hud, N. V.; Dickson, R. M., DNA-Templated Ag Nanocluster Formation. *J. Am. Chem. Soc.* **2004,** 126, (16), 5207-5212.

3. Chandler, M.; Shevchenko, O.; Vivero-Escoto, J. L.; Striplin, C. D.; Afonin, K. A., DNA-Templated Synthesis of Fluorescent Silver Nanoclusters. *Journal of Chemical Education* **2020,** 97, (7), 1992-1996.

4. New, S. Y.; Lee, S. T.; Su, X. D., DNA-templated silver nanoclusters: structural correlation and fluorescence modulation. *Nanoscale* **2016,** 8, (41), 17729-17746.

5. Cerretani, C.; Kanazawa, H.; Vosch, T.; Kondo, J., Crystal structure of a NIR-Emitting DNA-Stabilized Ag 16 Nanocluster. *Angewandte Chemie* **2019,** 131, (48), 17313-17317.

6. Huard, D. J. E.; Demissie, A.; Kim, D.; Lewis, D.; Dickson, R. M.; Petty, J. T.; Lieberman, R. L., Atomic Structure of a Fluorescent Ag8 Cluster Templated by a Multistranded DNA Scaffold. *Journal of the American Chemical Society* **2019,** 141, (29), 11465-11470.

7. O'Neill, P. R.; Gwinn, E. G.; Fygenson, D. K., UV Excitation of DNA Stabilized Ag Cluster Fluorescence via the DNA Bases. *The Journal of Physical Chemistry C* **2011,** 115, (49), 24061-24066.

8. Lee, T.-H.; Gonzalez, J. I.; Zheng, J.; Dickson, R. M., Single-Molecule Optoelectronics. *Accounts Chem. Res.* **2005,** 38, (7), 534-541.

9. Gwinn, E. G.; O'Neill, P.; Guerrero, A. J.; Bouwmeester, D.; Fygenson, D. K., Sequence-Dependent Fluorescence of DNA-Hosted Silver Nanoclusters. *Adv. Mater.* **2008,** 20, (2), 279-283.

10. Gwinn, E.; Schultz, D.; Copp, S.; Swasey, S., DNA-Protected Silver Clusters for Nanophotonics. *Nanomaterials* **2015,** 5, (1), 180-207.

11. Yin, N.; Yuan, S.; Zhang, M.; Wang, J.; Li, Y.; Peng, Y.; Bai, J.; Ning, B.; Liang, J.; Gao, Z., An aptamer-based fluorometric zearalenone assay using a lighting-up silver nanocluster probe and catalyzed by a hairpin assembly. *Microchimica Acta* **2019,** 186, (12).

12. Afonin, K. A.; Schultz, D.; Jaeger, L.; Gwinn, E.; Shapiro, B. A., Silver Nanoclusters for RNA Nanotechnology: Steps Towards Visualization and Tracking of RNA Nanoparticle Assemblies. Springer New York: 2015; pp 59-66.

13. Afonin, K. A.; Dobrovolskaia, M. A.; Church, G.; Bathe, M., Opportunities, Barriers, and a Strategy for Overcoming Translational Challenges to Therapeutic Nucleic Acid Nanotechnology. *ACS Nano* **2020,** 14, (8), 9221-9227.

14. Feng, Q. L.; Wu, J.; Chen, G. Q.; Cui, F. Z.; Kim, T. N.; Kim, J. O., A mechanistic study of the antibacterial effect of silver ions on Escherichia coli and Staphylococcus aureus. *Journal of Biomedical Materials Research* **2000,** 52, (4), 662-668.

15. Sondi, I.; Salopek-Sondi, B., Silver nanoparticles as antimicrobial agent: a case study on E-coli as a model for Gram-negative bacteria. *J. Colloid Interface Sci.* **2004,** 275, (1), 177-182.

16. Morones, J. R.; Elechiguerra, J. L.; Camacho, A.; Holt, K.; Kouri, J. B.; Ramirez, J. T.; Yacaman, M. J., The bactericidal effect of silver nanoparticles. *Nanotechnology* **2005,** 16, (10), 2346-2353.

17. Banerjee, I.; Pangule, R. C.; Kane, R. S., Antifouling Coatings: Recent Developments in the Design of Surfaces That Prevent Fouling by Proteins, Bacteria, and Marine Organisms. *Adv. Mater.* **2011,** 23, (6), 690-718.

18. Javani, S.; Lorca, R.; Latorre, A.; Flors, C.; Cortajarena, A. L.; Somoza, Á., Antibacterial Activity of DNA-Stabilized Silver Nanoclusters Tuned by Oligonucleotide Sequence. *ACS applied materials & interfaces* **2016,** 8, (16), 10147-10154.

19. Yang, L.; Yao, C.; Li, F.; Dong, Y.; Zhang, Z.; Yang, D., Synthesis of Branched DNA Scaffolded Super-Nanoclusters with Enhanced Antibacterial Performance. *Small* **2018,** 14, (16), 1800185.

20. Eun, H.; Kwon, W. Y.; Kalimuthu, K.; Kim, Y.; Lee, M.; Ahn, J.-O.; Lee, H.; Lee, S. H.; Kim, H. J.; Park, H. G.; Park, K. S., Melamine-promoted formation of bright and stable DNA–silver nanoclusters and their antimicrobial properties. *Journal of Materials Chemistry B* **2019,** 7, (15), 2512-2517.

21. Sengupta, B.; Sinha, S. S.; Garner, B. L.; Arany, I.; Corley, C.; Cobb, K.; Brown, E.; Ray, P. C., Influence of Aptamer-Enclosed Silver Nanocluster on the Prevention of Biofilm by <I>Bacillus thuringiensis</I>. *Nanoscience and Nanotechnology Letters* **2016,** 8, (12), 1054-1060.

22. Panigaj, M.; Johnson, M. B.; Ke, W.; McMillan, J.; Goncharova, E. A.; Chandler, M.; Afonin, K. A., Aptamers as Modular Components of Therapeutic Nucleic Acid Nanotechnology. *ACS Nano* **2019,** 13, (11), 12301-12321.

23. Yourston, L. E.; Lushnikov, A. Y.; Shevchenko, O. A.; Afonin, K. A.; Krasnoslobodtsev, A. V., First Step Towards Larger DNA-Based Assemblies of Fluorescent Silver Nanoclusters: Template Design and Detailed Characterization of Optical Properties. *Nanomaterials (Basel)* **2019,** 9, (4).

24. Guo, Y.; Shen, F.; Cheng, Y.; Yu, H.; Xie, Y.; Yao, W.; Pei, R.; Qian, H.; Li, H.-W., DNA-Hairpin-Templated Silver Nanoclusters: A Study on Stem Sequence. *The Journal of Physical Chemistry B* **2020**.

25. Ramsay, H.; Simon, D.; Steele, E.; Hebert, A.; Oleschuk, R. D.; Stamplecoskie, K. G., The power of fluorescence excitation–emission matrix (EEM) spectroscopy in the identification and characterization of complex mixtures of fluorescent silver clusters. *RSC Advances* **2018,** 8, (73), 42080-42086.

26. Yourston, L.; Rolband, L.; Lushnikov, A.; West, C.; Afonin, K.; Krasnoslobodtsev, A., Tuning properties of silver nanoclusters with RNA nanoring assemblies. *Nanoscale* **2020**.

27. Yourston, L. E.; Krasnoslobodtsev, A. V., Micro RNA Sensing with Green Emitting Silver Nanoclusters. *Molecules* **2020,** 25, (13).

28. Petty, J. T.; Sergev, O. O.; Kantor, A. G.; Rankine, I. J.; Ganguly, M.; David, F. D.; Wheeler, S. K.; Wheeler, J. F., Ten-Atom Silver Cluster Signaling and Tempering DNA Hybridization. *Analytical Chemistry* **2015,** 87, (10), 5302-5309.

29. Chaloupka, K.; Malam, Y.; Seifalian, A. M., Nanosilver as a new generation of nanoproduct in biomedical applications. *Trends in Biotechnology* **2010,** 28, (11), 580-588.

30. Deshmukh, S. P.; Patil, S. M.; Mullani, S. B.; Delekar, S. D., Silver nanoparticles as an effective disinfectant: A review. *Materials Science and Engineering: C* **2019,** 97, 954-965.

31. Cerretani, C.; Vosch, T., Switchable Dual-Emissive DNA-Stabilized Silver Nanoclusters. *ACS Omega* **2019,** 4, (4), 7895-7902.

32. Shah, P.; Rørvig-Lund, A.; Chaabane, S. B.; Thulstrup, P. W.; Kjaergaard, H. G.; Fron, E.; Hofkens, J.; Yang, S. W.; Vosch, T., Design Aspects of Bright Red Emissive Silver Nanoclusters/DNA Probes for MicroRNA Detection. *ACS Nano* **2012,** 6, (10), 8803-8814.

33. Enkin, N.; Wang, F.; Sharon, E.; Albada, H. B.; Willner, I., Multiplexed Analysis of Genes Using Nucleic Acid-Stabilized Silver-Nanocluster Quantum Dots. *ACS Nano* **2014,** 8, (11), 11666-11673.

34. Tian, X.; Jiang, X.; Welch, C.; Croley, T. R.; Wong, T.-Y.; Chen, C.; Fan, S.; Chong, Y.; Li, R.; Ge, C.; Chen, C.; Yin, J.-J., Bactericidal Effects of Silver Nanoparticles on Lactobacilli and the Underlying Mechanism. *ACS Applied Materials & Interfaces* **2018,** 10, (10), 8443-8450.

35. Verdolino, V.; Cammi, R.; Munk, B. H.; Schlegel, H. B., Calculation of pKa Values of Nucleobases and the Guanine Oxidation Products Guanidinohydantoin and Spiroiminodihydantoin using Density Functional Theory and a Polarizable Continuum Model. *The Journal of Physical Chemistry B* **2008,** 112, (51), 16860-16873.

36. Gambucci, M.; Cerretani, C.; Latterini, L.; Vosch, T., The effect of pH and ionic strength on the fluorescence properties of a red emissive DNA-stabilized silver nanocluster. *Methods and Applications in Fluorescence* **2019,** 8, (1), 014005.

37. Copp, S. M.; Schultz, D.; Swasey, S.; Pavlovich, J.; Debord, M.; Chiu, A.; Olsson, K.; Gwinn, E., Magic Numbers in DNA-Stabilized Fluorescent Silver Clusters Lead to Magic Colors. *The Journal of Physical Chemistry Letters* **2014,** 5, (6), 959-963.

38. Weerawardene, K. L. D. M.; Häkkinen, H.; Aikens, C. M., Connections Between Theory and Experiment for Gold and Silver Nanoclusters. *Annual Review of Physical Chemistry* **2018,** 69, (1), 205-229.

39. Le Ouay, B.; Stellacci, F., Antibacterial activity of silver nanoparticles: A surface science insight. *Nano Today* **2015,** 10, (3), 339-354.

40. Lakowicz, J. R., *Principles of fluorescence spectroscopy*. Third edition ed.; Springer, NY, USA: 2006

41. Yuan, X.; Setyawati, M. I.; Tan, A. S.; Ong, C. N.; Leong, D. T.; Xie, J., Highly luminescent silver nanoclusters with tunable emissions: cyclic reduction–decomposition synthesis and antimicrobial properties. *NPG Asia Materials* **2013,** 5, (2), e39-e39.

42. Jabed, M. A.; Dandu, N.; Tretiak, S.; Kilina, S., Passivating Nucleobases Bring Charge Transfer Character to Optically Active Transitions in Small Silver Nanoclusters. *J Phys Chem A* **2020,** 124, (43), 8931-8942.

43. Krause, S.; Cerretani, C.; Vosch, T., Disentangling optically activated delayed fluorescence and upconversion fluorescence in DNA stabilized silver nanoclusters. *Chemical Science* **2019,** 10, (20), 5326-5331.

44. Brewster, J. D., A simple micro-growth assay for enumerating bacteria. *Journal of Microbiological Methods* **2003,** 53, (1), 77-86.

APPENDIX A: SUPPORTING INFORMATION FOR DNA-TEMPLATED FLUORESCENT SILVER NANOCLUSTERS INHIBIT BACTERIAL GROWTH WHILE BEING NON-TOXIC TO MAMMALIAN CELLS

Lewis Rolband[1#], Liam Yourston[2#], Morgan Chandler[#1], Damian Beasock[#1], Leyla Danai[1], Seraphim Kozlov[1], Nolan Marshall[2], Oleg Shevchenko[1], Alexey V. Krasnoslobodtsev[2]*, and Kirill A. Afonin[1]*

[1]Nanoscale Science Program, Department of Chemistry, University of North Carolina at Charlotte, Charlotte, NC 28223, USA
[2]Department of Physics, University of Nebraska at Omaha, Omaha, NE 68182, USA

SEQUENCES USED IN THIS PROJECT

All oligonucleotides were purchased from IDT, Inc. Names denote the numbers of cytosines in each hairpin loop, underlined below.[1,2]

C7: 5'- TATCCGTCCCCCCCACGGATA
C9: 5'- TATCCGTCCCCCCCCCACGGATA
C11: 5'- TATCCGTCCCCCCCCCCCCACGGATA
C13: 5'- TATCCGTCCCCCCCCCCCCCCACGGATA

From Fig. S1:
C12: 5'- TATCCGTCCCCCCCCCCCCCACGGATA
Single-stranded C12: 5'- CCCCCCCCCCCCC

SUPPORTING METHODS

Bacterial growth of* Lactobacilli *on LB agar. One colony with the morphology of *Lactobacilli* was isolated from 1:100 and 1:1000 dilutions of Bulgarian yogurt (White Mountain) tested on LB agar plates in duplicate and was inoculated into SOS medium (Invitrogen) to prepare a pure culture. The culture was incubated at 42-45 °C for 36 hours to produce a turbid culture. A 100 µL aliquot of this culture was transferred into fresh SOS medium and again incubated at 42-45 °C for 36 hours to adapt *Lactobacilli* to SOS medium. This culture was then used for all subsequent experiments and was stored at 4 °C between experiments to prevent bacterial cells from proliferating. Each DNA-templated AgNC (C7, and C9) was mixed with liquid *Lactobacilli* culture in SOS media so that the final dilutions of bacteria were 1:1000 and 1:10,000 with nanoclusters at the final concentration of 22.5 µM of silver in 100 µL. From this, 25 µL of each sample was plated per one quarter of an LB agar plate; two replicates per sample were tested. Plates were incubated at 42-45 °C for 36 hours, then individual colonies were counted.

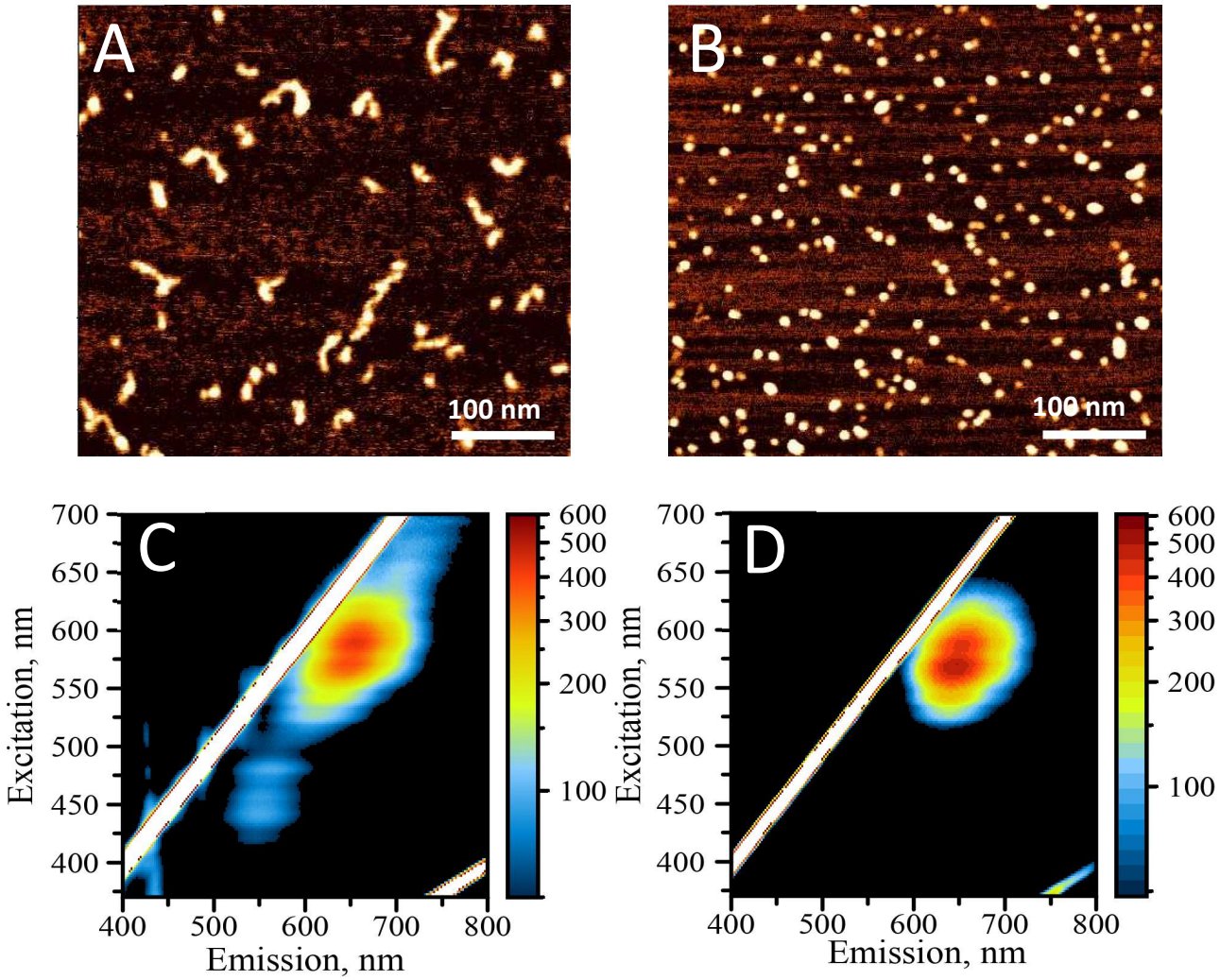

SI Figure S1. Comparison of C12 template as a single-stranded nucleotide or as a loop in a hairpin structure. **(A)** AFM image of AgNCs formed on a template containing single-stranded C12 sequence, **(B)** AFM image of AgNCs formed on a template containing C12 loop, **(C)** EEM of AgNCs templated on a template containing single-stranded C12 sequence, **(D)** EEM of AgNCs templated on a template containing C12 loop.

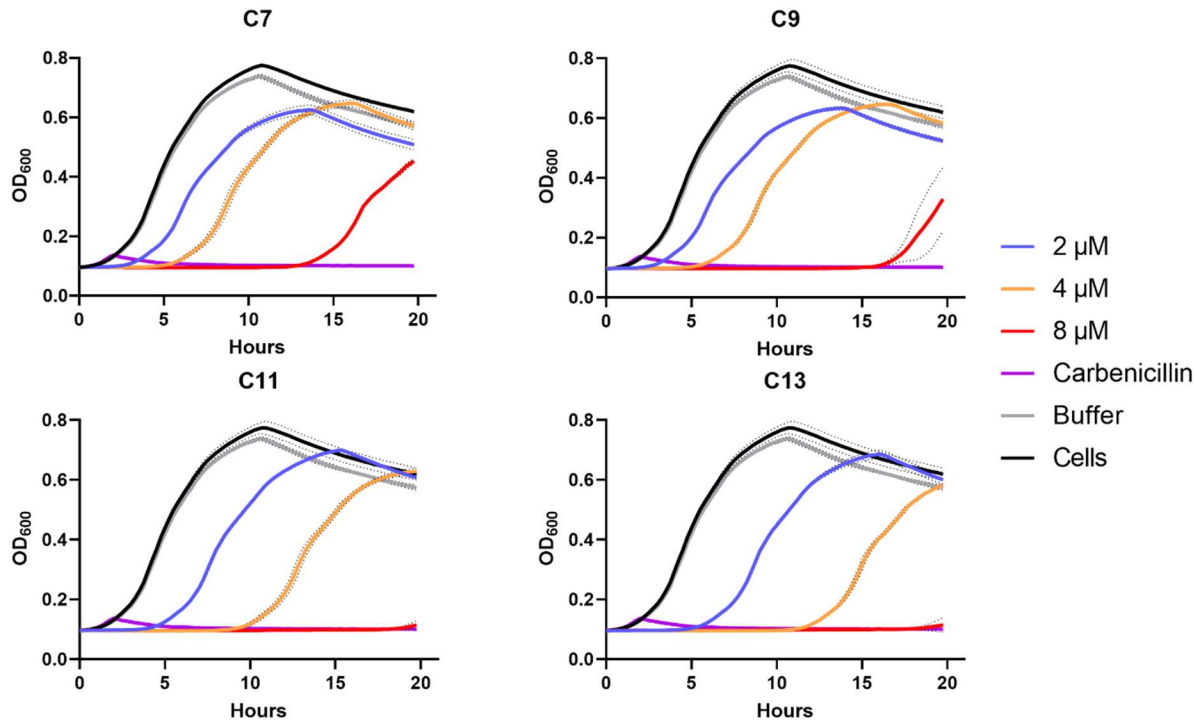

SI Figure S2. Liquid culture growth curves are shown of *E. coli* which have been treated with varying concentrations of AgNC. Each is shown with the standard deviation as a dotted line on either side of the solid line in the same color. There is a strong dose-dependence for each AgNC with 8 μM C11 eliminating growth for almost the full 20 hours.

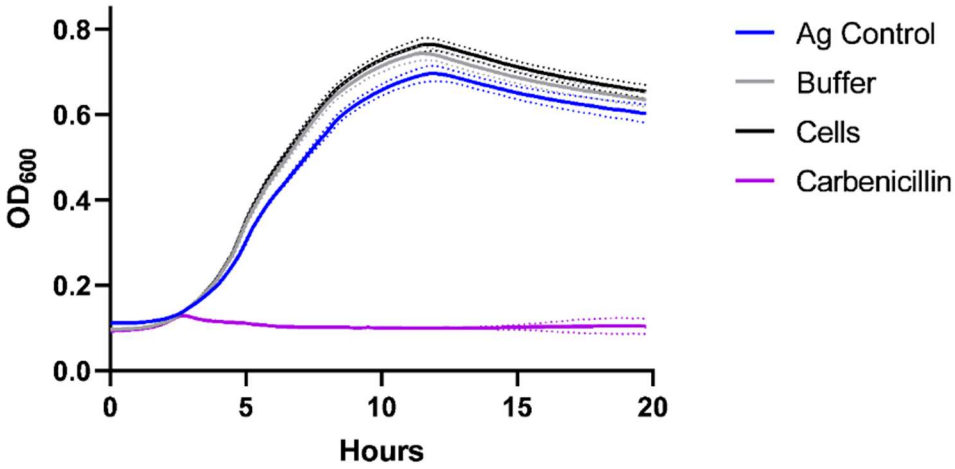

SI Figure S3. To see the effects of free silver that may not have bound to DNA, 650 μM $AgNO_3$ solution was reduced with an equimolar amount of $NaBH_4$, just as in the synthesis of the C13 AgNC. *E. coli* was then treated with the same amount of this solution as would be present in 4 μM C13 AgNC treatments. While there was a slight reduction in growth rate and the maximum OD_{600}, these were minimal compared to the effects of the C13 AgNC at 4 μM.

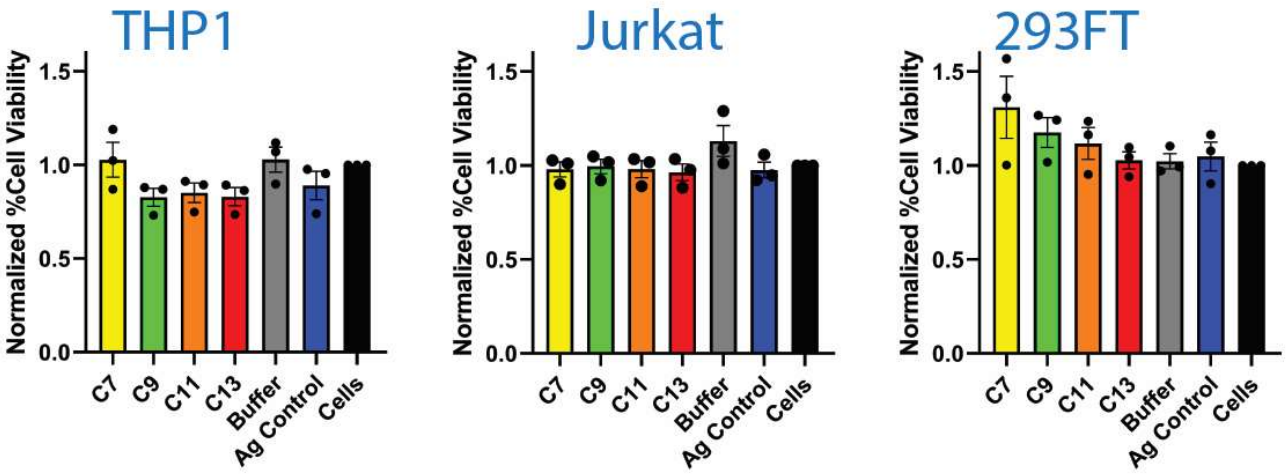

SI Figure S4. Additional mammalian cell viability assays were conducted with 8 μM AgNC concentrations following the methods described in the main text. Following 20 hours of incubation at 37 °C and 5% CO_2, MTS was added and incubated for an additional 75 minutes at the same conditions. The absorbance was recorded at 490 nm and the relative cell viability was calculated. No statistically significant reduction in cell viability was found at the elevated AgNC conditions.

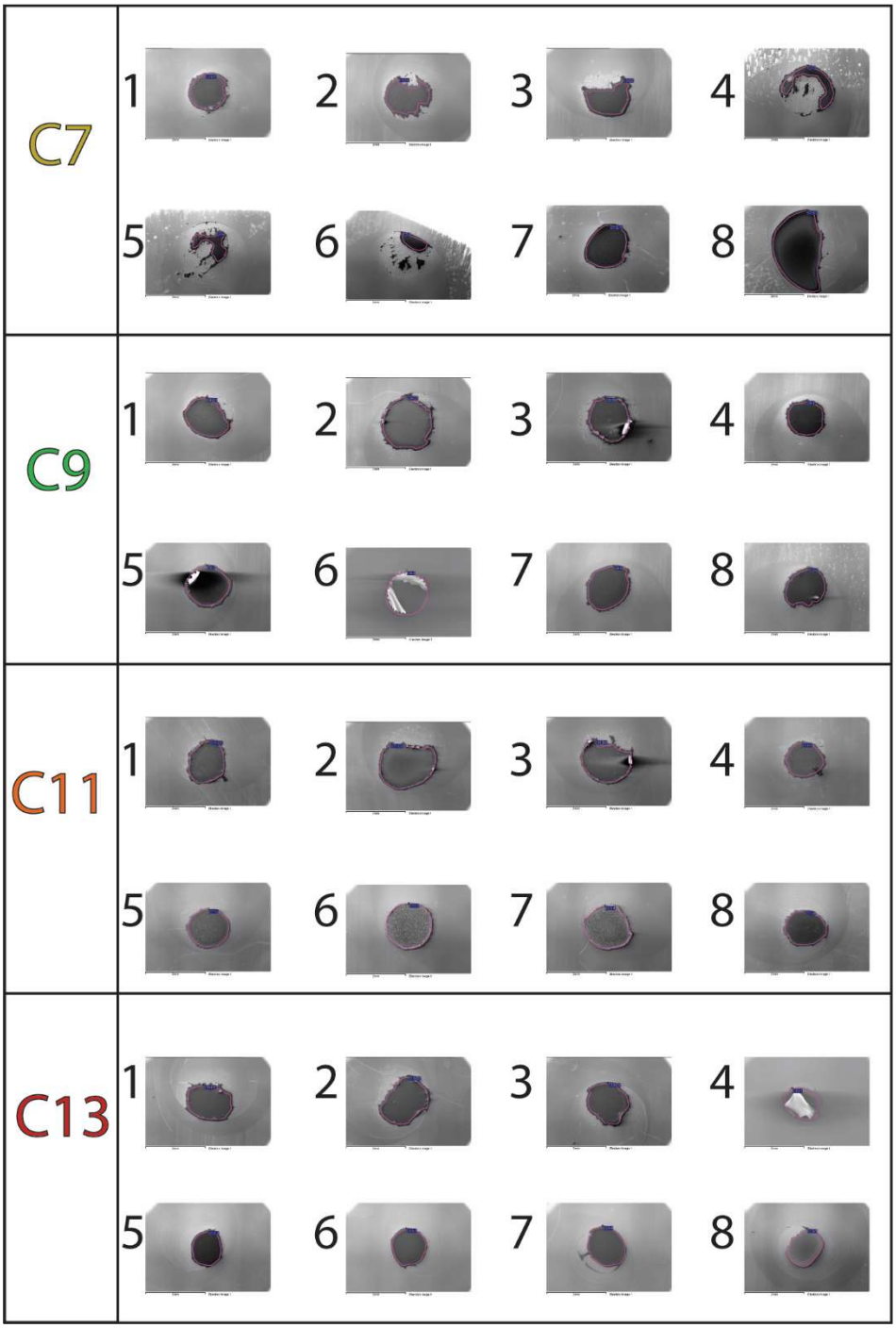

SI Figure S5. Secondary electron micrographs of all of the dried AgNC samples which were used for the stoichiometry calculations are shown.

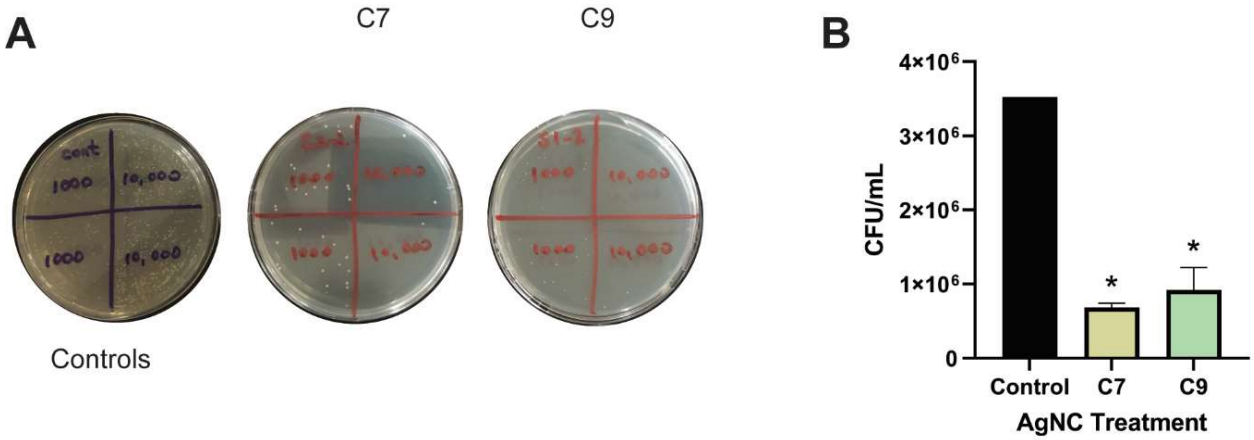

SI Figure S6. (A) Plates of *Lactobacilli* treated with C7 or C9 AgNCs and the resulting colonies formed. **(B)** Colony forming units (CFU)/mL after treatment with C7 or C9 were compared to the control sample Significance of $p<0.05$ is denoted with an asterisk.

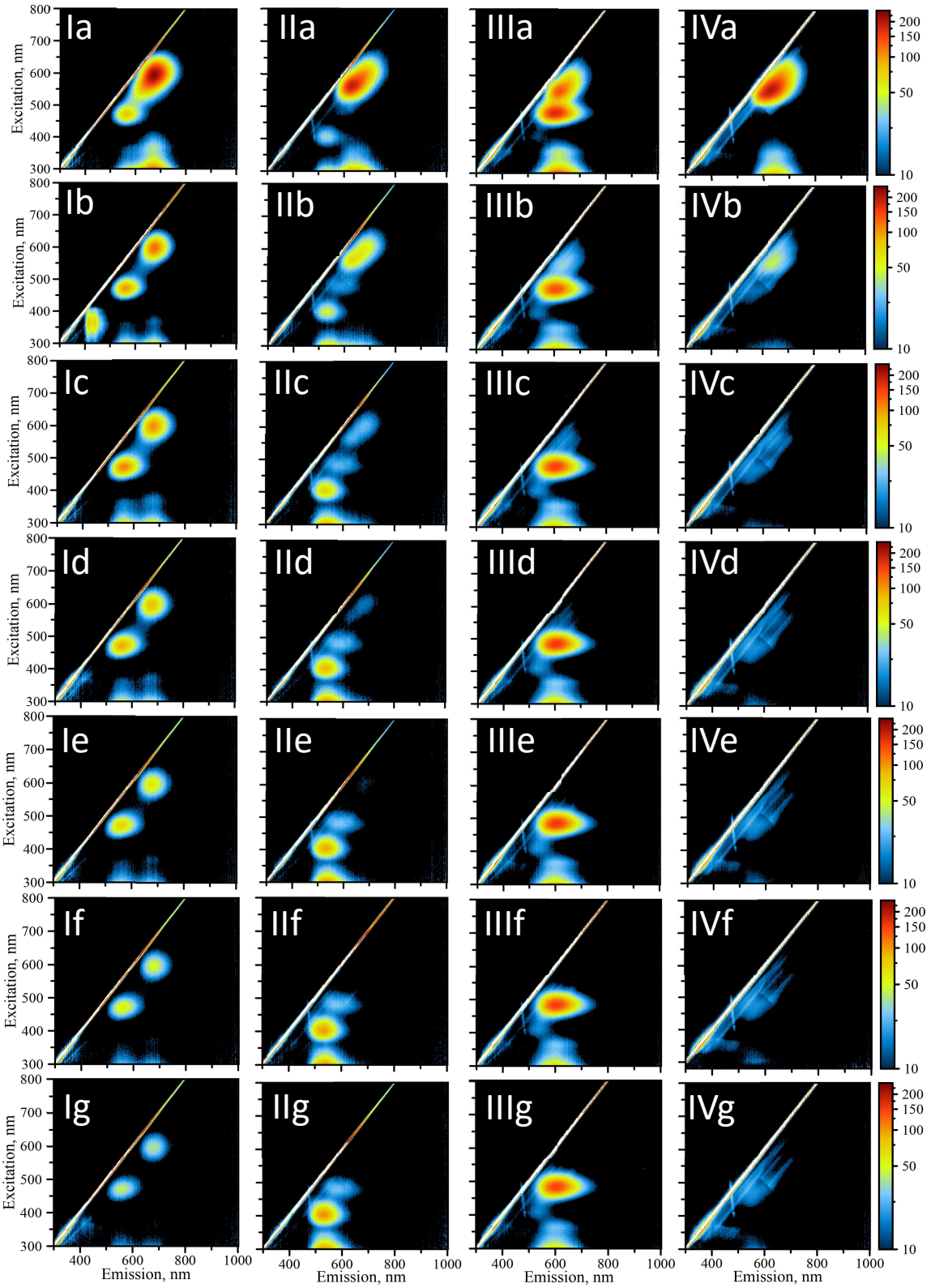

SI Figure S7. Titration of AgNCs with hydrogen peroxide. I) C7 DNA-AgNCs, II) C9 DNA-AgNCs, III) C11 DNA-AgNCs, IV) C13 DNA-AgNCs. Progressive addition of hydrogen peroxide shows changes in oxidative state of DNA-AgNCs. (**a-f**) are different ratios of C_{AgNC}/C_{H2O2} = 1/0 (**a**), 1/1.9 (**b**), 1/3.8 (**c**), 1/5.7 (**d**), 1/7.6 (**e**), 1/9.5 (**f**), 1/11.4 (g).

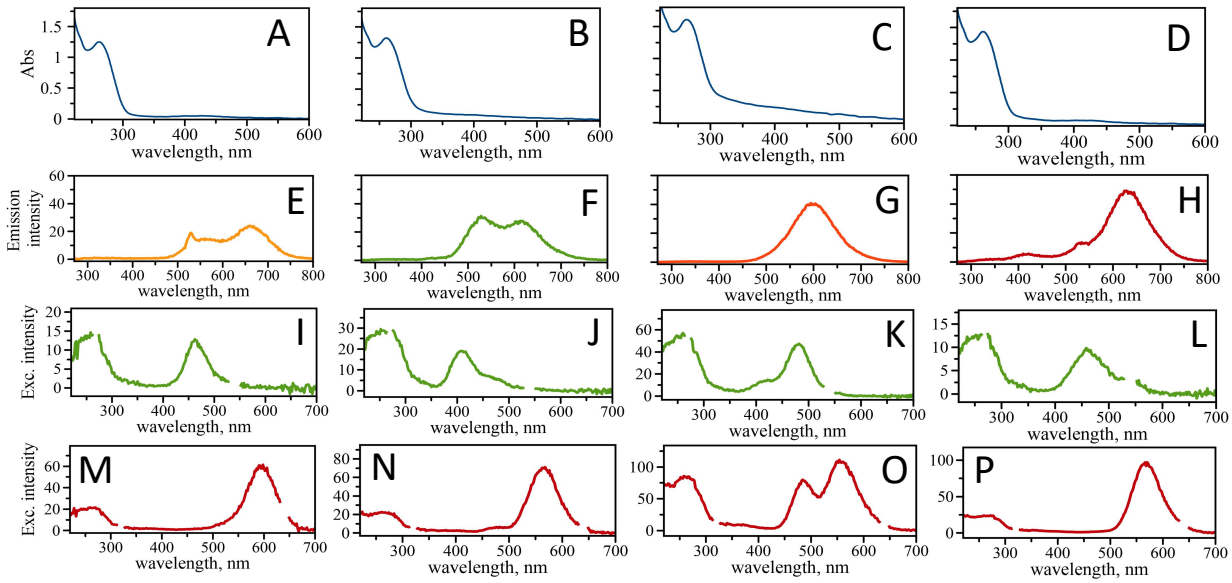

SI Figure S8. Evaluation of optical properties. UV-Vis spectra of A) C7, B) C9, C) C11, D) C13 samples immediately after purification. Emission spectra with 254 nm excitation mimicking color observation shown in Figure 1, E) C7, F) C9, G) C11, H) C13. Excitation spectra for 525 nm emission peak, I) C7, J) C9, K) C11, L) C13. Excitation spectra for 635 nm emission peak, M) C7, N) C9, O) C11, P) C13.

SI Table S1. The calculated number of silver atoms from the atomic percentages obtained from the EDS reports are shown with the average and standard error of the mean for each AgNC.

	1	2	3	4	5	6	7	8	Mean		SEM
C7	11.3	11.5	9.7	12.3	8.3	9.2	8.0	8.7	9.9	±	0.6
C9	10.2	7.9	11.4	7.4	7.8	7.6	8.0	7.7	8.5	±	0.5
C11	11.4	9.8	14.0	11.2	13.6	10.8	11.8	11.4	11.7	±	0.5
C13	11.3	13.3	10.9	8.0	7.5	7.9	8.7	13.7	10.2	±	0.9

Supporting References

(1) O'Neill, P. R.; Gwinn, E. G.; Fygenson, D. K. UV Excitation of DNA Stabilized Ag Cluster Fluorescence via the DNA Bases. *The Journal of Physical Chemistry C* **2011**, *115*, 24061-24066.

(2) O'Neill, P. R.; Velazquez, L. R.; Dunn, D. G.; Gwinn, E. G.; Fygenson, D. K. Hairpins with Poly-C Loops Stabilize Four Types of Fluorescent Agn:DNA. *The Journal of Physical Chemistry C* **2009**, *113*, 4229-4233.

CHAPTER 4. STRUCTURAL CHARACTERIZATION OF MULTISTRANDED NUCLEIC ACID NANOPARTICLES VIA SMALL-ANGLE X-RAY SCATTERING

1. Introduction:

The interest in developing novel ribonucleic acids (RNA) therapeutics has ramped up in recent years, with a third small interfering RNA (siRNA) formulation being approved by the FDA in 2020 and two mRNA vaccines leading the fight against SARS-COV-2[1-5]. RNA is naturally immunostimulatory, as foreign nucleic acids are commonly recognized by pattern recognition receptors as signs of viral or bacterial infection[6-8]. To minimize the immunostimulatory of RNA therapeutics, chemically modified nucleobases are frequently included, such as 1-methylpseudouridine in the case of the Pfizer/BioNTech vaccine[9, 10]. Another method of modulating the immunostimulatory of RNA is to use nucleic acid nanoparticles (NANPs) with specific geometries to deliver therapeutic moieties, such as siRNAs[11-14].

The growing field of RNA nanotechnology has yielded a library of rationally designed, self-assembling RNA nanoparticles with well-defined and predictable geometries[13, 15-21]. RNA folding via secondary and long-range tertiary interactions allows for RNA self-assembly and dictates its binding interactions with proteins and other molecules[22]. As the secondary and tertiary structures of RNA oligonucleotides are becoming easier to predict, due to the development of new computational methods, it is becoming easier to rationally design NANPs with programmed structures[23, 24]. NANPs are becoming increasingly studied for use in a variety of biomedical applications. Their ability to be reliably customized with controlled stoichiometries of functional moieties in geometrically precise ways make RNA nanoparticles attractive as modular therapeutic agents[11-13, 16, 25-27].

A variety of structural features of NANPs have been determined to dictate their immunogenicity, such as their dimensionality (1D vs 2D vs 3D) and the placement of therapeutic

moieties around the NANP[14, 28, 29]. As such, a robust procedure which may be adapted to characterize the vast library of nucleic acid nanoparticles must be developed. In keeping with our previous work, an RNA ring was chosen for further characterization due to its established use and thorough preliminary characterization[29-31]. The RNA ring under investigation is a hexameric assembly consisting of six 44 nt-long sequences. Each monomer undergoes intramolecular Watson-Crick base pairing to allow for the subsequent formation of intermolecular RNAI/RNAII inverse kissing loop complexes, as derived from the ColE1 plasmid in *E. coli*[15]. Each kissing loop pair is designed such that the loops can only form stable base pairing interactions with one other specific binding partner. As a result, the full ring assembly only forms in the presence of all six constituent strands[11]. This assembly strategy allows for each monomeric unit to be functionalized independently from the others. As such, up to six separate functionalities may be delivered on a single ring in predetermined stoichiometric ratios[32]. The addition of dicer substrate RNAs (DS-RNAs) allows these particles to serve as delivery agents for RNA interference-based therapeutics[11, 16, 32, 33]. The resulting 6 DS RNA rings are composed of 12 individual RNA oligonucleotides that self-assemble into a monodisperse population of particles[15, 16].

Small-angle x-ray scattering (SAXS) is a structural characterization technique that is well poised to further the understanding RNA nanotechnology's unique structure-function relationship. As SAXS measurements take place in a dynamic solution environment, information regarding exact atomic positions is lost. In return, the ability to observe biomolecular systems in their native environment is gained. As such, oligomerization states, overall conformation and flexibility is retained in SAXS measurements[28, 34-36]. This information is not always readily available in the case of high-resolution characterization methods, called as such due to their ability to map atomic coordinates, where the requirement to have fixed samples can lead to questions about these properties[28]. The ability of SAXS to confirm the oligomeric state of proteins and organic polymers has been extensively utilized, and the characterization of highly flexible biomolecular systems

have been shown to benefit greatly from the inclusion of SAXS experiments[37-39]. The present work shows the SAXS based characterization of an RNA ring comprised of six single-stranded oligonucleotides, including three-dimensional models of the structure obtained through a combination of *ab initio* and rigid body modeling. Symmetry assumptions are based on the designed structure and justified through the use of atomic force microscopy and previous characterization of this system[11, 15, 25, 30, 31]. Addition of SAXS to the characterization pipeline of NANPs serves as an effective means of characterizing RNA nanoparticle populations and can be adapted to any multi-stranded nucleic acid nanoassembly.

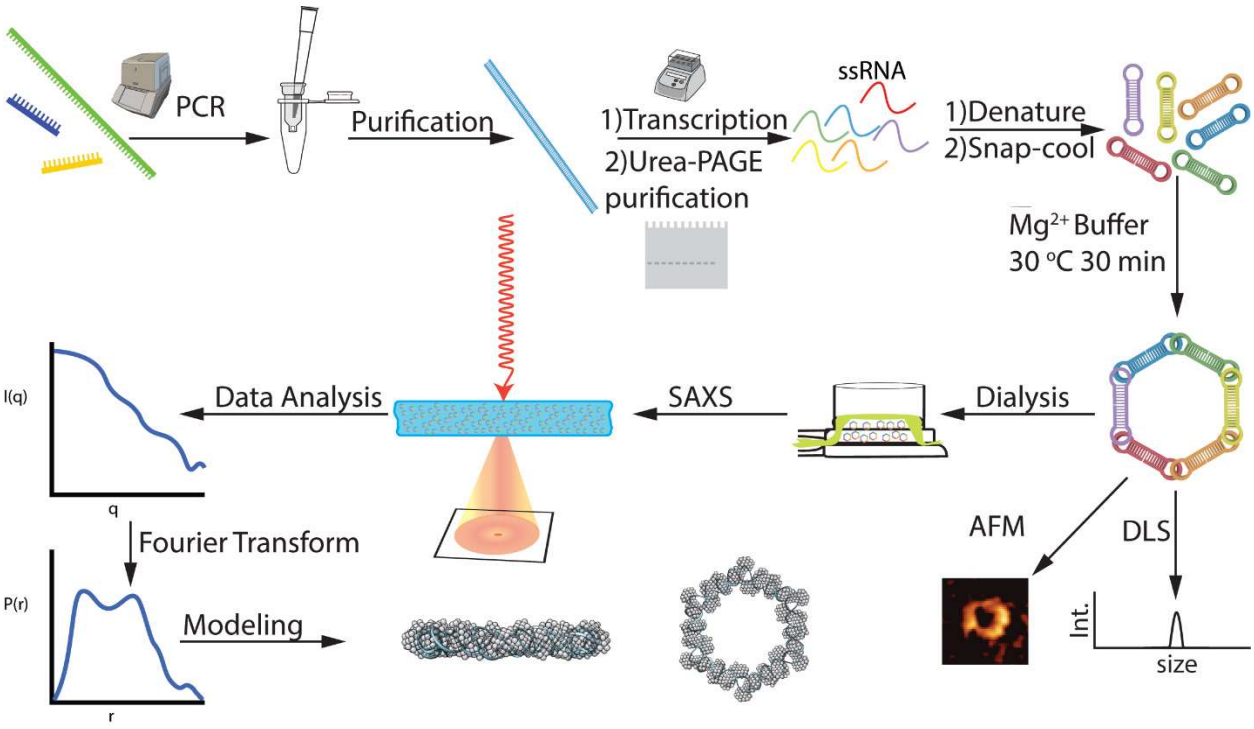

Figure 1. The experimental workflow is shown from the synthesis and initial characterization of the NANPs to the SAXS experiment and three-dimensional modeling.

2. Materials and Methods:

2.1 RNA Nanoparticle Synthesis

Forward primers, reverse primers, and template DNA oligonucleotides, containing a T7 RNA polymerase promoter region, were purchased from Integrated DNA Technologies. Polymerase chain reaction was used to amplify the DNA oligonucleotides using MyTaq™ Mix (Bioline) and the products were purified using the DNA Clean and Concentrator™ kit using the manufacturer's protocol (Zymo Research). *In vitro* run-off transcription, using t7 RNA polymerase, was performed to produce the RNAs, in 80 mM HEPES-KOH buffer, pH 7.5, 50 mM DTT, 2.5 mM spermidine, 5 mM NTPs and 25 mM $MgCl_2$ (Sigma-Aldrich). DNAse (Promega) was added to stop the transcription. Denaturing polyacrylamide gel electrophoresis, in 8 M urea, was used to purify the RNAs, which were visualized with a short wavelength UV lamp, cut out, and eluted in a solution of 300 mM NaCl, 2 mM EDTA, and 89 mM Tris-borate at pH 8.2 (Sigma-Aldrich). Using 2.5 volumes of 200 proof ethanol (VWR), washed with 180 proof ethanol, and dried by vacuum centrifugation at 55 °C. The RNAs were resuspended using 17.8 MΩ cm ultra-pure water and combined in equimolar ratios. The mixtures were heated to 95 °C for 2 minutes, snap-cooled to 4 °C for 2 minutes. Following cooling, the mixture was incubated at 30 °C for 30 minutes in assembly buffer (89 mM tris-borate, pH 8.2, 2 mM $MgCl_2$, 50 mM KCl). Assembly was confirmed through an electrophoretic mobility shift assay using a non-denaturing 8% PAGE (37.5:1 acrylamide:bisacrylamide). The assembled samples were dialyzed against 0.2 μm filtered assembly buffer at 4 °C with 12 hours between buffer changes. The third dialysate was saved for measurements as the matched buffer. The same protocol was used for the preparation of monomer samples using the same buffer solution sans $MgCl_2$.

2.2 Atomic Force Microscopy

Sample solutions of the NANPs were placed onto a freshly cleaved mica surface, modified with aminopropyl silatrane, and allowed to dry for 2 minutes. Unbound RNA was removed by washing the surface twice with 50 μL of deionized water, followed by gently drying with a flow of argon gas. Atomic force microscopy (AFM) was performed with a MultiMode AFM Nanoscope IV

system (Bruker Instruments) using a TESPA-300 probe. Micrographs were recorded with a 320 Hz resonance frequency, 1.5 Hz scanning rate, and a spring constant of 40 N/m in tapping mode. Micrographs were processed with FemtoScan Online (Advanced Technologies Center, Moscow, Russia) as previously reported[14].

2.3 Dynamic Light Scattering

Samples of the NANP assemblies were 0.2 μm filtered and 40 μL of the solution was used for each measurement with plastic micro cuvettes (Malvern Panalytical). Light scattering data was collected using a Malvern Instruments Zeta Sizer Nano with a 633 nm red laser. A total of 5 runs with 15 measurements per run were averaged. The equilibration time was set to 5 minutes and the scattering signal was collected at a 173° angle and the refractive index was set to 1.45. Data is presented as the Z-average hydrodynamic radius (R_h) ± the standard deviation.

2.4 Small-angle X-ray Scattering

SAXS data was collected at the Life Science X-ray scattering beamline (16-ID) at the National Synchrotron Light Source II at Brookhaven National Laboratory in February of 2021. The wavelength of the beam was set to 0.819 Å. Matched buffer data were recorded using the final dialysate and subtracted from the sample measurements to yield the scattering profile of each particle. Initial analysis was performed using the PRIMUS software to yield the root-mean-square distance of each atom to the center of mass, radius of gyration (R_g), through a Guinier approximation using the low q data.[40] The pair-wise probability distance distribution, P(r), and R_g were calculated and d_{max} was estimated using the GNOM software (ATSAS 3.0.1). [41] Dummy atom models of the monomer units were generated using DAMMIF to generate 20 models, superimpose, average them, and the resultant model from DAMFILT is shown.[42] The scattering of the models was fit to the experimental scattering profile using CRYSOL.[43] The secondary

structure of the monomeric subunits was predicted using NuPack (www.nupack.org).[23] The predicted secondary structure was used with RNA Composer to predict the three-dimensional structure of each subunit.[24] To model the assembled NANPs, the DAMFILT models of each monomer were used for rigid body modeling using SASREF with six-fold rotational symmetry as the only structural constraint.[44]

3. Results and Discussion

3.1 Initial Characterization

Table 1. The dimensions of the RNA nonfunctionalized ring, 6 DS RNA ring, and their monomer units are shown as determined by DLS and SAXS.

		Ring Monomer	DS RNA Ring Monomer	Ring	6 DS RNA Ring
DLS	**Z-Average R_h (Å)**	—		53 ± 2	101 ± 3
	Polydispersity Index	—		0.22 ± 0.03	0.23 ± 0.02
SAXS	**Guinier R_g (Å)**	21.2 ± 0.2	40.0 ± 0.5	60.5 ± 0.9	82.2 ± 0.7
	P(r) R_g (Å)	21.5 ± 0.1	36.3 ± 0.1	57.5 ± 0.3	83.3 ± 0.3
	d_{max} (Å)	68	115	166	284

Initial calculations of the size of the RNA ring based solely on the designed structure put estimates of its radius around 70 Å and its maximum linear dimension (d_{max}) close to 150 Å[15]. The addition of the DS RNAs is expected to add roughly 130-140 Å to the d_{max}, assuming they form A-form helices that are perpendicular the sides of the ring. The hydrodynamic radius (R_h) of a particle that is given from DLS measurements represents the radius of a hard sphere that diffuses at a similar rate as the analyte. As such, the R_h, for particles that deviate significantly from spheres, is a poor indicator of the size of the particles themselves. In the case of the nonfunctionalized ring, the R_h was found to be 53 ± 2 Å while the 6 DS RNA rings were found to have a R_h of 101 ± 3 Å (Table 1 and Figure 2A). The size of the 6 DS RNA rings obtained from

DLS quite different from the size of the particles shown in the AFM micrographs, which show the NANPs to have a d_{max} just over 300 Å in length (Figure 2B). The DLS data do confirm that, in solution, the nonfunctionalized ring and 6 DS RNA ring assemble into monodisperse populations of nanoparticles, as evidenced by their low polydispersity indices. The AFM results further confirm the assembly of each NANP and provide a justification for the imposition of 6-fold rotational symmetry on the system for the three-dimensional modeling of SAXS data, as slight structural differences between individual rings are believed to be caused by the fixation of the nanoparticles onto the mica substrate or interactions with the probe[28].

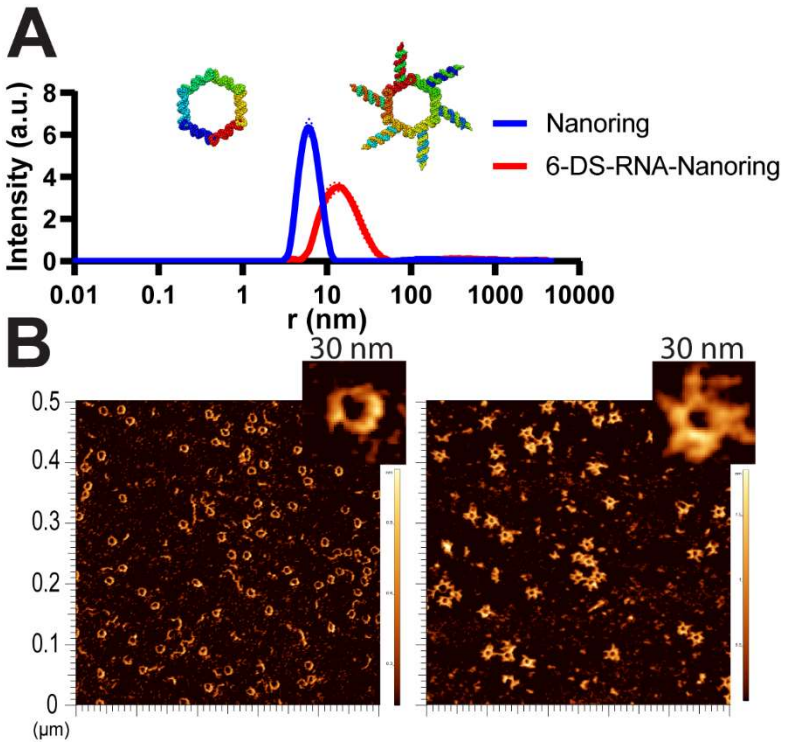

Figure 2. (A) Dynamic light scattering data collected with the nonfunctionalized ring (blue) and the 6 DS RNA ring (red) showing them to have hydrodynamic diameters of 53 Å and 101 Å respectively. **(B)** Atomic force micrographs are shown of the nonfunctionalized ring (left) and the 6 DS RNA ring (right).

3.2 Monomer Units

To resolve the entire structure of the nonfunctionalized ring and 6 DS RNA ring, we began with the characterization of each monomer unit which, while having different sequences of nucleobases, share a conserved global structure, in the form of a double hairpin with a nick in the middle of the anticipated dumbbell structure. As the presence of Mg^{2+} enhances the ability of the kissing loop complexes to form, SAXS measurements of the monomers were performed in a Mg-free buffer.

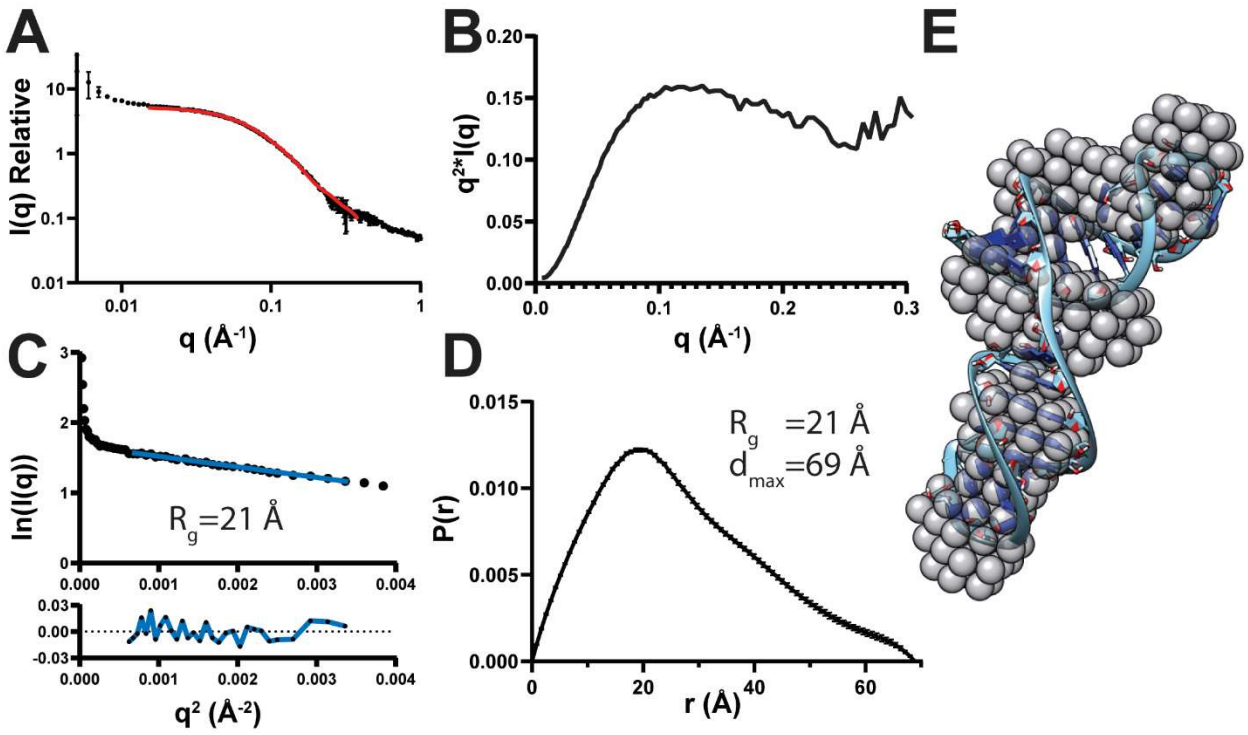

Figure 3. (A) The experimental SAXS profile of the RNA nonfunctionalized ring monomer is shown as black dots with the calculated scattering of the dummy atom model (E) shown as a solid red line (0.025 $Å^{-1}$ - 0.375 $Å^{-1}$). (B) The Kratky plot of the scattering profile is shown. (C) The Guinier fit of the data is shown with the linear fit appearing as a solid blue line. The residuals of the fit are plotted directly underneath the Guinier plot. (D) The pair-wise distance distribution of the SAXS data, calculated over 0.025 $Å^{-1}$ - 0.375 $Å^{-1}$ is shown. (E) The dummy atom model, which

is the average of 20 models, is shown with the atomic model generated by RNAcomposer superimposed using SUPCOMB.

3.2.1 *RNA ring monomer*

The ring monomer is designed to have 15 base pairs forming the length of the sides of the rings with a 7 nucleotide loop on either side of the dumbbell that base pairs with its corresponding partner in order to form the corners of the ring[15]. The d_{max} obtained from the pair-wise distance distribution is close to the predicted size of 65 Å[15]. The peak in the P(r) curve at 21 Å is close to what is expected for a B-form RNA helix (Figure 3D)[45]. The reduced χ^2 of the dummy atom model of the SAXS profile against the experimental data is 3.7, while the correlation map test yields a p-value of $1.3x10^{-5}$ [46]. The structure of the nonfunctionalized ring monomer, as predicted by RNA composer, adopts a bent conformation that implies that the two hairpins may have a wide array of available conformational states in solution (Figure 3E). This is expected, as the dumbbell-like structure that anticipated has a nick in the middle of the double-stranded region. The flexibility of the monomer is confirmed by the SAXS data, as shown by the level trend of the Kratky plot after the maximum $q^2*I(q)$ value (Figure 3C). The conformation of the monomer, predicted by RNA composer, fit well into the dummy atom model generated by DAMMIF, though there are some unoccupied spaces (Figure 3E).

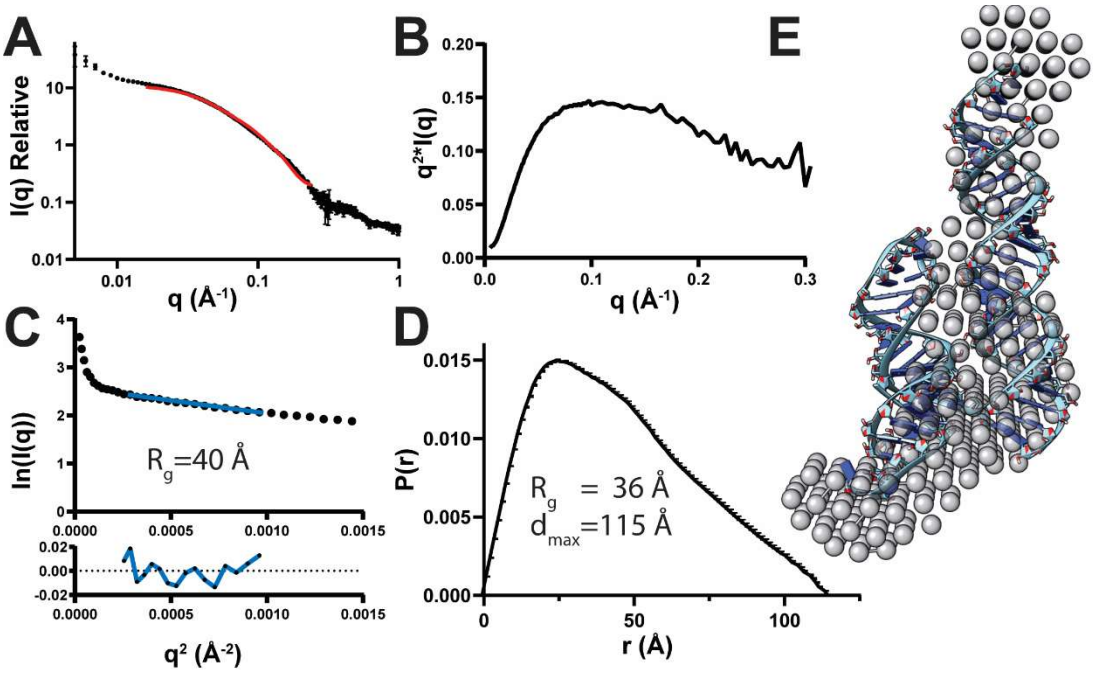

Figure 4. The experimental SAXS profile of the DS-RNA ring monomer is shown as black dots with the calculated scattering of the dummy atom model (E) shown as a solid red line (0.016 $Å^{-1}$ - 0.25 $Å^{-1}$). (B) The Kratky plot of the scattering profile is shown. (C) The Guinier fit of the data is shown with the linear fit appearing as a solid blue line. The residuals of the fit are plotted directly underneath the Guinier plot. (D) The pair-wise distance distribution of the SAXS data, calculated over 0.016 $Å^{-1}$ - 0.25 $Å^{-1}$ is shown. (E) The dummy atom model, which is the average of 20 models, is shown with the atomic model generated by RNAcomposer superimposed using SUPCOMB.

3.2.2 *DS RNA ring Monomer*

The DS RNA ring monomer consists of the same dumbbell forming sequence as the nonfunctionalized ring monomer, but it has been extended at the 3' end, by 29 nucleotides, with an siRNA sequence. A complementary 25 nucleotide long RNA oligonucleotide is bound to only the new extension with two unpaired bases on either side. As expected, it is much larger than the nonfunctionalized ring monomer, with a d_{max} 40 Å longer than the nonfunctionalized monomer. Its R_g has also nearly doubled as compared to the nonfunctionalized monomer unit. From the Kratky

plot (Figure 4C), the particle is shown to remain highly flexible, which is expected given the two unpaired nucleotides linking the DS RNA to the dumbbell. The simulated scattering profile of the dummy atom model has a χ^2 of 16.8 against the same region of experimental data and a p-value of 1.3×10^{-7} from the correlation map test. These are large deviations from what is considered to be a good fit, however, we still determine the modeled particle's simulated scattering to be a reasonable fit to the experimental data as the χ^2 is calculated in a way that considers the error of each measurement such that the higher the error of each measurement, the closer to the ideal value of 1 the final value of χ^2 will be given the same data. In the case of the data presented herein, the error of the region used for modeling is generally less than 2% of the detected intensity, in arbitrary units, while SAXS data with less than 12% noise are generally considered to be low-noise data[47]. While there are some discrepancies between the particle shapes determined through DAMMIF and the conformer output by RNAcomposer, they show the same general morphology (Figure 4E).

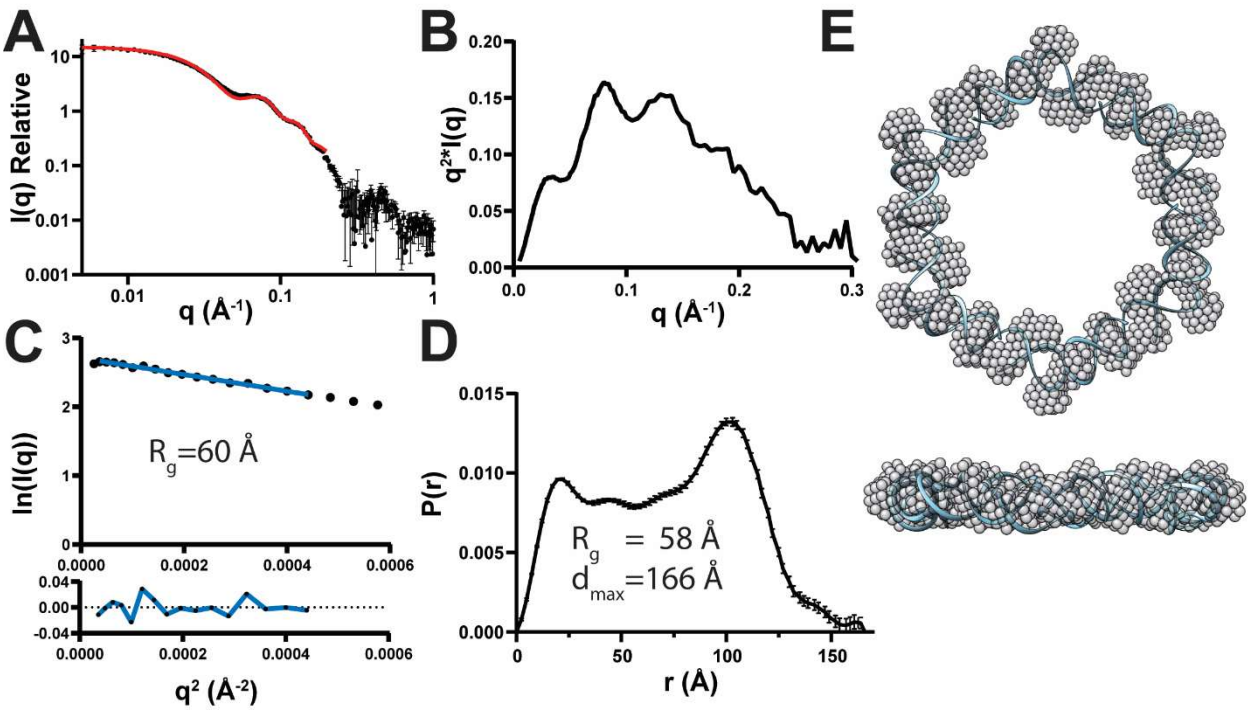

Figure 5. (A) The experimental SAXS profile of the RNA ring is shown as black dots with the calculated scattering of the dummy atom model (E) shown as a solid red line. (B) The Kratky plot of the scattering profile is shown. (C) The Guinier fit of the data is shown with the linear fit appearing as a solid blue line. The residuals of the fit are plotted directly underneath the Guinier plot. (D) The pair-wise distance distribution of the SAXS data, calculated over 0.005 $Å^{-1}$ - 0.2 $Å^{-1}$ is shown. (E) The dummy atom model was generated using rigid body modeling (SASREF) of the monomer to fit the experimental data with P6 symmetry is shown with the anticipated three-dimensional structure superimposed[44].

3.2.3 *RNA Ring*

The RNA ring showed an R_g which was slightly larger than the R_h, which was determined through DLS measurements, giving an R_g/R_h of 1.08-1.14 (Table 1). This ratio being greater than 1 is expected for particles that deviate significantly from spherical, which would have a R_g/R_h close to 0.78 [48]. While the constituent monomers of the ring have been shown to be flexible through their Kratky plots (Figure 3C), the fully assembled ring does not seem to have the same degree of flexibility despite each monomer having the nick in the middle of its double-stranded region(Figure 5C). The ring appears to be slightly larger than the predicted d_{max} of 150 Å[15]. This may be due to a combination of the ring having a breathing mode of movement in solution to adopt a slightly elongated conformation and the attraction of a large ion and hydration layer around the highly charged RNA backbone[49, 50]. The modeling of this particle through rigid body modeling, using SASREF, was done using the dummy atom model of the monomer unit and with P6 symmetry as a constraint, which is justified through the design of this particle, which ensures full assembly only when all 6 constituent strands are together, and through the AFM micrographs which show hexagonal RNA rings (Figure 1B and Figure 5E)[44]. The rigid body modeling approach provided a model with a calculated scattering profile that reasonably fit the experimental data, with a χ^2 of 13.2 and a p-value of $1.0x10^{-6}$ from the correlation map test. The apparently poor fit

from the correlation mapping is largely due to the slightly larger dip in the calculated scattering of the model around 0.05 Å^{-1}. The error of each point in the region used for modeling (q= 0.005 Å^{-1} - 0.2 Å^{-1}) is generally less than 2%, which contributes to the high χ^2.

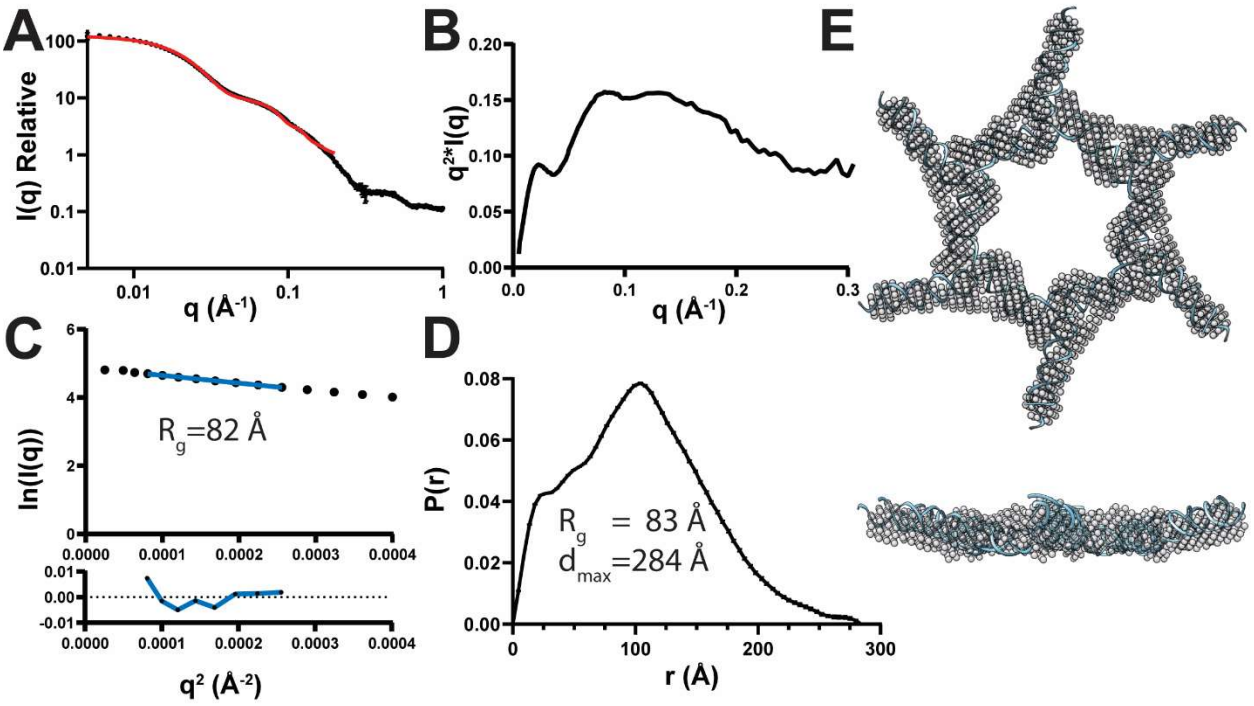

Figure 6. The experimental SAXS profile of the 6 DS RNA ring is shown as black dots with the calculated scattering of the dummy atom model (E) shown as a solid red line. (B) The Kratky plot of the scattering profile is shown. (C) The Guinier fit of the data is shown with the linear fit appearing as a solid blue line. The residuals of the fit are plotted directly underneath the Guinier plot. (D) The pair-wise distance distribution of the SAXS data, calculated over 0.005 Å^{-1} - 0.2 Å^{-1} is shown. (E) The dummy atom model was generated using rigid body modeling (SASREF) of the ring monomer to fit the experimental data with P6 symmetry is shown with the anticipated three-dimensional structure superimposed[44].

3.2.4 *6 DS RNA Ring*

The 6 DS RNA ring assembles in the same fashion as the nonfunctionalized ring, but with the 3' end of each monomer extended to accommodate a double stranded RNA sequence meant to trigger the RNA interference pathway[11, 15, 16]. As discussed above, there are two unpaired nucleotides linking the DS RNA arm to the section that forms the body of the ring. It is expected that this two-nucleotide linker is where the 6 DS RNA ring regains the flexibility over the nonfunctionalized ring, as can be seen from the Kratky plots of each (Figure 6C and Figure 5C respectively). The R_g/R_h ratio of this particle ranges from 0.81- 0.82, indicating that it behaves similarly to a globular particle in solution, though it is certainly not spherical. From the AFM micrographs, this particle generally appears to have a d_{max} of close to or even greater than 300 Å in some cases, but from the pair-wise distance distribution function, the d_{max} was estimated to be 284 Å (Figure 1B and Figure 6D). We expect that the interaction with the mica surface is biasing the conformation of the ring and DS RNA arms into an elongated and planar conformation, as conformational bias of nucleic acid nanostructures have been noted as an issue with AFM measurements in previous work[28]. Previous studies of this structure, using cryogenic electron microscopy, have shown a crown-like shape with the DS-RNA arms extended slightly out of the plane in a pinwheel like shape[11]. The three-dimensional modeling of this particle was done in a similar manner to that of the nonfunctionalized ring over a q range of 0.005 $Å^{-1}$ - 0.2 $Å^{-1}$ using SASREF to fit the experimental data using the DS-RNA monomer dummy atom model with a six-fold rotational symmetry constraint, justified through the same reasoning as is explained for the nonfunctionalized ring. The resultant model confirms the puckering of the DS-RNA arms out of the plane as was observed in previous studies. The calculated scattering of this model yields a χ^2 of 52.1 against the experimental data and the p-value obtained through the correlation map test is 1.0×10^{-6}. The data of the 6 DS RNA ring contained very little error, generally being less than 1% across the range used to generate the rigid body model.

As compared to previous attempts at modeling the RNA rings, the approach presented here, of first addressing the structure of the monomeric units and building the full structure from these pieces appears to have been more successful, through there is certainly more room for improvement. Prior results have given χ^2 values of nearly 60 for the nonfunctionalized ring and 400 for the 6 DS RNA ring. There models presented herein have χ^2 values of 13.2 and 52.1 for the same structures with similar quality data. While these values are still some distance from what would be considered an ideal fit, they represent a significant improvement in the production of 3D models of the NANPs from their 1D SAXS profiles.

Conclusion

The standard approach of characterizing novel nucleic acid nanomaterials, using a combination of dynamic light scattering and atomic force microscopy is effective as a means of confirming their assembly and general morphology; however, these techniques do not provide the whole picture of the structures of these systems. Including SAXS in the characterization of NANPs and other RNA molecules with conserved structures is a necessary step to gain proper insight into the true size and shape of these systems in the dynamic solution environment. For nucleic acid structures which rely on a combination of intra- and intermolecular interactions to fully assemble, like the hexameric RNA rings used in this work, the approach presented here-in is effective. Further improvements may be found in molecular dynamics simulations of the entire structure and surrounding solvation layers; however, these are computationally expensive and particularly time consuming for larger assemblies such as the 12-stranded 6 DS RNA ring. The means of assessing the three-dimensional structure of multi-stranded RNA assemblies shown here will be applicable for many systems, in particular those built from discreet monomeric units. We have shown that SAXS is able to provide significant structural information, including information regarding flexibility and three-dimensional models, and should be an integral step in the assessment of the structure of nucleic acid nanomaterials, in addition to DLS and AFM.

Acknowledgements

The authors would also like to thank Alexander Lushnikov and Yuri Lyubchenko for performing AFM imaging at the Nanoimaging Core Facility at the University of Nebraska Medical Center. We also wish to thank James Byrnes, Lin Yang, and Shirish Chodankar for their assistance with SAXS data collection. This research used resources [or insert beamline if applicable] of the National Synchrotron Light Source II, a U.S. Department of Energy (DOE) Office of Science User Facility operated for the DOE Office of Science by Brookhaven National Laboratory under Contract No. DE-SC0012704. The Center for BioMolecular Structure (CBMS) is primarily supported by the National Institutes of Health, National Institute of General Medical Sciences (NIGMS) through a Center Core P30 Grant (P30GM133893), and by the DOE Office of Biological and Environmental Research (KP1607011). Also, research reported in this publication was supported in part by the National Institute of General Medical Sciences of the National Institutes of Health under award number R35GM139587 (to K.A.A.). The content is solely the responsibility of the authors and does not necessarily represent the official views of the National Institutes of Health.

References

1. Scott, L. J.; Keam, S. J., Lumasiran: First Approval. *Drugs* **2021,** *81* (2), 277-282.
2. Dagan, N.; Barda, N.; Kepten, E.; Miron, O.; Perchik, S.; Katz, M. A.; Hernán, M. A.; Lipsitch, M.; Reis, B.; Balicer, R. D., BNT162b2 mRNA Covid-19 Vaccine in a Nationwide Mass Vaccination Setting. *New England Journal of Medicine* **2021,** *384* (15), 1412-1423.
3. Wang, Z.; Schmidt, F.; Weisblum, Y.; Muecksch, F.; Barnes, C. O.; Finkin, S.; Schaefer-Babajew, D.; Cipolla, M.; Gaebler, C.; Lieberman, J. A.; Oliveira, T. Y.; Yang, Z.; Abernathy, M. E.; Huey-Tubman, K. E.; Hurley, A.; Turroja, M.; West, K. A.; Gordon, K.; Millard, K. G.; Ramos, V.; Da Silva, J.; Xu, J.; Colbert, R. A.; Patel, R.; Dizon, J.; Unson-O'Brien, C.; Shimeliovich, I.; Gazumyan, A.; Caskey, M.; Bjorkman, P. J.; Casellas, R.; Hatziioannou, T.; Bieniasz, P. D.; Nussenzweig, M. C., mRNA vaccine-elicited antibodies to SARS-CoV-2 and circulating variants. *Nature* **2021,** *592* (7855), 616-622.
4. Noor, R., Developmental Status of the Potential Vaccines for the Mitigation of the COVID-19 Pandemic and a Focus on the Effectiveness of the Pfizer-BioNTech and Moderna mRNA Vaccines. *Current Clinical Microbiology Reports* **2021**.

5. Jackson, L. A.; Anderson, E. J.; Rouphael, N. G.; Roberts, P. C.; Makhene, M.; Coler, R. N.; McCullough, M. P.; Chappell, J. D.; Denison, M. R.; Stevens, L. J.; Pruijssers, A. J.; McDermott, A.; Flach, B.; Doria-Rose, N. A.; Corbett, K. S.; Morabito, K. M.; O'Dell, S.; Schmidt, S. D.; Swanson, P. A.; Padilla, M.; Mascola, J. R.; Neuzil, K. M.; Bennett, H.; Sun, W.; Peters, E.; Makowski, M.; Albert, J.; Cross, K.; Buchanan, W.; Pikaart-Tautges, R.; Ledgerwood, J. E.; Graham, B. S.; Beigel, J. H., An mRNA Vaccine against SARS-CoV-2 — Preliminary Report. *New England Journal of Medicine* **2020,** *383* (20), 1920-1931.
6. Okamoto, M.; Tsukamoto, H.; Kouwaki, T.; Seya, T.; Oshiumi, H., Recognition of Viral RNA by Pattern Recognition Receptors in the Induction of Innate Immunity and Excessive Inflammation During Respiratory Viral Infections. *Viral Immunology* **2017,** *30* (6), 408-420.
7. Schlee, M.; Hartmann, E.; Coch, C.; Wimmenauer, V.; Janke, M.; Barchet, W.; Hartmann, G., Approaching the RNA ligand for RIG-I? *Immunological Reviews* **2009,** *227* (1), 66-74.
8. Tatematsu, M.; Funami, K.; Seya, T.; Matsumoto, M., Extracellular RNA Sensing by Pattern Recognition Receptors. *Journal of Innate Immunity* **2018,** *10* (5-6), 398-406.
9. Chung, Y. H.; Beiss, V.; Fiering, S. N.; Steinmetz, N. F., COVID-19 Vaccine Frontrunners and Their Nanotechnology Design. *ACS Nano* **2020,** *14* (10), 12522-12537.
10. Mulligan, M. J.; Lyke, K. E.; Kitchin, N.; Absalon, J.; Gurtman, A.; Lockhart, S.; Neuzil, K.; Raabe, V.; Bailey, R.; Swanson, K. A.; Li, P.; Koury, K.; Kalina, W.; Cooper, D.; Fontes-Garfias, C.; Shi, P.-Y.; Türeci, Ö.; Tompkins, K. R.; Walsh, E. E.; Frenck, R.; Falsey, A. R.; Dormitzer, P. R.; Gruber, W. C.; Şahin, U.; Jansen, K. U., Phase I/II study of COVID-19 RNA vaccine BNT162b1 in adults. *Nature* **2020,** *586* (7830), 589-593.
11. Afonin, K. A.; Viard, M.; Koyfman, A. Y.; Martins, A. N.; Kasprzak, W. K.; Panigaj, M.; Desai, R.; Santhanam, A.; Grabow, W. W.; Jaeger, L.; Heldman, E.; Reiser, J.; Chiu, W.; Freed, E. O.; Shapiro, B. A., Multifunctional RNA Nanoparticles. *Nano Letters* **2014,** *14* (10), 5662-5671.
12. Chandler, M.; Panigaj, M.; Rolband, L. A.; Afonin, K. A., Challenges in optimizing RNA nanostructures for large-scale production and controlled therapeutic properties. *Nanomedicine* **2020,** *15* (13), 1331-1340.
13. Johnson, M. B.; Halman, J. R.; Satterwhite, E.; Zakharov, A. V.; Bui, M. N.; Benkato, K.; Goldsworthy, V.; Kim, T.; Hong, E.; Dobrovolskaia, M. A.; Khisamutdinov, E. F.; Marriott, I.; Afonin, K. A., Programmable Nucleic Acid Based Polygons with Controlled Neuroimmunomodulatory Properties for Predictive QSAR Modeling. *Small* **2017,** *13* (42), 1701255.
14. Hong, E.; Halman, J. R.; Shah, A. B.; Khisamutdinov, E. F.; Dobrovolskaia, M. A.; Afonin, K. A., Structure and Composition Define Immunorecognition of Nucleic Acid Nanoparticles. *Nano Lett.* **2018,** *18* (7), 4309-4321.
15. Grabow, W. W.; Zakrevsky, P.; Afonin, K. A.; Chworos, A.; Shapiro, B. A.; Jaeger, L., Self-Assembling RNA Nanorings Based on RNAI/II Inverse Kissing Complexes. *Nano Letters* **2011,** *11* (2), 878-887.
16. Afonin, K. A.; Grabow, W. W.; Walker, F. M.; Bindewald, E.; Dobrovolskaia, M. A.; Shapiro, B. A.; Jaeger, L., Design and self-assembly of siRNA-functionalized RNA nanoparticles for use in automated nanomedicine. *Nat. Protoc.* **2011,** *6* (12), 2022-2034.
17. Afonin, K. A.; Bindewald, E.; Yaghoubian, A. J.; Voss, N.; Jacovetty, E.; Shapiro, B. A.; Jaeger, L., In vitro assembly of cubic RNA-based scaffolds designed in silico. *Nature Nanotechnology* **2010,** *5* (9), 676-682.
18. Khisamutdinov, E. F.; Bui, M. N. H.; Jasinski, D.; Zhao, Z.; Cui, Z.; Guo, P., Simple Method for Constructing RNA Triangle, Square, Pentagon by Tuning Interior RNA 3WJ Angle from 60° to 90° or 108°. In *RNA Scaffolds: Methods and Protocols*, Ponchon, L., Ed. Springer New York: New York, NY, 2015; pp 181-193.

19. Guo, P., The emerging field of RNA nanotechnology. *Nature Nanotechnology* **2010,** *5* (12), 833-842.
20. Boerneke, M. A.; Dibrov, S. M.; Hermann, T., Crystal-Structure-Guided Design of Self-Assembling RNA Nanotriangles. *Angewandte Chemie International Edition* **2016,** *55* (12), 4097-4100.
21. Boerneke, M. A.; Hermann, T., Design and Crystallography of Self-Assembling RNA Nanostructures. In *RNA Nanostructures : Methods and Protocols*, Bindewald, E.; Shapiro, B. A., Eds. Springer New York: New York, NY, 2017; pp 135-149.
22. Leontis, N. B.; Westhof, E. J. R., Geometric nomenclature and classification of RNA base pairs. **2001,** *7* (4), 499-512.
23. Zadeh, J. N.; Steenberg, C. D.; Bois, J. S.; Wolfe, B. R.; Pierce, M. B.; Khan, A. R.; Dirks, R. M.; Pierce, N. A., NUPACK: Analysis and design of nucleic acid systems. *Journal of Computational Chemistry* **2011,** *32* (1), 170-173.
24. Antczak, M.; Popenda, M.; Zok, T.; Sarzynska, J.; Ratajczak, T.; Tomczyk, K.; Adamiak, R. W.; Szachniuk, M., New functionality of RNAComposer: application to shape the axis of miR160 precursor structure. *Acta Biochimica Polonica* **2017,** *63* (4), 737-744.
25. Yourston, L.; Rolband, L.; West, C.; Lushnikov, A.; Afonin, K. A.; Krasnoslobodtsev, A. V., Tuning properties of silver nanoclusters with RNA nanoring assemblies. *Nanoscale* **2020,** *12* (30), 16189-16200.
26. Xu, C.; Zhang, K.; Yin, H.; Li, Z.; Krasnoslobodtsev, A.; Zheng, Z.; Ji, Z.; Guo, S.; Li, S.; Chiu, W.; Guo, P., 3D RNA nanocage for encapsulation and shielding of hydrophobic biomolecules to improve the in vivo biodistribution. *Nano Research* **2020,** *13* (12), 3241-3247.
27. Piao, X.; Yin, H.; Guo, S.; Wang, H.; Guo, P., RNA Nanotechnology to Solubilize Hydrophobic Antitumor Drug for Targeted Delivery. *Advanced Science* **2019,** *6* (22), 1900951.
28. Oliver, R. C.; Rolband, L. A.; Hutchinson-Lundy, A. M.; Afonin, K. A.; Krueger, J. K., Small-Angle Scattering as a Structural Probe for Nucleic Acid Nanoparticles (NANPs) in a Dynamic Solution Environment. *Nanomaterials* **2019,** *9* (5), 681.
29. Chandler, M.; Rolband, L.; Johnson, M. B.; Shi, D.; Avila, Y. I.; Cedrone, E.; Beasock, D.; Danai, L.; Stassenko, E.; Krueger, J. K.; Jiang, J.; Lee, J. S.; Dobrovolskaia, M. A.; Afonin, K. A., Expanding Structural Space for Immunomodulatory Nucleic Acid Nanoparticles (Nanps) via Spatial Arrangement of Their Therapeutic Moieties. *Advanced Functional Materials* **2022**, 2205581.
30. Sajja, S.; Chandler, M.; Fedorov, D.; Kasprzak, W. K.; Lushnikov, A.; Viard, M.; Shah, A.; Dang, D.; Dahl, J.; Worku, B.; Dobrovolskaia, M. A.; Krasnoslobodtsev, A.; Shapiro, B. A.; Afonin, K. A., Dynamic Behavior of RNA Nanoparticles Analyzed by AFM on a Mica/Air Interface. *Langmuir* **2018,** *34* (49), 15099-15108.
31. Parlea, L.; Bindewald, E.; Sharan, R.; Bartlett, N.; Moriarty, D.; Oliver, J.; Afonin, K. A.; Shapiro, B. A., Ring Catalog: A resource for designing self-assembling RNA nanostructures. *Methods* **2016,** *103*, 128-137.
32. Saito, R. F.; Rangel, M. C.; Halman, J. R.; Chandler, M.; de Sousa Andrade, L. N.; Odete-Bustos, S.; Furuya, T. K.; Carrasco, A. G. M.; Chaves-Filho, A. B.; Yoshinaga, M. Y.; Miyamoto, S.; Afonin, K. A.; Chammas, R., Simultaneous silencing of lysophosphatidylcholine acyltransferases 1-4 by nucleic acid nanoparticles (NANPs) improves radiation response of melanoma cells. *Nanomedicine: Nanotechnology, Biology and Medicine* **2021,** *36*, 102418.
33. Afonin, K. A.; Kireeva, M.; Grabow, W. W.; Kashlev, M.; Jaeger, L.; Shapiro, B. A., Co-transcriptional Assembly of Chemically Modified RNA Nanoparticles Functionalized with siRNAs. *Nano Lett.* **2012,** *12* (10), 5192-5195.
34. Yang, S. C., Methods for SAXS-Based Structure Determination of Biomolecular Complexes. *Adv. Mater.* **2014,** *26* (46), 7902-7910.
35. Svergun, D. I.; Koch, M. H. J., Small-angle scattering studies of biological macromolecules in solution. *Rep. Prog. Phys.* **2003,** *66* (10), 1735-1782.

36. Grant, T. D.; Luft, J. R.; Carter, L. G.; Matsui, T.; Weiss, T. M.; Martel, A.; Snell, E. H., The accurate assessment of small-angle X-ray scattering data. *Acta Crystallogr. Sect. D-Biol. Crystallogr.* **2015,** *71*, 45-56.
37. Møller, M.; Nielsen, S. S.; Ramachandran, S.; Li, Y.; Tria, G.; Streicher, W.; Petoukhov, M. V.; Cerione, R. A.; Gillilan, R. E.; Vestergaard, B., Small Angle X-Ray Scattering Studies of Mitochondrial Glutaminase C Reveal Extended Flexible Regions, and Link Oligomeric State with Enzyme Activity. *PLoS One* **2013,** *8* (9), e74783.
38. van Genabeek, B.; de Waal, B. F. M.; Gosens, M. M. J.; Pitet, L. M.; Palmans, A. R. A.; Meijer, E. W., Synthesis and Self-Assembly of Discrete Dimethylsiloxane–Lactic Acid Diblock Co-oligomers: The Dononacontamer and Its Shorter Homologues. *J. Am. Chem. Soc.* **2016,** *138* (12), 4210-4218.
39. Lolli, G.; Naressi, D.; Sarno, S.; Battistutta, R., Characterization of the oligomeric states of the CK2 α2β2 holoenzyme in solution. *Biochemical Journal* **2017,** *474* (14), 2405-2416.
40. Konarev, P. V.; Volkov, V. V.; Sokolova, A. V.; Koch, M. H. J.; Svergun, D. I., PRIMUS: a Windows PC-based system for small-angle scattering data analysis. *Journal of Applied Crystallography* **2003,** *36* (5), 1277-1282.
41. Svergun, D. I., Determination of the regularization parameter in indirect-transform methods using perceptual criteria. *Journal of Applied Crystallography* **1992,** *25* (4), 495-503.
42. Franke, D.; Svergun, D. I., DAMMIF, a program for rapidab-initioshape determination in small-angle scattering. *Journal of Applied Crystallography* **2009,** *42* (2), 342-346.
43. Franke, D.; Petoukhov, M. V.; Konarev, P. V.; Panjkovich, A.; Tuukkanen, A.; Mertens, H. D. T.; Kikhney, A. G.; Hajizadeh, N. R.; Franklin, J. M.; Jeffries, C. M.; Svergun, D. I., ATSAS 2.8: a comprehensive data analysis suite for small-angle scattering from macromolecular solutions. *J. Appl. Crystallogr.* **2017,** *50* (4), 1212-1225.
44. Petoukhov, M. V.; Svergun, D. I., Global Rigid Body Modeling of Macromolecular Complexes against Small-Angle Scattering Data. *Biophys. J.* **2005,** *89* (2), 1237-1250.
45. Saenger, W., Polymorphism of DNA versus Structural Conservatism of RNA: Classification of A-, B-, and Z-TYPe Double Helices. In *Principles of Nucleic Acid Structure*, Saenger, W., Ed. Springer New York: New York, NY, 1984; pp 220-241.
46. Franke, D.; Jeffries, C. M.; Svergun, D. I., Correlation Map, a goodness-of-fit test for one-dimensional X-ray scattering spectra. *Nature Methods* **2015,** *12* (5), 419-422.
47. Rambo, R. P.; Tainer, J. A., Accurate assessment of mass, models and resolution by small-angle scattering. *Nature* **2013,** *496* (7446), 477-481.
48. Nygaard, M.; Kragelund, B. B.; Papaleo, E.; Lindorff-Larsen, K., An Efficient Method for Estimating the Hydrodynamic Radius of Disordered Protein Conformations. *Biophys. J.* **2017,** *113* (3), 550-557.
49. Chen, Y.; Pollack, L., SAXS studies of RNA: structures, dynamics, and interactions with partners. *Wiley Interdisciplinary Reviews: RNA* **2016,** *7* (4), 512-526.
50. Pollack, L., SAXS Studies of Ion–Nucleic Acid Interactions. *Annual Review of Biophysics* **2011,** *40* (1), 225-242.

APPENDIX B: SUPPORTING INFORMATION FOR STRUCTURAL CHARACTERIZATION OF MULTISTRANDED NUCLEIC ACID NANOPARTICLES VIA SMALL-ANGLE X-RAY SCATTERING

Sequences used in this project:

Component RNA strands of hexameric rings are denoted by 1-6. Functionalized strands which have been extended to accommodate the dicer-substrate are 1*-6*.

1

5′-GGGAACCGUCCACUGGUUCCCGCUACGAGAGCCUGCCUCGUAGC

2

5′-GGGAACCGCAGGCUGGUUCCCGCUACGAGAGAACGCCUCGUAGC

3

5′-GGGAACCGCGUUCUGGUUCCCGCUACGAGACGUCUCCUCGUAGC

4

5′-GGGAACCGAGACGUGGUUCCCGCUACGAGUCGUGGUCUCGUAGC

5

5′-GGGAACCACCACGAGGUUCCCGCUACGAGAACCAUCCUCGUAGC

6

5′-GGGAACCGAUGGUUGGUUCCCGCUACGAGAGUGGACCUCGUAGC

1*

5′-GGGAACCGUCCACUGGUUCCCGCUACGAGAGCCUGCCUCGUAGCUUCGGUGGUGCAGAUGAACUUCAGGGUCA

2*

5′-GGGAACCGCAGGCUGGUUCCCGCUACGAGAGAACGCCUCGUAGCUUCGGUGGUGCAGAUGAACUUCAGGGUCA

3*

5′-GGGAACCGCGUUCUGGUUCCCGCUACGAGACGUCUCCUCGUAGCUUCGGUGGUGCAGAUGAACUUCAGGGUCA

4*

5′-GGGAACCGAGACGUGGUUCCCGCUACGAGUCGUGGUCUCGUAGCUUCGGUGGUGCAGAUGAACUUCAGGGUCA

5*

5′-GGGAACCACCACGAGGUUCCCGCUACGAGAACCAUCCUCGUAGCUUCGGUGGUGCAGAUGAACUUCAGGGUCA

6*

5′-GGGAACCGAUGGUUGGUUCCCGCUACGAGAGUGGACCUCGUAGCUUCGGUGGUGCAGAUGAACUUCAGGGUCA

Dicer-substrate reverse complement

5′-/5Phos/ACCCUGAAGUUCAUCUGCACCACCG

CHAPTER 5: CONCLUSIONS

The utilization of therapeutic nucleic acids (TNAs) and nucleic acid nanoparticles (NANPs) continues to expand as more therapeutic formulations are constantly under development[1-5]. To ensure these therapies are safe and effective, it is important that a thorough understanding of their structures and the structures of their formulations are fully understood. Small-angle x-ray scattering (SAXS) is a technique which has the potential to greatly enhance the characterization pipeline of a variety of TNAs, including NANPs which may serve as a scaffold for the multiple therapeutic, diagnostic, and biosensing moieties[6, 7]. One potential TNA which may be carried by NANPs are fluorescent and antibacterial DNA-templated silver nanoclusters (DNA-AgNCs). These relatively new biopolymer-inorganic hybrid nanomaterials harbor great potential as tools in the fight against multidrug resistant bacterial infections[8, 9]. By combining these two technologies, NANPs and DNA-AgNCs, novel TNA formulations can be developed with the potential ability of fighting both local and systemic bacterial infections. In order to be certain that these materials are stable in solution and free of nonspecific aggregation or other interactions which are unsuitable for systemically administered drugs, the characterization of their solution state structure is an absolute must. The introduction of this work demonstrates the great success to which SAXS has already been applied to a number of TNAs and their formulations. Given the utility of this technique and the quantifiable information gained from it, it is likely that SAXS will continue to serve as a pivotal step in the TNA characterization pipeline.

The first main article of this work consists of a survey of the current applications of both DNA-AgNCs and silver nanoparticles (AgNPs). While both harbor significant capabilities as antibacterial agents, biosensors, and have unique optical properties, the small size, modularity, and readily observed fluorescence of DNA-AgNCs make them ideal for combination with NANP technologies. While little is known about the antibacterial mechanisms of DNA-AgNCs, great progress is being made in understanding the origin of their unique fluorescent signals. Many

computational studies, in addition to information gained from two crystal structures of DNA-AgNCs are helping push the understanding of how their charge states and the number of uncharged silver atoms affect the color of their fluorescence.

The second manuscript demonstrates that the size of the loop of poly-cytosine hairpin DNAs can modulate the color of the fluorescence, the antibacterial activity, and the rate and method of aging of the DNA-AgNC. From this work, it was found that a seven base pair stem with 13 cytosines in the loop of the hairpin was the most effective at inhibiting bacterial growth. This particular DNA-AgNC was also shown to age in a way that led to a decrease in the fluorescence intensity rather than a blue shift in the peak fluorescence wavelength. This finding was in contrast to what was observed for the three other DNA-AgNCs examined in this work. Furthermore, the DNA-AgNCs were all found to be non-toxic to mammalian cells after being treated with double the concentration that was found to effectively inhibit bacterial cell growth.

The final work which was presented shows how the SAXS based 3D reconstruction of a hexameric RNA NANP which is capable of carrying up to six separate functional moieties can be improved by taking a bottom-up approach to the modeling. This approach focused on initially characterizing the monomer units of the NANP, then using these data and models to build up to the full NANP structure using a combination of dummy-atom modeling and rigid-body modeling. This approach was able to significantly reduce the difference in the scattering of the 3D reconstruction and the experimental data. Moving forward, this approach can be used to aid in the 3D reconstruction of any number of NANPs.

As a whole, this work lays the groundwork for the spatial arrangement of DNA-AgNCs around a NANP scaffold which has been thoroughly characterized. The prior characterization of both of these systems will aid in the combination of the two technologies. This preliminary work also forms a basis for the physicochemical characterization of any number of newly developed DNA-AgNCs and NANPs. Given the clearly established structure–function relationship of these materials in

biological systems, this characterization will only continue to be critical in ensuring the safety, efficacy, and consistency of these novel classes of TNAs and their formulations.

References

1. Rolband, L.; Beasock, D.; Wang, Y.; Shu, Y. G.; Dinman, J. D.; Schlick, T.; Zhou, Y.; Kieft, J. S.; Chen, S. J.; Bussi, G.; Oukhaled, A.; Gao, X.; Šulc, P.; Binzel, D.; Bhullar, A. S.; Liang, C.; Guo, P.; Afonin, K. A., Biomotors, viral assembly, and RNA nanobiotechnology: Current achievements and future directions. *Comput Struct Biotechnol J* **2022,** *20*, 6120-6137.
2. Afonin, K. A.; Dobrovolskaia, M. A.; Ke, W.; Grodzinski, P.; Bathe, M., Critical review of nucleic acid nanotechnology to identify gaps and inform a strategy for accelerated clinical translation. *Advanced Drug Delivery Reviews* **2022,** *181*, 114081.
3. Afonin, K. A.; Dokholyan, N. V., Editorial to "Molecular engineering of biomaterials programmed to operate in living systems". *Adv Drug Deliv Rev* **2023,** *193*, 114669.
4. Chandler, M.; Johnson, B.; Khisamutdinov, E.; Dobrovolskaia, M. A.; Sztuba-Solinska, J.; Salem, A. K.; Breyne, K.; Chammas, R.; Walter, N. G.; Contreras, L. M.; Guo, P.; Afonin, K. A., The International Society of RNA Nanotechnology and Nanomedicine (ISRNN): The Present and Future of the Burgeoning Field. *ACS Nano* **2021,** *15* (11), 16957-16973.
5. Afonin, K. A.; Dobrovolskaia, M. A.; Church, G.; Bathe, M., Opportunities, Barriers, and a Strategy for Overcoming Translational Challenges to Therapeutic Nucleic Acid Nanotechnology. *ACS Nano* **2020,** *14* (8), 9221-9227.
6. Chandler, M.; Minevich, B.; Roark, B.; Viard, M.; Johnson, M. B.; Rizvi, M. H.; Deaton, T. A.; Kozlov, S.; Panigaj, M.; Tracy, J. B.; Yingling, Y. G.; Gang, O.; Afonin, K. A., Controlled Organization of Inorganic Materials Using Biological Molecules for Activating Therapeutic Functionalities. *ACS Applied Materials & Interfaces* **2021,** *13* (33), 39030-39041.
7. Fredrick, D.; Yourston, L.; Krasnoslobodtsev, A. V., Detection of cancer-associated miRNA using fluorescence switch of AgNC@NA and guanine-rich overhang sequences. *Luminescence* **2023**.
8. Rolband, L.; Yourston, L.; Chandler, M.; Beasock, D.; Danai, L.; Kozlov, S.; Marshall, N.; Shevchenko, O.; Krasnoslobodtsev, A. V.; Afonin, K. A., DNA-Templated Fluorescent Silver Nanoclusters Inhibit Bacterial Growth While Being Non-Toxic to Mammalian Cells. *Molecules* **2021,** *26* (13), 4045.
9. Yourston, L.; Rolband, L.; West, C.; Lushnikov, A.; Afonin, K. A.; Krasnoslobodtsev, A. V., Tuning properties of silver nanoclusters with RNA nanoring assemblies. *Nanoscale* **2020,** *12* (30), 16189-16200.